Electromagnetic Phenomena in $CeCu_6$, $^3He-^4He$ Solutions and $CsNiF_3$ at Low Temperatures

A Dissertation

Presented to the Faculty of the Graduate School

of Cornell University

in Partial Fulfillment of the Requirements for the Degree of

Doctor of Philosophy

by

Dean Lewis Hawthorne

January 2012

Electromagnetic Phenomena in $CeCu_6$,
$^3He-^4He$ Solutions and $CsNiF_3$
at Low Temperatures
Dean Lewis Hawthorne, Ph.D.
Cornell University 2012

This dissertation collates research on electromagnetic phenomena in three magnetic systems: the heavy fermion compound $CeCu_6$, dilute solutions of ^3He in superfluid ^4He and the quasi one-dimensional ferromagnet $CsNiF_3$.

Evidence for magnetic order in $CeCu_6$ at low temperatures is presented. The temperature dependence of the spin-lattice relaxation time T_1, measured using nuclear quadrupole resonance, and the AC magnetic susceptibility suggest some type of magnetic order in the low milli-Kelvin temperature regime.

We report the first application of acoustic saturation nuclear quadrupole resonance (ASNQR) at temperatures in the low/sub milli-Kelvin regime. Application of pulsed ultrasound at a given NQR frequency clearly results in significant saturation of the NQR line at the same frequency while the remaining NQR transitions remain unaffected.

Spin dynamics of ^3He-^4He solutions in the degenerate and non-degenerate regimes are discussed. Measurements of the longitudinal diffusion coefficient $D_\parallel$, observation of multiple spin echoes, and the observation of a new long time-scale excitation are reported. Computer simulations of the full non-linear spin dynamics reveal the importance of domain walls and similar magnetic objects in the time evolution of the long time-scale phenomena.

Results of a novel electron spin resonance transmission experiment on the quasi one-dimensional ferromagnet $CsNiF_3$ are reported. The results are shown to be consistent with the scattering of the uniformly precessing magnetization mode by massively higher energy solitons into degenerate magnons in an energy conserving but momentum non-conserving process.

BIOGRAPHICAL SKETCH

Dean Hawthorne was born in Ridgewood, New Jersey, son of John Hawthorne, factory worker and welder, and Janet Hawthorne, school bus driver. Together with his elder brother and sister, Dean grew up in the town of Hawthorne, New Jersey, where the Hawthorne family had resided since the nineteenth century when the area was still known as North Paterson. The official story regarding the naming of the town is that the town name was inspired by the hawthorn tree, not the Hawthorne family. However, the reader may note the difference in spelling between the name of the town and the name of the tree. Furthermore, in over twenty years of residence in the town of Hawthorne, Dean never saw a single hawthorn tree.

Dean's career in academia, engineering and the physical sciences developed in response to a series of fortuitous events. The first event occurred when Dean was a high school student. As luck would have it, Mary Gomes, a teacher in the Hawthorne High School history department, overheard Dean discussing middle eastern politics with a group of students in the cafeteria. Mrs. Gomes was impressed and demanded that Dean take her advance placement history class. Since advanced placement history was not a requirement for Dean's chosen career path, heavy metal guitarist, Dean refused. Mrs. Gomes replied "I know your parents. I used to baby sit you. I changed your diapers when you were an infant. You are taking my class. You have a brain and you *will* use it." Thus Dean abandoned the heavy metal guitarist fantasy, quit the band and turned to his studies. The rest, as they say, is history.

Upon graduation from high school, Dean entered New Jersey Institute of Technology's electrical engineering program, where the second fortuitous event occurred. While working in the NJIT Air Pollution Research Laboratory, Dean was overheard talking about his Native American heritage. Another employee of the lab had a connection to AT&T Bell Laboratories and suggested that Dean might apply for an AT&T summer employment program for minority students. Dean applied, was accepted and assigned to assist Dr. Laurent P. Lévy in his laboratory. In reality, Dr. Lévy assisted Dean far more than Dean assisted Dr. Lévy, but Dr. Lévy did not seem to mind. It was in Dr. Lévy's lab that Dean was bitten by the physics bug.

After graduating Summa cum Laude from NJIT in 1988, Dean headed to Cornell to pursue a Ph.D. in physics, funded by an AT&T fellowship. After a relatively enjoyable first year of graduate school, health issues arose and ultimately Dean opted to take a health leave of absence from graduate school, which put some strain on the relationship between Dean and his thesis advisor, Dr. David Lee.

A year of recuperation enabled Dean to launch a successful career as a software engineer. In 2004 he met Sarah Katherine Onley; they were married in 2008. With a wife and a successful career, Dean all but forgot about his years as a physicist in Clark Hall. Then one day while touching up his curriculum vitae, the third fortuitous event occurred. Dean reminisced about graduate school and realized that he had never actually thanked Dr. Lee for serving as his advisor, so he drafted an email to Dr. Lee for just that purpose. Dr. Lee responded with a plan for Dean to finish his Ph.D., a totally unexpected reaction. Within a few weeks and just one day shy of his 45th birthday, Dean was reinstated by the Graduate School, the oldest graduate student in the Field of Physics. Best of all, the tension between Dean and his advisor vanished, an old friendship renewed though one heartfelt thank you and a kind response.

Cornell's American Indian Program afforded Dean an avenue to become more active in Native American culture, an opportunity which was hard to come by growing up in suburban New Jersey. Dean served a term as president of the Cornell

Council of Native American Graduate and Professional Students. He attends sweat lodge whenever possible and has participated in the Sun Dance with the Mandan, Hidatsa and Arikara Nation of Fort Berthold in North Dakota as a fire keeper and a sun dancer.

To Dr. Laurent P. Lévy,

the person who inspired me to explore and enjoy

the beauty of the physical sciences.

ACKNOWLEDGEMENTS

Firstly, I must thank my parents for nurturing me throughout my academic career. Although they have both passed on, I know they would be very proud of the completion of my doctorate degree.

As I tried to make clear in the biographical sketch contained in this dissertation, there are several key people who helped me adjust the course of my life, ultimately guiding me to graduate school in the physical sciences. In actuality, the list is probably far too long to enumerate here, but two names stand out above the rest: Mrs. Mary Gomes, my high school history teacher who would not allow me to sink into apathy, and Dr. Laurent P. Lévy, who showed me first hand want it meant to be a scientist, as well as how to “slurp” data.

In addition to Dr. Lévy, I wish to thank the men and women of AT&T Bell Laboratories with whom I worked during my summers before leaving New Jersey for the colder climate of Cornell in Ithaca, New York. Again, the list of names is very extensive and spans two research divisions, Condensed Matter Physics and Lightwave Devices, but I would like to give special thanks to Dr. Douglas D. Osheroff who taught me an adage which would become a mantra for me: the only people who don’t break anything are the people who don’t do anything. Thanks to Dr. Osheroff’s advice, I have broken my fair share of things over the years.

I would like to thank my fellow graduate students in the Cornell Low Temperature Physics Group under professors Lee, Parpia, Reppy and Richardson. In addition to making doctoral research in condensed matter physics possible, your comradery also made it pleasant. Albert Putnam, George Stecher, Drew Geller, Linda Gunderson, Chao Jin, Peter Fraenkel, and Sheena Murphy, your expertise was invaluable and your company at Sa’s Place or the cheap Chinese restaurant in Collegetown was delightful. However, there is one name which stands out above the rest: Geoff Nunes. It was a great experience to work with Geoff on the ^{3}He-^{4}He solutions experiments; Geoff is truly an artist and a craftsman.

No experimental work below 77 Kelvin is successful without the assistance of Eric Smith, whose help on the $CeCu_6$ and ^{3}He-^{4}He solutions experiments is greatly appreciated. Working alongside "Captain Microkelvin," Lois Pollack exuded professionalism and energy during the $CeCu_6$ experiments; thank you.

Likewise, no experimental work is successful without the assistance of the wonderful Cornell facilities staff. The sands of time have shifted and individual names are no longer as clear in my mind as they were in the 1990's, so I will not attempt to attribute individuals here, but rather give kudos to the staff of the student and professional machine shops, the technical operations laboratory staff, the physical plant staff, the operators of the cryogenic fluids facility, and the Material Science Center computing and information technology staff.

I would like to thank and acknowledge the help of the members of my special committee: Dr. Veit Elser, Dr. Jeevak Parpia and of course, my advisor, Dr. David Lee. When I was a young graduate student, Nick Bigelow once said to me "By the time you finish your Ph.D., Dave Lee will not just be your advisor, he will be your friend." Now I can say that Nick was indeed correct.

Lastly, I would like to thank my wife Kate for putting up with my return to graduate school at age 45. Kate shouldered many of my burdens while I was busy reading papers, writing simulations on my computer, and writing this dissertation. Although she is the daughter of a physics professor and thus no stranger to physics shop talk, I cannot help but think that she sometimes listens to my dinner time ramblings about spin waves, computer simulations and the like purely out of politeness and love.

TABLE OF CONTENTS

LIST OF FIGURES

LIST OF TABLES

Part I

Nuclear quadrupole resonance in the heavy fermion compound $\mathbf{CeCu_6}$

Chapter 1

Low-temperature order in the heavy-fermion compound $\mathbf{CeCu_6}$[†]

1.1 Abstract

We have used nuclear-quadrupole-resonance (NQR) techniques to study Cu nuclei in two single-crystal samples of $CeCu_6$ between 200 μK and 20 mK. We present measurements of the NQR intensities and spin-lattice relaxation times, T_1, at frequencies corresponding to three different sites in the crystal. Below 5 mK we observe deviations from standard metallic behavior in both signal intensity and spin-lattice relaxation times. These deviations are unusual in that they are site dependent; they reveal the presence of one or more types of order in this system.

Heavy fermion (HF) compounds display a rich variety of magnetic order and exotic superconductivity.[1,2] However, the ground states of $CeCu_6$ and $CeAl_3$ (Ref. 3) have yet to be determined. These compounds have among the largest linear coefficients of specific heat, γ, in this class of systems.[1] The determination of their ground states would therefore be of special interest. In this paper we present our very low-temperature studies of $CeCu_6$. These measurements indicate the presence of one or more ordering transitions.

Earlier higher-temperature measurements by several groups[4,5,6] on pure $CeCu_6$

[†] Reprinted with permission from L. Pollack, M. J. Hoch, C. Jin, E. N. Smith, J. M. Parpia, D. L. Hawthorne, D. A. Geller, D. M. Lee, and R. C. Richardson, Phys. Rev. B, **52**, 707 (1995).

and on a series of alloys suggest that antiferromagnetic order is likely to occur in the pure compound in the limit of zero temperature. Aeppli *et al.*[4] obtained evidence of short-range antiferromagnetic correlations at $T = 0.4$ K from neutron-scattering measurements on pure $\mathrm{CeCu_6}$. For the alloy series $\mathrm{Ce(Cu_{1-x}Ag_x)_6}$ Gangopadhyay *et al.*[5] have made magnetic susceptibility measurements down to 60 mK and have observed evidence of antiferromagnetic ordering for $x < 0.10$. Recently, Löhneysen *et al.*[6] measured the magnetic susceptibility, specific heat, and transport of various samples of $\mathrm{CeCu_{6-x}Au_x}$. They conclude that for $x > 0.1$ long-range antiferromagnetic order occurs and that for $x = 0.1$ this is suppressed to a very low temperature by the competing Kondo effect. Other evidence to support a magnetic ground state is discussed by Kim and Stewart.[7] They point out that the large value of γ may be due to magnetic correlations in addition to an enhanced effective mass.

A static, magnetically ordered ground state is only one possibility. In other HF systems such as $\mathrm{CeCu_2Si_2}$ (Ref. 8) or $\mathrm{CeAl_3}$ (Ref. 9) dynamic magnetic correlation effects appear to be important. Finally HF superconductivity has been observed in several systems, sometimes in coexistence with magnetic order.[1,2]

We have carried out pulsed nuclear-quadrupole-resonance (NQR) measurements on Cu nuclei in two different samples of $\mathrm{CeCu_6}$. Our measurements as well as the measured ac susceptibility of the same samples[10,11] will be discussed. At zero field the nuclear quadrupole splitting is the result of the interaction of the electric quadrupole moment of the Cu nucleus with the electric field gradient present in the lattice. The crystal structure of $\mathrm{CeCu_6}$ is orthorhombic at room temperature with a transition to monoclinic below 200 K. As a result of the low symmetry of the lattice there are five independent copper sites with a nonzero E field gradient. In addition, the two copper isotopes ^{63}Cu and ^{65}Cu have nuclear quadrupole moments that differ by 6.9%. There are therefore ten different zero-field

NQR frequencies which range from 3.6 to 11.3 MHz.[12] The use of NQR provides a comparison of microscopic interactions at specific sites rather than the more general susceptibility measurements and neutron probes. NQR has previously been used to measure spin-lattice relaxation times (T_1) in CeCu$_6$ at temperatures above 60 mK. From changes in the temperature dependence of T_1 the transition from localized impurity (Kondo) state to the heavy electron state was found to occur at about 6 K. Between 60 and 200 mK a Korringa constant of 11 msec K has been measured[13] on a powdered sample.

We have studied three NQR transitions at frequencies of 3.9, 6.8, and 11.3 MHz. In all cases T_1 and signal intensity have been measured as a function of temperature. Both free induction decays and spin echoes were used. Since the samples are single crystals with mm scale dimensions, we are only exciting and detecting nuclei within a skin depth at any given frequency. At 11.3 MHz, assuming a resistivity of 5 $\mu\Omega$ cm, characteristic of a high-quality sample at mK temperatures,[11] we calculate a skin depth of approximately 30 μm. The skin depth increases with decreasing frequency as $\omega^{-1/2}$.

The H_1 field is supplied by a small coil wrapped around the sample, oriented along the orthorhombic "*a*" axis. The electron temperature of the copper plate on which the experiment is mounted is determined by a Pt NMR thermometer with higher resolution provided by a ^{3}He melting curve thermometer above 0.9 mK.[14] Our measurements span the temperature range 200 μK to 20 mK.

Two different samples were measured. A glow discharge mass spectrometer (GDMS) analysis[†] performed on the first sample (A) indicates the presence of magnetic and rare-earth impurities at the 10-100 ppm level. To eliminate possible artifacts introduced by impurity effects we obtained another sample (B) with

---

[†] Analyses were performed by Charles Evans and Associates, 301 Chesapeake Dr., Redwood City, CA 94063

negligible levels (less than 1 ppm from additional GDMS measurements) of these impurities. Both samples were thermally anchored with a thin layer of silver epoxy.

Spin-lattice relaxation times were measured by the standard techniques of saturating the spins and measuring the recovery after various delay times. At the lower temperatures, where the signal intensity is large, the recovery after saturation was monitored by a series of small angle tipping pulses. The value of T_1 at a given temperature appears to be independent of the method used to measure it in these experiments. The pulse length was between 10 and 100 times shorter than the inverse linewidth to ensure saturation. The relaxation curves do not appear to follow a single exponential in all cases; however, the relaxation of the majority of the magnetization occurs with a single time constant, T_1. Figure 1.1 shows T_1^{-1} for three different quadrupole resonances in sample B. Above 5 mK the relaxation follows the Korringa law, $T_1 T = 26$ msec K. Below 5 mK T_1^{-1} becomes site dependent: at the two lower-frequency sites (3.9 and 6.8 MHz) the best fit to the data indicates a T^3 dependence.

The data from sample A show a similar trend to that of sample B, but with a large change in scale factor. Above about 2 mK the data appear to follow a Korringa law but with a constant of 11000 msec K, a factor of 400 *larger* than that of the pure sample. Below 2 mK there is a sudden increase in T_1 for the 3.9 and 6.8 MHz transitions. Because of the length of time involved in reaching thermal equilibrium it was not feasible to take enough data to measure a power-law dependence at low temperatures. Again the 11.3 MHz transition exhibits different behavior below 3 mK. Following saturation, we cannot recover the full signal intensity after many hours, indicating an anomaly in the relaxation time.

The large difference in the Korringa constants for our two samples is clearly of significance, but is difficult to explain. Both exhibit a rapid increase in T_1 with

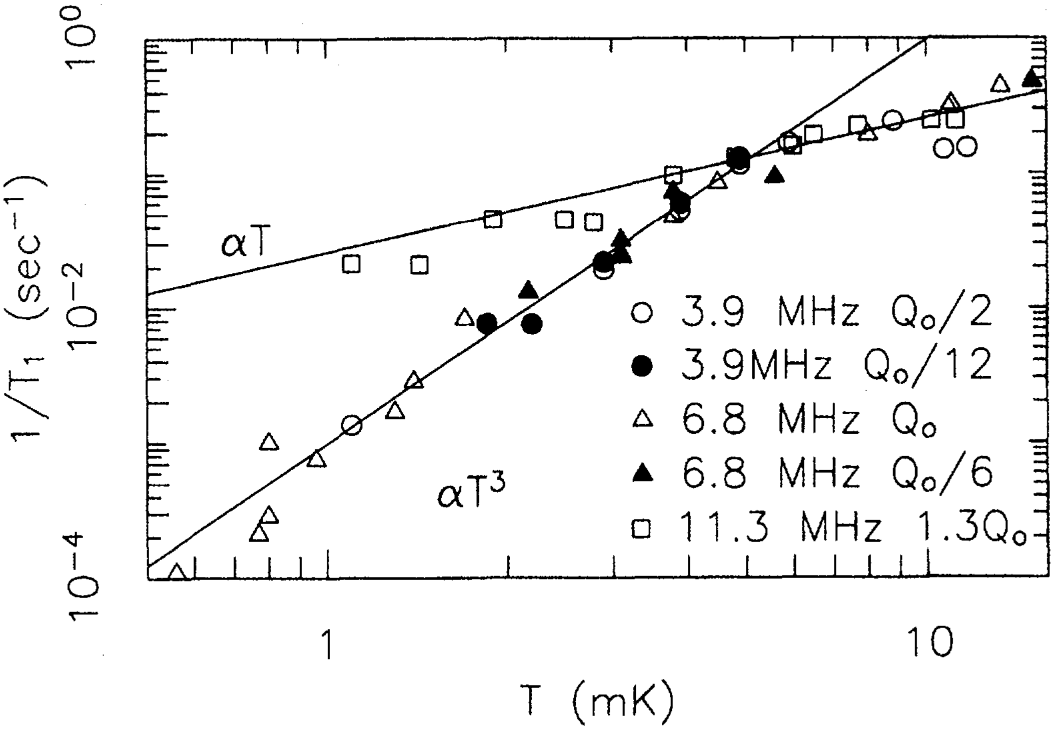

Figure 1.1: The spin-lattice relaxation data from sample B demonstrating the Korringa-like dependence ($T_1^{-1} \propto T$) at the 11.3 MHz NQR transition and the abrupt transition to $T_1^{-1} \propto T^3$ dependence for the other measured sites. Five different pulse energies (Q) were employed as a check on eddy current heating from the pulses.

decreasing temperature and show other features which point to a shared physical origin for the observed behavior. The difference between the Korringa constants of our high purity sample (B) and the sample of Ref. 12 is not understood. The relative difference is, however, much smaller than between our two samples. It is possible that the presence of trace amounts of various impurities affects the spin fluctuation spectrum leading to changes in the nuclear relaxation time.

We now turn to a discussion of measurements of the NQR signal intensity. For a paramagnetic system, the intensity obeys the Curie law. In this system we find that the intensity obeys the Curie-Weiss law, indicating antiferromagnetic correlations between nuclei (spins). This functional form fits the data very well over the entire temperature range; the sole exception occurs for the low temperature data at 11.3 MHz (near and below a peak observed at about 1 mK to be described in more detail below). The value of the Curie-Weiss temperature, Θ, varies with both site and sample; however, there is qualitative agreement between samples A and B in that Θ is largest for the 11.3 MHz resonance and comparable for the two lower-frequency lines. In sample B our best fit to the data yields values of the Curie-Weiss temperature Θ of -0.62 ± 0.1, -0.15 ± 0.1, and -0.1 ± 0.1 mK for the three resonances in order of decreasing frequency. For sample A the same type of fit yields Θ values of -2.5 ± 0.2, -0.42 ± 0.07, and -0.5 ± 0.2 mK, respectively. We plot the inverse signal intensity as a function of temperature for both samples in Fig. 1.2. We note the quantitative difference, but the qualitative similarity, between the samples, also reflected in the T_1 measurements.

The short T_1 for the spins at the 11.3 MHz site in sample B allows for detailed studies of its low-temperature signal intensity. As the cryostat warms up following a demagnetization, the signal intensity *increases* with increasing temperature, going through a peak at 1.1 mK (see Fig. 1.3). The height of this peak depends on

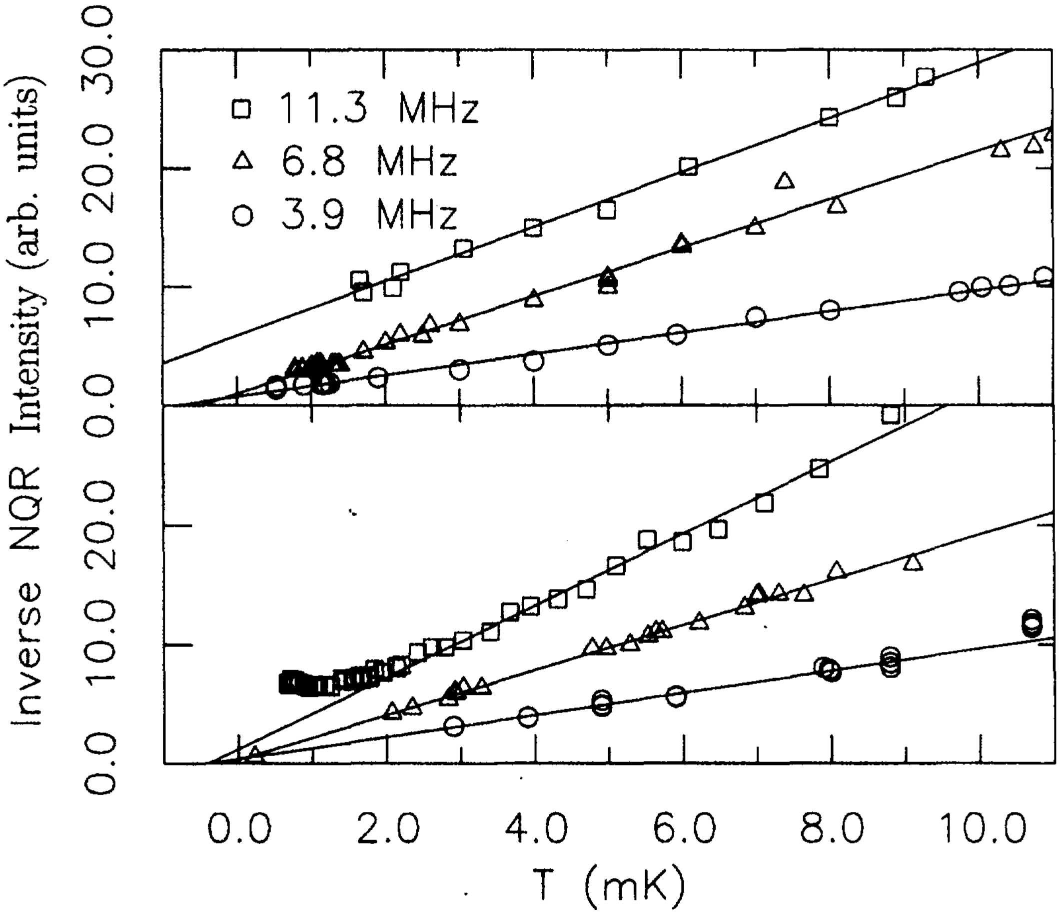

Figure 1.2: The inverse NQR intensity is plotted as a function of temperature for sample A (top) and sample B (bottom). A straight line with negative x intercept demonstrates the best fit to the Curie-Weiss law.

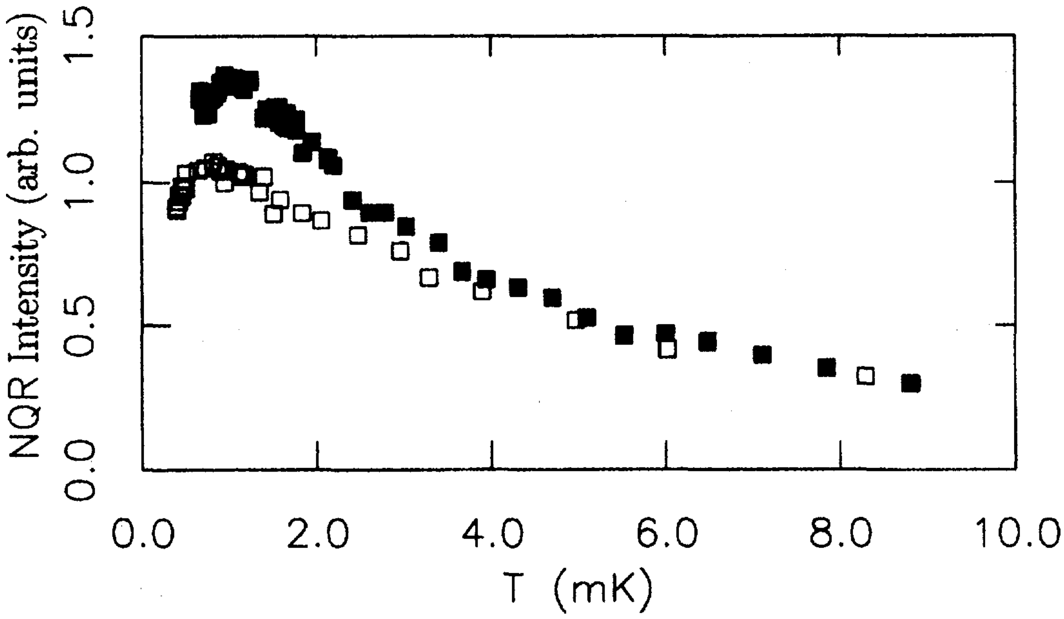

Figure 1.3: The NQR intensity from the 11.3 MHz transition as a function of temperature for two different warming rates of the nuclear stage. The run depicted with open circles has a faster warmup.

our cooling and warming rates, suggesting hysteresis. We studied the line shape, spin-echo decay time, and field dependence of the resonance. There was no substantial change in the line appearance and spin-echo decay time ($T_2 = 50\ \mu$sec) over the entire temperature range. The application of a field of 100 G resulted in a fourfold splitting of the line.[15] Again there was no substantial change in the temperature dependence of the signal with the field present.

The ac (electronic) susceptibility has also been measured for both samples. Sample A shows two peaks in χ',[10] at 3 and 0.5 mK. Similar features have been reported by Schuberth *et al.*,[16] after subtraction of a baseline due to magnetic Gd^{3+} ions. The susceptibility of sample B shows no maximum at 3 mK; we tentatively attribute the 3 mK feature in sample A to spin-glass ordering of an impurity system. At lower temperatures only a small increase in susceptibility is observed in sample B. There is no indication of the 0.5 mK peak; however, the thermometry was reliable only down to 0.9 mK.

The unique behavior described above for $CeCu_6$ must originate from an ordering transition of either the electronic or the nuclear spin system. Many features are similar to those observed in phase transitions in other systems; however, it appears that not all can be explained by any single phenomenon. In this section we will discuss ordering in other systems in relation to features observed in the NQR and electronic susceptibility of $CeCu_6$.

With regard to electronic order the most interesting possibility is superconductivity. Points to support this interpretation include the temperature dependence of T_1^{-1}, which strongly resembles that of a superconductor; there is an abrupt transition from a Korringa dependence to a T^3 dependence below 5 mK at two of the three sites. (A T^3 dependence has been observed in other exotic superconductors.[17]) Although the temperature dependence of T_1^{-1} at the 11.3 MHz site does not show this dramatic change, a site dependent T_1 has been observed in exotic superconductors, such as the high-T_c compound $YBa_2Cu_3O_7$.[18] Another feature of superconductivity is a sharp drop in the product of signal intensity and temperature reflecting the decreased penetration depth below T_c. This does not appear to explain the observed site dependence of the signal intensity, although the relative magnitudes of H_1 and H_{c1} are unknown and may lead to unanticipated effects. Finally, the ac susceptibility shows no evidence of flux exclusion at 5 mK.

Small moment (typically a fraction of μ_B) electronic antiferromagnetism exists in a number of HF system, often coexisting with superconductivity.[8] It is instructive to compare our measurements to NQR/NMR measurements on the HF $CeCu_2Si_2$,[8,19] which has a magnetic transition at $T = T_M$, just above the zero-field superconducting transition at $T = T_c$.[‡] In the presence of an applied field, the superconducting transition is suppressed, allowing for NMR measurements in the

---

[‡] There is a unique Cu site in $CeCu_2Si_2$.

magnetic state only. Several of the features of the magnetic transition of $CeCu_2Si_2$ resemble our measurements. There is a sharp decrease in the product of signal intensity and temperature at T_M with no corresponding change in line position or appearance. The temperature-independent line shape suggests the absence of the internal field which would be associated with static magnetic order. The lack of a static, internal field, coupled with the anomalous behavior of the spin-echo decay time (T_2) have been interpreted as signatures of a dynamic magnetic transition in $CeCu_2Si_2$.[8] We note that the T_2 measurements in $CeCu_2Si_2$ reveal a strong field dependence and that at zero field there is no temperature dependence down to well below T_c. Our T_2 measurements, also performed at zero field, are temperature independent. Measurements of $(T_1T)^{-1}$ at the magnetic transition in $CeCu_2Si_2$ show a small increase, followed by a rapid decrease below T_c. Although some of the features of the dynamic magnetic transition are similar to those observed in $CeCu_6$, the site dependence, especially in the T_1 measurements, cannot be readily explained on this basis.

The last class of electronic order that we consider involves a spin-glass transition of uncompensated moments in stray Ce^{3+} ions. Such a transition has been observed in samples of $CeCu_2Si_2$ which have been grown with variations in their stoichiometry.[8] The NMR signatures of this transition include an increase in the linewidth and a drop in nuclear signal that mimics a Curie-Weiss law. Finally, the temperature dependence of the intensity has a dramatic field dependence. Although our data can be well describe by a Curie-Weiss law, we see no change in linewidth. Additionally, our measurements of site dependence of the Curie-Weiss constants cannot be explained since the spin-glass transition would be global. The field dependence is also incorrect: since application of 2.5 T dramatically changes the nature of the spin-glass transition in $CeCu_2Si_2$, which has a zero field $T_g = 2.5$

K, we would expect some change with an applied field of 10^{-2} T if T_g were on the order of mK. Finally, there is no indication of a characteristic peak in the ac susceptibility in this temperature range.

With regard to nuclear order, the Curie-Weiss behavior of the nuclear spin system as well as the peak in signal intensity at 1.1 mK are reminiscent of NMR measurements on pure metallic systems that display nuclear order at low temperature.[20] Since these systems have lattices with cubic symmetry, every sites is equivalent. In the case of $CeCu_6$ the sites are not equivalent. The different Curie-Weiss constants that we measure could be the result of a spatially varying interaction. Of the two known mechanism that result in nuclear order in metals, the dipole-dipole interaction is far too small to result in ordering at 1 mK. However, a crude estimate of the relative magnitude of the Ruderman-Kittel-Kasuya-Yosida (RKKY) interaction in $CeCu_6$ and in metallic Cu shows an enhancement of roughly two orders of magnitude in the HF system.[21] Such a large exchange interaction would result in a significant increase in the ordering temperature, although it still falls short of the mK range. A more careful calculation of the RKKY interaction, taking into consideration all the details of the heavy electrons, would be necessary to make a useful comparison. The first example of of nuclear order resulting from the RKKY interaction under thermal equilibrium conditions has just been observed in the intermetallic compound $AuIn_2$ at 35 μK.[22]

In addition to these metals, there are other systems that display nuclear order but with a very high T_c (mK range), In solid ^{3}He atomic exchange results in a transition temperature below 1 mK.[23] Such a process is unlikely to exist in $CeCu_6$. The Van Vleck paramagnets also display nuclear order in the mK range. Due to the presence of $4f$ electrons there are large hyperfine fields in these compounds. $PrCu_6$, structurally similar to $CeCu_6$, is a hyperfine enhanced system in which the

Pr nuclear spins order ferromagnetically at 2.7 mK.[24] This type of order is unlikely in $CeCu_6$ as the Ce nuclei have no spin and there are no large hyperfine fields at the Cu nuclei.

A phase transition occurring in the low mK regime in either the nuclear or electronic system is highly unusual; however, unusual behavior, such as the coexistence of magnetism and superconductivity, is known to exist in HF compounds. The vast majority of experiments on these compounds have been focused on the electronic system. Thus it is not surprising that there are no theoretical models available to which we can compare our findings. It is evident that the interactions between nuclear and electronic systems as well as the ground-state properties of the nuclear spin system in these compounds are of considerable interest.

We acknowledge useful discussions with P. C. Hammel, C. L. Henley, D. L. Cox and G. R. Stewart. We thank L. Gunderson for assistance with the experiment, and A. Putnam for assistance with the x-ray orientation studies of the sample. This work was funded by the NSF through the Materials Science Center under Grant No. DMR-9121654 and by the NSF under Grant No. DMR-91099524.

REFERENCES FOR CHAPTER 1

[1] G. Stewart, Rev. Mod. Phys., **52**, 755 (1984).

[2] Z. Fisk *et al.*, Science, **239**, 33 (1988), and references within.

[3] O. Avenel *et al.*, Phys. Rev. B, **45**, 5695 (1988).

[4] G. Aeppli *et al.*, Phys. Rev. Lett., **57**, 122 (1986).

[5] A.K. Gangopadhyay *et al.*, Phys. Rev. B, **38**, 2603 (1988).

[6] H. v. Löhneysen *et al.*, Phys. Rev. Lett., **72**, 3262 (1994).

[7] J. Kim and G. Stewart, Phys. Rev. B, **49**, 327 (1994).

[8] H. Nakamura *et al.*, Condens. Matter, **4**, 437 (1992).

[9] S. Barth *et al.*, Phys. Rev. B, **39**, 695 (1989).

[10] C. Jin *et al.*, Physica B, **194**, 207 (1994).

[11] C. Jin, Ph.D. thesis, Cornell University (1993), (unpublished).

[12] K. Kumagai *et al.*, Jpn. J. Appl. Phys., **26**, 533 (1987).

[13] Y. Kitaoka *et al.*, J. Phys. Soc. Jpn., **54**, 3686 (1985).

[14] D. Greywall, Phys. Rev. B, **33**, 7520 (1986).

[15] A. Abragam, *Principles of Nuclear Magnetism* (Oxford University Press, Oxford, 1978).

[16] E.A.Schuberth *et al.*, Phys. Rev. B, **51**, 892 (1995).

[17] D. Cox and M. Maple, Phys. Today, **48**, 32 (1995).

[18] P.C. Hammel *et al.*, Phys. Rev. Lett., **63**, 1992 (1992).

[19] D. MacLaughlin, C. Tien, and L. Gupta, Phys. Rev. B, **30**, 1577 (1984).

[20] P. Hakonen, O. Lounasmaa, and A. Oja, J. Magn. Mater., **100**, 394 (1991).

[21] C. Schlicter, *Principles of Magnetic Resonance* (Springer-Verlag, Heidelberg, 1980).

[22] T. Herrmannsdörfer *et al.*, Phys. Rev. Lett., **74**, 1665 (1995).

[23] W.P. Halperin *et al.*, Phys. Rev. Lett., **32**, 927 (1974).

[24] J. Babcock *et al.*, Phys. Rev. Lett., **43**, 380 (1979).

Chapter 2

Acoustic coupling to NQR in the heavy fermion $CeCu_6$[†]

2.1 Abstract

We have designed an experiment to measure the bulk nuclear spin properties of a single crystal sample of $CeCu_6$ using a combination of pulsed ultrasound and NQR. Our preliminary studies show that there is a coupling between the sound waves and the nuclear quadrupole split energy levels. We will use this technique to explore the nature of the low temperature order previously observed in this system.[1‡]

2.2 Introduction

The use of resonant ultrasound to couple to the nuclear spin system in insulators was first demonstrated in the 1950's.[2] This work was extended to metals in the 1960's.[3] Although both ultrasound and nuclear resonance techniques have been widely used in the low/sub milliK regime, the techniques have not previously been combined in this temperature range. Acoustic excitation and detection has a large advantage over resonance techniques in the study of metal as the phonons

---

[†] Reprinted with permission from L. Pollack, R. K. Sundfors, E. N. Smith, D. L. Hawthorne, S. C. Kycia, and E. Bucher, in *Proceedings of the Twenty-First International Conference on Low Temperature Physics*, Vol. 46 (Czechoslovak Journal of Physics, 1996) p. 2081. Copyright ©1996 Springer Science and Business Media.

[‡] Research supported by the NSF through the Cornell Materials Science Center under DMR-9121654.

propagate throughout the metal, sampling the bulk properties of the nuclear spin system.[4] Pure resonance techniques are limited to sensing the spins inside of the skin depth, typically microns at MHz frequencies. We have chosen to study the heavy fermion compound $CeCu_6$ with a combination of ultrasound and NQR. This type of experiment is known as Acoustic Saturation NQR.[4]

At this time we have demonstrated the coupling between the ultrasound and the nuclear spin system. Our technique as well as some preliminary results are the subjects of this paper.

2.2 Experimental Details

The single crystal of $CeCu_6$ has polished faces that are oriented along the crystalline axes of the room temperature, orthorhombic, phase.

Four different piezoelectric transducers have been bonded to four faces of the crystal. The frequencies of the transducers were chosen to be equal to the frequencies of two of the ten zero-field NQR lines in $CeCu_6$[5] 6.8 MHz and 11.3 MHz. Two of the four transducers are AT-cut Quartz (one at each frequency). The remaining transducers are 11 MHz, longitudinal, $LiNbO_3$. The transducers were carefully bonded to the crystal with Dow Corning 200 fluid. They are held in place by 0.85 mm hard-line BeCu coaxial cable with a 90 degree bend at its end to provide the spring force. The center conductors were stiffened with epoxy. A very small NQR coil was wound over the transducers and can be tuned to match 50 ohms at any transition frequency.

2.3 Results and discussion

One goal of this work is to observe the increase in acoustic attenuation corresponding to the increase in NQR signal intensity at low temperature; however, in these preliminary experiments we are mainly concerned with the observation of a coupling to the nuclear spin systems. The first set of experiments that we have performed uses three different sets of pulse sequences. The first is a pure NQR pulse to determine the equilibrium signal amplitude at a given temperature. The second sequence involves the addition of an acoustic pulse just prior to the NQR pulse. The third sequence is identical to the first and serves as a check that the system has returned to its original state. For this set of experiments the sound was pulsed at 11.3 MHz and the NQR signals at both 11.3 and 6.8 MHz were monitored. The intensity of the signal at 11.3 MHz is dramatically reduced after the application of the sound (second pulse), whereas the intensity of the 6.8 MHz NQR signal is only slightly affected. Figure 2.1 shows the resulting NQR signal at 11.3 MHz following the first two pulse sequences. The larger signal shows the equilibrium signal size. Figure 2.2 shows the same pulse sequences for the 6.8 MHz NQR transition. We note that the reduction in the NQR signal is quite small. This measurement has also eliminated concerns about a pure heating effect. Measurements were made in a region were the measured spin-lattice relaxation times of the two transitions were approximately equal.[1] If the result of the sound pulse were simply to raise the electronic temperature of the sample, both nuclear spin systems should have their temperature raised and ratio of signals after pulses 1 and 2 should have been equal for both transitions. We consistently observed a stronger effect on the 11.3 MHz NQR line at temperatures down to 0.6 mK.

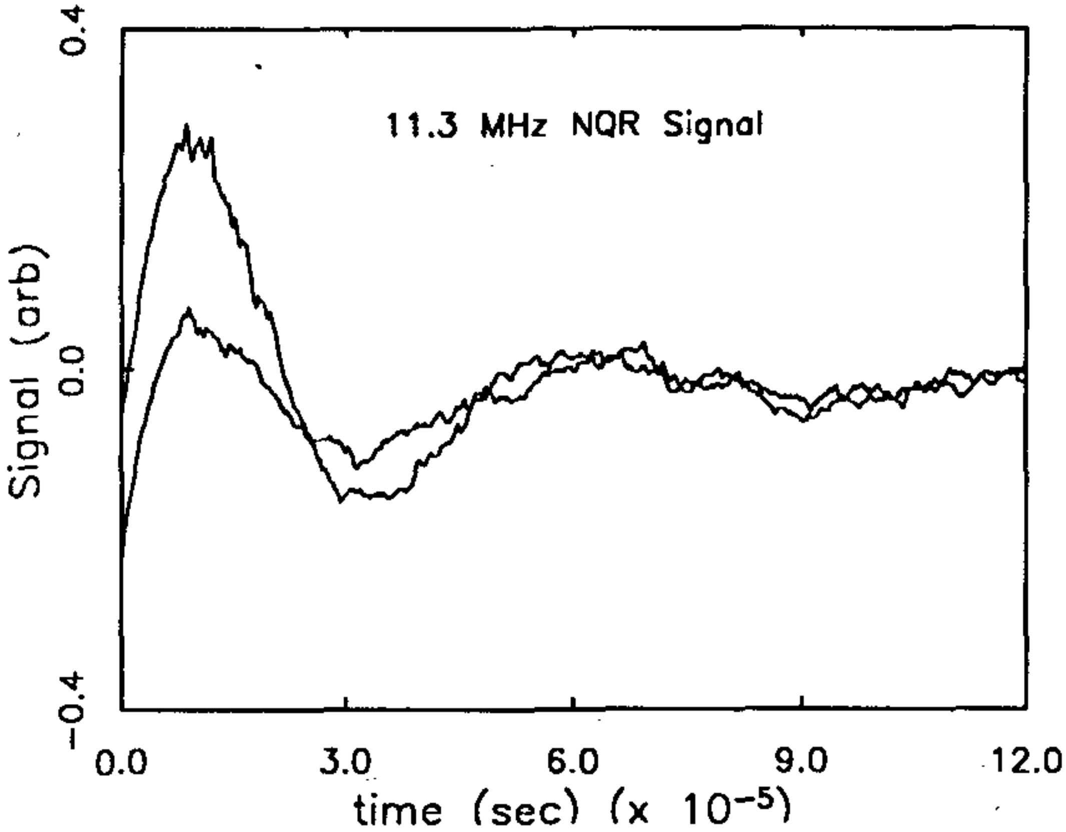

Figure 2.1: The effect of sound energy input at 11.3 MHz on the NQR signal with the same frequency. The large signal is the equilibrium signal at 4.4 mK; the smaller signal shows the reduction due to the effect of acoustic saturation.

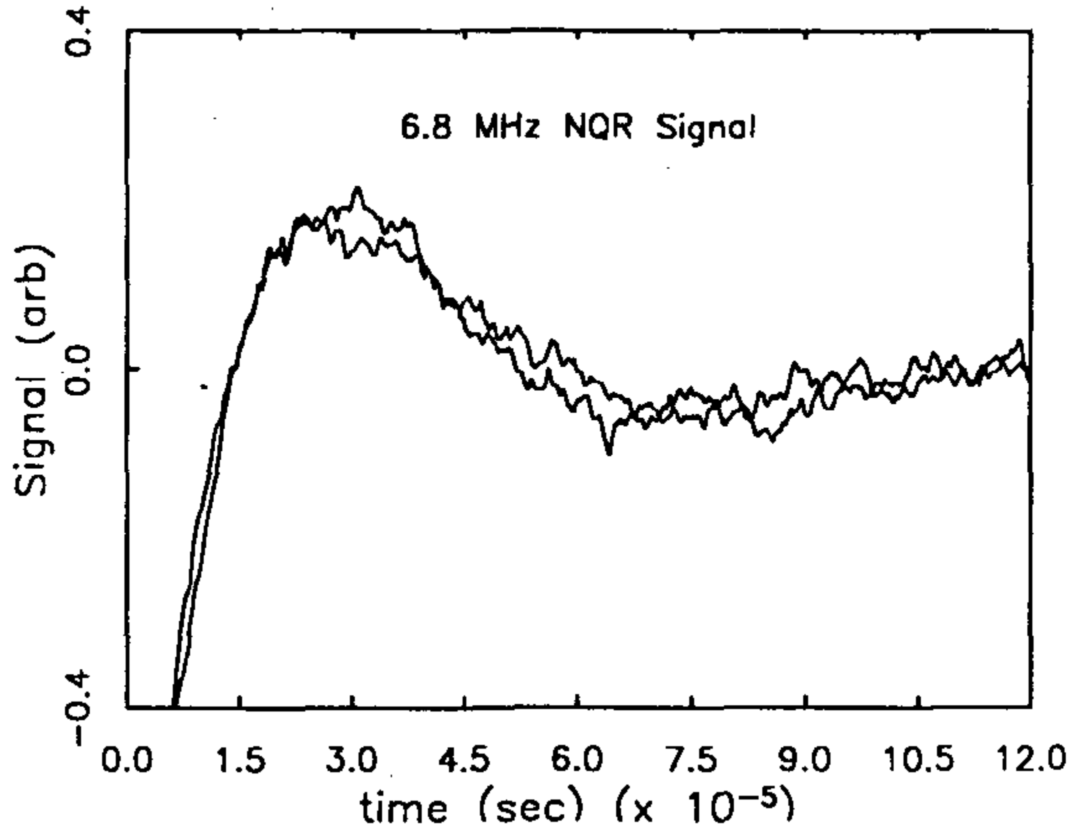

Figure 2.2: The effect of sound energy input at 11.3 MHz on the NQR line at 6.8 MHz. The large signal is the equilibrium signal at 4.4 mK; the smaller signal shows that the sound has a much smaller effect on the NQR signal at this frequency than at 11.3 MHz.

2.4 Conclusions

We have made the first measurements of ASNQR at ≈ 1 mK. We plan to refine this technique to allow to allow for measurements of the bulk properties of nuclear spin systems in metals.

REFERENCES FOR CHAPTER 2

[1] L. Pollack, M. J. Hoch, C. Jin, E. N. Smith, J. M. Parpia, D. L. Hawthorne, D. A. Geller, D. M. Lee, and R. C. Richardson, Phys. Rev. B, **52**, 707 (1995).

[2] W. Proctor and W. Tantilla, Phys. Rev., **98**, 1854 (1955).

[3] E. Gregory and H. Bömmel, Phys. Rev. Lett., **15**, 404 (1965).

[4] D. Bolef and R. Sundfors, *Nuclear Acoustic Resonance* (Acadimic Press, 1993).

[5] K. Kumagai *et al.*, Jpn. J. Appl. Phys., **26**, 533 (1987).

Part II

Spin wave phenomena: ^{3}He-^{4}He solutions and $CsNiF_3$

Chapter 3

Spin-polarized ^{3}He-^{4}He solutions: Longitudinal spin diffusion and nonlinear spin dynamics[†]

3.1 Abstract

Pulsed-NMR techniques have been used to investigate longitudinal spin diffusion and nonlinear spin dynamics in dilute, spin-polarized ^{3}He-^{4}He solutions between 4 and 400 mK. Solutions with ^{3}He concentrations $x_3 = 3.5$ x 10^{-4} and 19.4 x 10^{-4} were forcibly polarized to as much as 65% and 25%, respectively, with a 9.2-T magnetic field. A technique for measuring the coefficient of longitudinal spin diffusion $D_\parallel$ is described, and results of the technique are compared with recent theoretical calculations. Throughout a temperature range that covers both the degenerate and nondegenerate behaviors, theory and experiment are found to be in excellent quantitative agreement for $x_3 = 3.5$ x 10^{-4}, and somewhat weaker agreement for 19.4 x 10^{-4}. The presence of strong molecular fields in this system is confirmed by the observation of multiple spin echoes, but it is found that they are not adequately described by recent theory. In addition, the observation of a novel, extremely long-lived oscillation with a lifetime on the order of 10 sec is reported. These oscillations are found to have temperature sensitive and magnetic-field-gradient dependencies.

[†] Reprinted with permission from G. Nunes, Jr., C. Jin, D. L. Hawthorne, A. M. Putnam, and D. M. Lee, Phys. Rev. B., **46**, 9082 (1992).

A simple model which implies that this behavior is driven by a nonlinear instability is presented, and the results of numerical simulations based on this model are examined in an attempt to gain further insight into the spin dynamics of the system.

3.2 Introduction

The spin dynamics and transport properties of spin-polarized Fermi systems have been the subject of much recent experimental and theoretical interest.[1] Dilute solutions of ^{3}He in superfluid ^{4}He provide a nearly ideal system in which to carry out studies of such phenomena. They can be highly polarized at readily attainable magnetic fields and temperatures, and can be examined both in the degenerate ($T \ll T_F$) and classical, or Boltzmann, ($T \gg T_F$) regimes. They remain the only Fermi system that can be studied in the transition region between degenerate and classical behaviors. At the low concentrations of interest, the ^{3}He atoms are weakly interacting, and so form a quantum gas, rather than a strongly interacting liquid. This last point is particularly important from a theoretical point of view, as it greatly simplifies any calculation of the transport coefficients in the system.

Nonlinear spin diffusion in degenerate Fermi systems was examined by Leggett and Rice,[2,3] who showed that quantum exchange effects in pure (normal) ^{3}He give rise to a molecular field whose strength depends both on the degree of polarization, and on the details of the ^{3}He-^{3}He interactions. This molecular field cannot directly affect the precession of the local polarization $\mathbf{M}(\vec{r}$,t), since the two are constrained to be parallel. (In this paper we shall use boldface type to denote vectors in spin space. Real-space vectors, gradients, etc., will be denoted by arrows, or will have their Cartesian components written out explicitly.) The molecular field can, however, affect the spin *currents*, which then react back on $\mathbf{M}$ through the continuity equation. The relative importance of these exchange effects depends on the ratio of the spin-diffusion relaxation time τ_D to the time it takes a quasiparticle to execute a single precession (at frequency Ω_{int}) about the local molecular field. Following Leggett,[3] we can characterize the strength of this molecular field by the quantity $\mu M \equiv \Omega_{int}\tau_D$, where $M = |\mathbf{M}|$ is the degree of polarization, and μ is the dimensionless "spin rotation" parameter. If $\mu M \gg 1$, then a quasiparticle will execute many cycles about the local molecular field before being relaxed in a collision, and the exchange effects will be important. Leggett's predictions for the behavior of a $\phi \sim 180^\circ$ spin-echo experiment under these circumstances have been experimentally verified by Corruccini *et al.*[4] for both pure ^{3}He and concentrated ^{3}He-^{4}He mixtures.

More recently, Bashkin has argued that quantum exchange should lead to similar molecular-field effects in polarized systems which are at low temperatures, but still obey Boltzmann statistics, rather than degenerate quantum statistics.[5] In these systems, the thermal de Broglie wavelength Λ_T becomes much longer than the range of the interparticle potential (which at low temperatures we may take to be the s-wave scattering length a), so that quantum-mechanical corrections to the scattering become important. In an independent treatment, Lhuillier and Laloë[6] examined the effect of these quantum corrections in detail, and found that forward scattering exchange gives rise to an additional precession of the particle spins, which they termed "the identical spin rotation effect." Since this additional precession has the same effect on the spin dynamics as the molecular field in the degenerate Fermi liquid, it is entirely reasonable to find that Lhuillier and Laloë's nonlinear spin-diffusion equation for dilute gases is identical to that originally given by Leggett.[3]

The similarity of the spin dynamics in the low-density, weakly interacting gas to those in the high-density, strongly interacting liquid suggests that a more unified approach ought to be possible. Such a unified approach has, in fact, been carried out by Lévy and Ruckenstein,[7] who developed a quasiparticle description of paramagnetic Boltzmann gases that emphasizes their relation to more dense systems. They have successfully applied that approach to the results of experiments on spin-polarized atomic hydrogen gas.[8]

In both the degenerate and Boltzmann regimes, the essential effect of the molecular field on the spin dynamics can be seen from Leggett's equation for the steady-state spin currents in the Larmor (rotating) frame,

$$\vec{\mathbf{J}} = -D_s \vec{\nabla} \mathbf{M} - \vec{\mathbf{J}} \times \mu \mathbf{M}, \tag{3.1}$$

where D_S, is the coefficient of spin diffusion, $\vec{\nabla}$ is the real-space gradient operator, and the spin current $\vec{\mathbf{J}}$ has both spin and spatial vector components. From the second term on the right-hand side, it is apparent that, in addition to being driven by gradients in $\mathbf{M}$, the spin currents precess about the local molecular field $\mu\mathbf{M}$. The solution to this equation is easily found to be[3]

$$\vec{\mathbf{J}}(\vec{r}, t) = -\frac{D_s}{1 + \mu^2 M^2} [\vec{\nabla} \mathbf{M} + \mu (\mathbf{M} \times \vec{\nabla} \mathbf{M}) + \mu^2 (\mathbf{M} \cdot \vec{\nabla} \mathbf{M}) \mathbf{M}], \tag{3.2}$$

which, together with the continuity equation for the polarization (again, in the rotating frame)

$$\frac{\partial \mathbf{M}}{\partial t}(\vec{r}, t) + \vec{\nabla} \vec{\mathbf{J}}(\vec{r}, t) - \mathbf{M} \times \gamma \delta \mathbf{H}(\vec{r}) = 0, \tag{3.3}$$

completely defines the spin dynamics of the system. $\delta\mathbf{H}(\vec{r})$ is the residual (gradient) part of the applied field that is not removed by transforming to the rotating frame, and γ is the ^{3}He gyromagnetic ratio.

Given the complex form of these equations, it is not surprising that spin-polarized gases and liquids exhibit a rich variety of nonlinear phenomena. In addition to the spin-echo behavior verified by Corruccini *et al.*,[4] Eqs.(3.18) and (3.19) predict multiple spin echoes,[9] as well as spin waves. The latter have been observed in pure ^{3}He,[10] in concentrated (degenerate) ^{3}He-^{4}He solutions,[11,12,13] is as well as in spin-polarized atomic hydrogen[8] and ^{3}He (Ref. 14) gases. More recently, Candela *et al.* have observed spin waves in dilute ^{3}He-^{4}He solutions that are in the intermediate regime between the degenerate and classical limits.[15] The earliest investigation of such a highly polarized, intermediate regime ^{3}He-^{4}He solution, however, was undertaken by Gully and Mullin,[16] who carried out a Leggett-Rice-type $\phi \sim 180^\circ$ spin-echo experiment, which they analyzed to obtain both μM and D_s. At high temperatures, where the solution obeyed classical statistics, their measured values for these two quantities agreed well with theoretical predictions, and confirmed the presence of identical spin rotation effects in spin-polarized dilute solutions. At lower temperatures, where the system should cross over to degenerate behavior, however, they found that μM, instead of increasing more sharply with decreasing T, leveled off and even decreased at the lowest temperature. They also found that instead of making a smooth transition between an approximately $\sqrt{T}$ behavior at high temperatures and a $1/T^2$ dependence in the degenerate regime, began to fall quite sharply with decreasing temperature just at the point it might have been expected to level off or even increase.

A possible explanation for the unexpected behavior of both D, and μM was put forward by Meyerovich,[17] who argued that in a system that was both degenerate and spin polarized, the spin currents perpendicular (in spin space) to the direction of polarization should relax on a time scale $\tau_\perp$ significantly shorter than the relaxation time $\tau_\parallel$ for the parallel spin currents. As a result, the system should no longer have a single spin-diffusion coefficient, but rather two: $D_\perp$ for the relaxation of the transverse spin currents, and $D_\parallel$ for the relaxation of the longitudinal spin currents. Since a $\phi \sim 180^\circ$ type spin-echo experiment will only be sensitive to $D_\perp$, any interpretation of such an experiment based only on Leggett's original analysis may well encounter difficulties.

While the argument for anisotropic spin diffusion can be made on general grounds,[17,18] Jeon and Mullin[19] have shown that a more detailed treatment of the kinetics also gives two relaxation times, with $\tau_\perp \ll \tau_\parallel$ for small T/T_F and large M. They find that, under these conditions, Leggett's equation for the spin currents should be somewhat modified. If the spin-space unit vector $\hat{\ell}$ is defined such that $\mathbf{M} = M\hat{\ell}$, then Eq. (3.18) decouples into separate expressions for the longitudinal ($\vec{\mathbf{J}} \parallel \hat{\ell}$) and transverse ($\vec{\mathbf{J}} \perp \hat{\ell}$) spin currents. In the degenerate, spin-polarized regime, Jeon and Mullin find

$$\vec{\mathbf{J}}_\parallel = D_\parallel \overrightarrow{\nabla} M\hat{\ell} \tag{3.4}$$

and

$$\vec{\mathbf{J}}_\perp = -\frac{D_\perp}{1+\mu^2 M^2}[M\overrightarrow{\nabla}\hat{\ell} + +\mu M^2(\hat{\ell} \times \overrightarrow{\nabla}\hat{\ell})], \tag{3.5}$$

with (for example) $D_\perp \sim \frac{1}{2}D_\parallel$ at $T/T_F = 0.1$ if the system is 60% polarized.[19] At higher temperatures, where the system obeys Boltzmann statistics, $D_\perp = D_\parallel = D_S$, and the above expressions are equivalent to Leggett's result, Eq. (3.18).

As is evident from the form of the above equations, all of the nonlinear effects are confined to the transverse spin dynamics. In a system where $\mathbf{M}$ and gradients in $\mathbf{M}$ are purely longitudinal, the spin dynamics remain completely linear. Gradients in $\mathbf{M}$ (which we may treat as a scalar in the purely longitudinal case) will simply relax according to the ordinary diffusion equation:

$$\frac{\partial \mathbf{M}}{\partial t}(\vec{r}, t) = -D_\parallel \nabla^2 M(\vec{r}, t). \tag{3.6}$$

If one could develop a technique for measuring the coefficient of spin diffusion by exciting only longitudinal gradients, one could in principle measure $D_\parallel$ independently of $D_\perp$ (which could be obtained from a standard spin-echo experiment,[20,21]) and thereby search for the predicted diffusion anisotropy.

We have, in fact, developed such a technique for measuring $D_\parallel$ in dilute ^{3}He-^{4}He solutions, and in this paper we report on the results of that experiment. We also report on our investigations of the nonlinear transverse spin dynamics in the system, which include multiple spin echoes and a novel, extremely long-time-scale excitation. The next section of the paper is devoted to a discussion of our experimental techniques, including our method for determining $D_\parallel$. In Sec. 3 we give our results for $D_\parallel$ in two different solutions, and compare them with recent theoretical calculations. Section 4 contains a discussion of our multiple spin-echo experiments. In Sec. 5 we report on our observation of a new behavior in this system, with a characteristic lifetime on the order of 10 sec, and on our attempts to model that behavior with a simple computer simulation. Some of the results reported here have been previously published in a briefer form.[22]

3.3 Experimental Methods

3.3.1 General techniques

Experiments on spin-polarized ^{3}He-^{4}He solutions require both low temperatures and high magnetic fields. For the experiments described in this paper, the former were provided by a large dilution refrigerator (Oxford Instruments) with a base temperature of $\sim$ 3.5 mK. In order to reduce eddy current heating in the high-field regions, the cryostat was supported on a rigid platform of our own design with three high-performance vibration isolators (Technical Manufacturing Corporation). Vibrations transmitted along the refrigerator pumping lines were reduced by the installation of sandboxes and Kirk and Twerdochlib style double-gimbal isolators.[23]

The requisite high magnetic fields for these experiments were provided by a 9-T superconducting solenoid (American Magnetics) with a 7.5-cm bore and a field homogeneity of better than one part in 10^6 over a 1-cm^3 region at its center.

We determined the sample temperature using a ^{3}He melting curve thermometer and the Greywall temperature scale.[24] Figure 3.1 offers a general schematic view of the apparatus, and shows the relative position of the melting curve thermometer and sample cell. The thermal link between the mixing chamber and the sample cell was made long enough so that the temperature error due to the residual magnetic field at the melting curve thermometer (< 0.2 T) would be less than 0.5%.[25] The link was made from oxygen-free high-conductivity (OFHC) copper which had been annealed in an oxygen atmosphere (10 Torr partial pressure) for 8 h at 800°C to improve its thermal conductivity. After the annealing, the copper had easily visible crystallites on the order of 1–2 mm in size. Because of the high specific heat of the copper nuclei in the 9-T field, the sample cell had a 5–6 hour time constant at the lowest temperatures. As a result, we had to take particular care that the cell was in reasonable thermal equilibrium at the lowest temperatures. For our experiments on the higher concentration mixture, we added a vibrating wire viscometer to the sample cell, which allowed us to more readily ascertain that the cell had come to equilibrium.

Also shown in Fig. 3.1 is our z gradient coil, which was designed to apply a large (30 G/cm) uniform magnetic- field gradient $G = \partial H_z/\partial z$ to the sample cell. The coil was wound from Cu-clad multifilamentary Nb-Ti superconducting wire, and mounted on one of the thermal shields inside the refrigerator. The superconducting leads from the coil had their Cu cladding etched off in several places to reduce their thermal conductivity, and were brought out of the vacuum can and into the main bath space through an epoxy feedthrough.

The microwave cavity used in these experiments has been described in detail elsewhere.[26] Its design is based on the spit-ring resonator of Hardy and Whitehead,[27] but it employs a flexible metal-dielectric laminate that allows an extremely compact construction. It had a resonant frequency of 293 MHz, and a loaded Q of 1500 at low temperatures. The cavity was designed so that it could be tuned and coupled on a test rig that could be dipped into a helium storage Dewar, and then mounted onto the dilution refrigerator without further adjustment. Because of the large amount of power ($\sim$10 W) dissipated in the resonator during large tip angle pulses, it could not touch the sample cell. It was instead rigidly mounted close to the cell with low thermal conductivity Vespel rods (Dupont), and anchored to a higher-temperature stage of the refrigerator with a flexible copper braid.

While the high Q of the cavity allowed for an excellent NMR signal-to-noise ratio, it also resulted in a phenomenon known (somewhat misleadingly) as radiation damping.[28,29] In this situation the field of the precessing spins, as amplified by the cavity, is large enough to react back on the spin system and exert a torque on the magnetization vector. While this effect is usually associated with higher-density spin systems, the low spin density in our experiments was more than compensated for by the high degree of spin polarization. For most of our experiments, the effect was quite small and only led to a NMR line shape that depended somewhat on both temperature and tip angle. At low temperatures in our higher-density sample the effect did become large enough that after a 180° pulse the sample magnetization vector was immediately rotated back to nearly its equilibrium direction. We were able to get around this difficulty by adjusting the current in our magnet so that the resonant frequency of the ^{3}He atoms was far enough outside the cavity linewidth to significantly reduce the effective Q of the cavity, and thereby reduce the radiation damping.

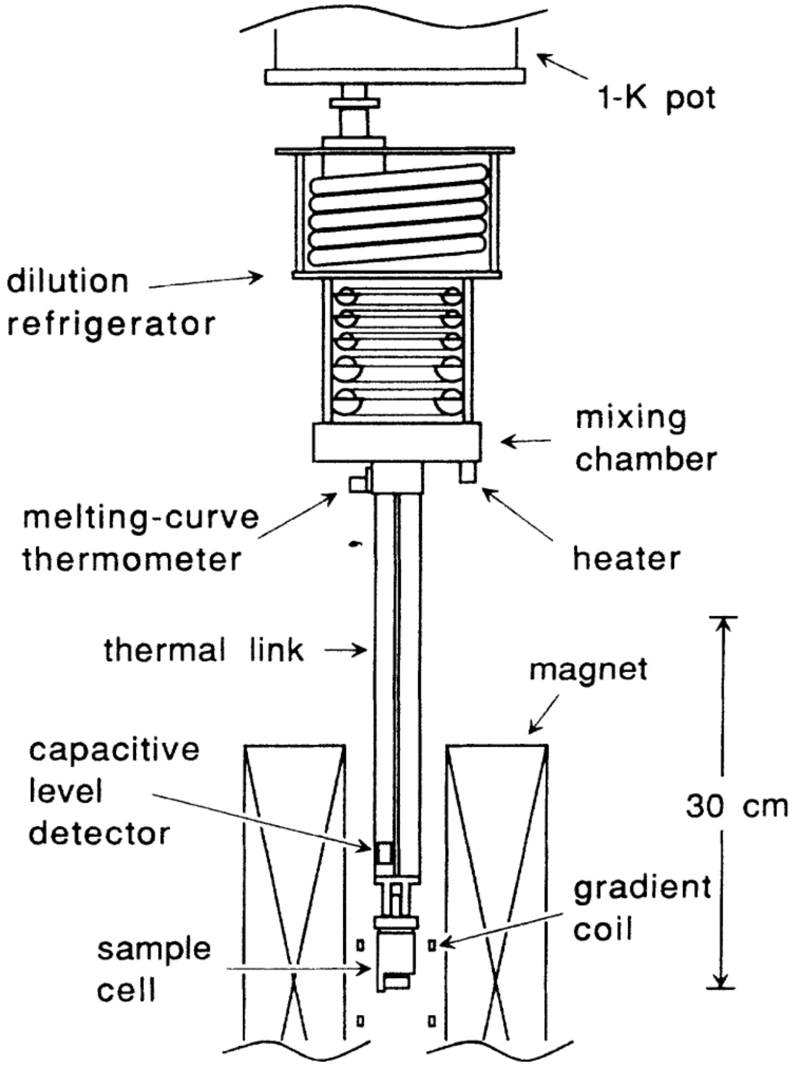

Figure 3.1: Schematic views of the low-temperature portion of the experimental apparatus.

The broadband pulsed NMR spectrometer used in these experiments was of a conventional design, and was built largely from commercially available components. It has been described in detail elsewhere.[30]

We prepared our ^{3}He-^{4}He solutions by means of a mixing system in which the ratio of a small volume ($\sim$155 cm^3) containing ^{3}He to a much larger one ($\sim$1.6x10^4 cm^3) containing ^{4}He had been carefully measured.[30] The sample concentration could then be determined from the initial pressure of ^{3}He in the small volume and the total pressure in the system once the two isotopes had been mixed. To minimize any errors that might result from an incomplete mixing, the total amount of sample was chosen so that, when liquefied, it would only exceed the known sample cell volume by a small amount. The mixed sample was then drawn into a charcoal cryopump and loaded into the sample cell while the latter was held at about 1.5 K. As the sample loading progressed, the cryopump was gradually warmed so as to maintain a pressure of 12 bar at the top of the cell-fill capillary.

It is a well-known property of superfluid ^{4}He that any temperature gradient in the liquid will cause a supercurrent to flow toward the higher-temperature regions. In our mixtures, the resulting counterflow of normal fluid would sweep all of the ^{3}He to the coldest spot and distort the concentration of the sample. To prevent this "heat flush" effect, we placed a capacitive level detector (shown in Fig. 3.1) in the sample cell-fill line. The capacitor was mounted on the thermal link, quite close to the cell, and was carefully monitored during the cell-filling procedure. When the changing capacitance of the level detector indicated that the sample's liquid-vapor interface was inside the detector, the filling procedure was halted, thus ensuring that none of the liquid extended up the fill line to warmer regions of the cryostat.

Two samples were prepared for the experiments described in this paper, one at a ^{3}He concentration of 350 ppm [T_F = 13.3 mK (Ref. 31)],[†] and a second at a

---

[†] We have used the ^{3}He effective mass $m^* = 2.255 m_3$ given by Ghozlan and Varoquaux, Ref.

concentration of 1940 ppm ($T_F = 41.4$ mK). As a check on the actual concentration, a portion of the mixed sample was transferred to a separate container and sent to the U. S. Bureau of Mines for analysis. Of the two samples sent for analysis, one was drawn from the completely mixed sample before loading any of the gas into the sample cell. It was mixed to have a concentration of 1820 ppm, but was measured by the Bureau of Mines to have a slightly ($\sim 5\%$) higher concentration of 1940 ± 40 ppm ^{3}He. The portion of the 350-ppm sample sent for analysis was actually taken from the gas remaining after the sample had been completely loaded, so we would expect it to be somewhat depleted of ^{3}He (which, with its higher vapor pressure, would come out of the cryopump first). The sample analyzed by the Bureau of Mines had a concentration of 300 ± 5 ppm ^{3}He, but it is our judgment that the concentration in the actual liquid sample was most likely within 5% of 350 ppm. In a 9.2-T magnetic field, the "brute force" polarization at the cryostat base temperature of 4 mK is 65% for the 350-ppm sample, and 25% for the 1940-ppm sample.[32]

3.3.2 Techniques for $D_\parallel$

Our technique for measuring $D_\parallel$ is based on the method of Johnson *et al.*,[8,33] who measured longitudinal spin diffusion in spin-polarized atomic hydrogen gas. The basic idea is quite simple. If we construct a sample cell with two chambers connected by a small channel, we can enclose one of these two chambers in a NMR coil or cavity. A π pulse applied to the cavity will then invert the spins in that chamber, and create a large longitudinal polarization gradient across the channel. Following the π pulse, spins will diffuse between the chambers until there is no longer any gradient, and the polarization in the two chambers will recover toward

---

31.

equilibrium. We can use the NMR cavity to apply small probe pulses and monitor this recovery as a function of time. If we can ignore T_1 (longitudinal relaxation) processes, then the recovery will be characterized by a single exponential time constant τ_0 that depends only on the geometry of the cell and the value of $D_{\|}$.

Of course, in any real experiment, the π pulse used to invert the magnetization will not be perfect, and will create some small amount of transverse magnetization. But because the applied static magnetic field is also not perfect, the transverse components in different parts of the cell will rapidly get out of phase, and – after a time T_2^* which is on the order of a few milliseconds – will average to zero. If the dimensions of the cell are chosen appropriately, τ_0 will be much longer than T_2^*, and any imperfections in the inversion will not matter.

A schematic drawing of the sample cell used in all the experiments described in this paper is shown in Fig. 3.2. The main body of the cell was constructed of Stycast 1266 epoxy (Emerson and Cuming). Thermal contact to the liquid was provided by a sintered silver heat exchanger with an area of approximately 25 m^3. The heat exchanger, which also served as the lid of the sample cell, was of a conventional "post and hole" design.[34] The 700- Å silver powder (Vacuum Metallurgical Co.) used to make the sinter was pressed in four separate steps to a 50% (by weight) packing fraction and a total thickness of 10 mm.

In the experiment as we have described it so far, the measured quantity is the time over which the magnetization in the lower chamber in Fig. 3.2 recovers to its initial value. To convert this time constant to a value for $D_{\|}$, we need to know the solution to the ordinary diffusion equation [Eq. (3.22)] for the cell. An exact analytical solution is quite likely impossible, given the complicated geometry of the cell. We can, however, easily find an approximate solution if, following Johnson, we make a few simplifying assumptions. Initially following the inversion of the spins

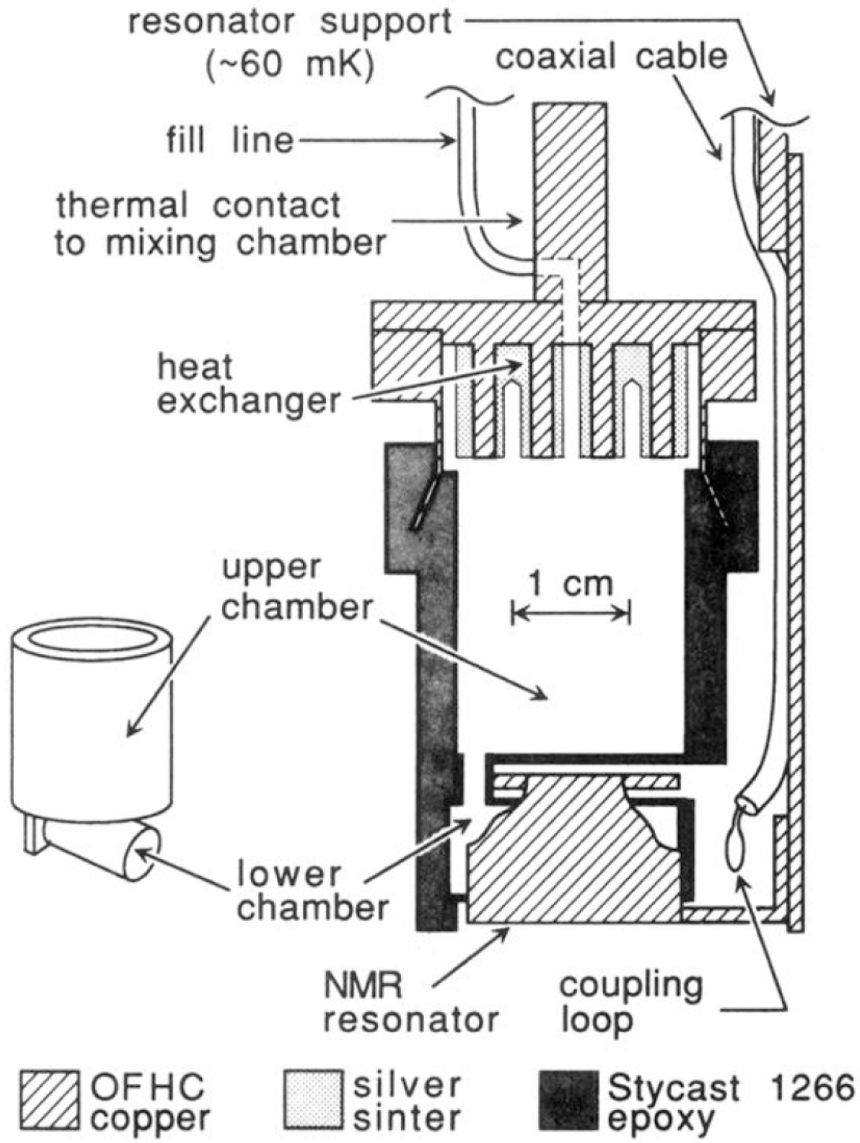

Figure 3.2: Schematic view of the sample cell. The relative orientation of the upper and lower chambers is indicated by the smaller figure on the left. The NMR resonator is shown partly cut away. Note that the resonator and its support do not touch the cell.

in the lower chamber (which we label volume 1), essentially all of the polarization gradient is along the length of the channel. Since the diameter of the channel is so small compared with the dimensions of the upper and lower cells, the gradient is likely to remain confined to the channel throughout the recovery, so it is not unreasonable to approximate the polarization as being completely uniform in the two chambers.

If we make the further approximation that the polarization is uniform across the diameter of the channel, and varies linearly along its length, then the total polarization flowing through the channel (per sec) is given by

$$I_M = D_{\parallel} \frac{\pi R^2 f}{L} (M_2 - M_1), \tag{3.7}$$

where M_2 is the (uniform) polarization in the upper chamber, R is the radius of the channel, and L is its length. The parameter f is a correction factor to take into account the fact that the gradients are not entirely confined to the channel. (Since we are assuming that any components of $\mathbf{M}$ that do not point in the z direction in spin space are small, we shall, for the moment, treat the polarization as a scalar quantity.)

If we can neglect T_1 processes (i.e., assume the total polarization in the cell is a conserved quantity), then any change in the polarization in the two chambers must be due entirely to the flow through the channel. It is then a straightforward matter to solve for M_1 as a function of time following a π pulse:

$$M_1(t) = M_f[1 - (1 + \epsilon)e^{-t/\tau 0}], \tag{3.8}$$

where M_f is the final polarization that both chambers relax toward, the polarization in the lower chamber at t = 0 has been defined as $M_1(0) \equiv -\epsilon M_f$, and the time constant for the exponential relaxation is given by

$$\frac{1}{\tau_0} = \frac{\pi R^2 f}{L} \frac{(V_1 + V_2)}{V_1 V_2} D_{\parallel}. \tag{3.9}$$

Table 3.1: The sample cell dimensions used in calculating the value of $D_{\parallel}\tau_0$ given in Eq. (3.11). The larger uncertainty in V_2 reflects the uncertainty associated with whether or not to include the open volume in the sinter. It makes only a very small contribution to the total uncertainty quoted in Eq. (3.11).

V_1	1.22 ± 0.01 cm^3
V_2	$10.5^{+1.4}_{-0.02}$ cm^3
R	0.122 ± 0.003 cm
L	0.36 ± 0.01 cm

Note that since $V_2 \gg V_1$, the time constant is relatively insensitive to the actual value of V_2, and therefore insensitive to whether it includes the open volume in the silver sinter heat exchanger.

To find a value for f, which corrects for the finite length of the channel, we note that the spin-diffusion problem we are considering is mathematically identical to the problem of electrical conductivity, providing that $D_{\parallel}$ is replaced by σ. In particular, if we model our cell as a small cylindrical wire connecting two semi-infinite electrodes, then we can use a result due to Maxwell[35] that the resistance of such a wire, including a "spreading resistance" correction for end effects, is given by

$$Z_e = \frac{L}{\pi R^2 \sigma}\left(1 + \frac{2\pi R}{3.82 L}\right) \tag{3.10}$$

Comparison with Eq. (3.7) shows that the quantity in parentheses above is just f^{-1}. In our cell, $L/R \simeq 3$, so that $f \simeq 0.64$ and this correction for end effects is relatively large. Putting the actual values for the length and radius of the channel and the volumes of the two chambers into Eqs. (3.9) and (3.10) (see Table 3.1), we find $D_{\parallel}\tau_0 = 13.03 \pm 0.56$ cm^2, where the uncertainty is due to our uncertainty in the dimensions of the sample cell.

In arriving at the above result, we have made a number of approximations, some of which may have been quite severe. In particular, the analytical treatment of the cell assumes that the channel is nicely centered and accessible from all directions, and thus entirely determines the impedance between the two chambers. In the real cell, however, the channel is off to one side, very close to the walls, and so there must be some additional impedance associated with its position in the cell. In an effort to correct for this "corner effect," we used a Monte Carlo computer simulation to solve the diffusion equation in our exact cell geometry.

The basic approach used in the program was quite simple. The model sample cell was filled with 235 "sample" atoms, each labeled by a position and a spin. Initially, all the atoms in the upper chamber had spin +1, and all those in the lower chamber had spin −1. For each run of the program, the initial positions of these atoms were chosen randomly from a uniform spatial distribution,

and the resulting configuration was simply "random walked" toward equilibrium.[30] The averaged results of 75 such runs are illustrated in Fig. 3.3. There are four curves shown in the figure: the polarization in the upper and lower chambers as given by the simulation (solid lines) and the same two quantities as given by least-squares fits to the data from the *upper* chamber only (dashed lines). There appear to be only three curves in the figure because, on this scale, the simulated data and the fit for the upper chamber are indistinguishable. (The curve for the lower chamber is much noisier because it is derived from a much smaller number of atoms.) From that fit we obtain the final result

$$D_{\|}\tau_0 = 14.14 \pm 0.75 \text{ cm}^2, \tag{3.11}$$

which is about 8% larger than the analytic result quoted above. The inset in Fig. 3.3 shows the distribution of time constants obtained from fitting each of the 75 runs separately. The uncertainty quoted in Eq. (3.11) was obtained from the variance of this distribution and the uncertainty in our knowledge of the exact dimensions of the cell.

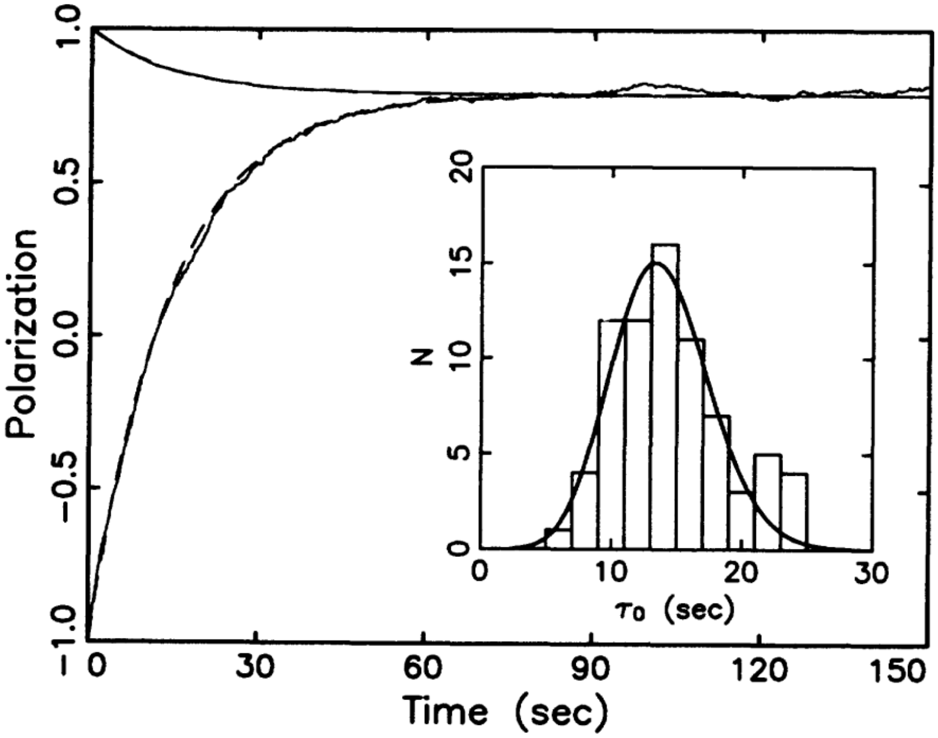

Figure 3.3: Averaged results from 75 runs of a Monte Carlo solution of the diffusion equation in the sample cell. Shown are the polarizations in the upper and lower chambers. The dashed line is a single exponential recovery with a time constant determined from a least-squares fit to the data in the *upper* cell only. On this scale, the data from the upper chamber and its fit are indistinguishable. The inset to the figure shows the distribution of time constants obtained from fitting the 75 runs separately. The solid line is a fit to a Poisson distribution.

So far we have made only passing reference to what is actually a very important approximation in our treatment: we have been assuming that we can neglect all longitudinal relaxation processes. In both our analytic and numerical solutions of the diffusion equation, we assumed that the system would relax toward a final state in which the spins in the two chambers had completely mixed, but had not yet returned to thermal equilibrium. Our assumed final state has only $\sim 90\%$ of the polarization initially in the sample before the population in the lower chamber was inverted. True thermal equilibrium will be regained through longitudinal relaxation processes with a time constant T_1, and the relative magnitude of T_1 and τ_0 will determine whether it is possible to correctly extract $D_\parallel$ from our measurements. In particular, we require $T_1 \gg \tau_0$ in the lower chamber of the cell.

In principle, we could make a direct measurement of T_1 in our cell by saturating the spins in the lower chamber with a continuous string of 90° pulses. After a time $\sim 10\tau_0$, the magnetization in the upper and lower chambers would have completely exchanged, so that monitoring the recovery of the magnetization (once the 90° pulses have been stopped) should give T_1. In practice, however, the relatively fast relaxation in the large surface area heat exchanger[36] makes it impossible for the slowly diffusing spins from the lower chamber to saturate the upper regions of the cell. We must instead rely on estimates of T_1 derived from the literature.

From the dimensions of our sample cell and the expected magnitude of the diffusion coefficient, it is easy to see that an atom will, on average, make several collisions with the cell wall during a time τ_0. Therefore, we must consider relaxation processes that occur at the wall of the sample cell, as well as those that occur in the bulk liquid. If we consider the two processes to add in parallel, then the total relaxation time T_1 will be given by

$$\frac{1}{T_1} = \frac{1}{T_{1B}} + \frac{1}{T_{1W}}, \tag{3.12}$$

where T_{1B} and T_{1W} are the relaxation times associated with bulk and wall processes, respectively.

In liquids and gases, bulk relaxation occurs as a result of the dipolar interaction during the brief interval that a pair of colliding spins are within a scattering length of each other.[37] Quite recently, Mullin, Laloë, and Richards[38] reexamined this mechanism for the case of a quantum gas, and found that the relevant length scale is not the scattering length, but the thermal de Broglie wavelength of the atoms. Their results predict that for a 2000-ppm solution of ^{3}He in ^{4}He at 0.5 K, $T_{1B} \sim 4 \text{ x } 10^5$ sec, which is very much longer than our expected τ_0. Since the dependence of their result on temperature and ^{3}He density is such that we would expect the relaxation time to become even longer at lower concentrations and lower temperatures, we may effectively neglect bulk processes in our consideration of T_1.

The relaxation of ^{3}He nuclei at surfaces has long been considered anomalous and remains a problem without an adequate theoretical description (see Ref. 39 and references therein). It has been empirically determined, however, that T_{1W} depends linearly on the applied magnetic field,[40,41] and that covering the surface with ^{4}He increases T_{1W} by a factor of 10-100.[40,42] If we use the data of Hammel and Richardson[39] for the T_{1W} of pure ^{3}He taken in the temperature range of our experiment and on a DLX6000 substrate,[†] and scale them to account for our much larger magnetic field and for the presence of ^{4}He in our system, we find that in the lower chamber of our sample cell $T_{1W} \sim 10^7$ sec. Although this estimate is rough at best, it is significantly longer than either our estimate for the bulk relaxation time or our observed τ_0. Taken together, our estimates for T_{1B} and T_{1W} give us a high degree of confidence that our measurements of τ_0 will not be significantly affected by relaxation processes.

[†] DLX6000 is a Teflon-like polymer containing paramagnetic spins (^{19}F) whose magnetic moment and density are not too different from the those of the protons in the sample cell epoxy. DLX6000 and Teflon are registered trademarks of the Dupont corporation.

3.3.3 Longitudinal Spin Diffusion

While our discussion and analysis of the sample cell and relaxation processes has been extended, the actual measurements of $D_{\|}$ were quite straightforward. At a given temperature, we applied a π pulse to the spins in the lower chamber, followed by a series of 45 small probe pulses. The tipping angle of the probe pulses ($\frac{1}{2}^{\circ}$) was chosen to be sufficiently small so that their cumulative effect on the total polarization would be negligible. The free induction decay (FID) following each probe pulse was mixed down from 300 MHz to an audiofrequency ~10 kHz, digitized, and stored for later analysis. For reasons we shall discuss in Sec. 5, these measurements were made with a small (~0.3 G/cm) magnetic-field gradient applied across the cell.

To obtain a number proportional to $M_z(t_n)$, where t_n is the time of the n^{th} probe pulse in the series, we used a least-squares-fitting procedure. To prevent transients in the spectrometer electronics from affecting the results, the first 50 μsec of the FID were discarded and the fit was made to the next 2.5 msec of signal. The parameters obtained from the fit were then extrapolated back to obtain the signal amplitude at t_n. Because the lower chamber in the sample cell is somewhat larger than the manufacturer specified high homogeneity "region" in the center of the magnet, and because of the radiation damping contribution to the line shape we discussed earlier, we found it necessary to fit the signals to a sum of two exponentially damped cosines, which we did by a linear prediction technique.[43] The fits typically found a fast decay rate with a time constant on the order of 0.3 msec, and a slow decay with a time constant of 23 msec.

The 45 amplitudes were then fit to an exponential recovery of the form given by Eq. (3.8). Figure 3.4 shows a comparison of a typical recovery with its fit for data taken on a 1940-ppm solution. Also shown are the deviations from the fit. If the recovery were not well characterized by a single exponential, then the deviations should systematically lie to one side of zero around the “knee” of the curve, and to the other side at later times. Such behavior was not observed.

At each temperature, we averaged the results of four such recoveries to obtain a value for τ_0 from which, using Eq. (3.11), we computed $D_\parallel$. Figure 3.5(a) shows our results for $D_\parallel$ between 4 and 400 mK in the 350-ppm solution. The error bars are derived from the fits and do not include the overall 5% uncertainty in our value of $D_\parallel \tau_0$ that comes from the uncertainty in the exact cell geometry and from the solution of the diffusion equation for the cell. Shown superimposed on the data is the theoretical calculation of Jeon and Mullin[44] appropriate to our field and concentration. The only parameter they have adjusted to improve the agreement between their theory and our experiment is the strength of the ^{3}He-^{3}He interaction potential V_0, which has been increased by about 4% over the value originally used by Ebner.[45] The main effect of this adjustment is a slight vertical shift in the calculated values of $D_\parallel$, but even without it, the agreement between our data and the calculation would still be well within the combined theoretical and experimental uncertainty.

In contrast to the results of the experiment by Gully and Mullin,[16] we find that $D_\parallel$ does in fact make a smooth transition between the expected high and low temperature behaviors, although we cannot quite reach low enough temperatures for $D_\parallel$ to exhibit the $1/T$ behavior characteristic of a fully degenerate Fermi system.

An important limitation of this technique for measuring $D_\parallel$, which we have not so far discussed, is that our treatment of the sample cell assumes that the diffusion coefficient is uniform throughout the cell. In particular, since the polarization in the channel immediately after the inversion is a rapidly changing function of position, this technique requires that $D_\parallel$ be, at most, weakly dependent on M, as

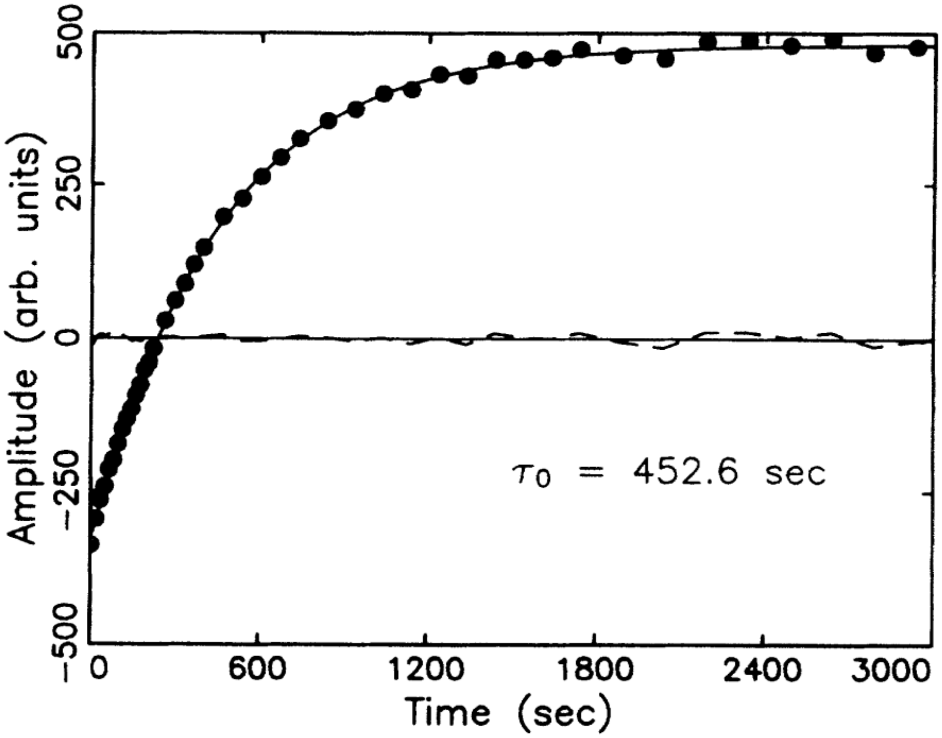

Figure 3.4: The results of a single measurement of τ_0 in a 1940-ppm solution at 54.6 mK. The solid circles are the signal amplitudes following each of the 45 probe pulses, and the solid line is a least-squares fit to a single exponential recovery. The dashed line shows the deviations from the fit.

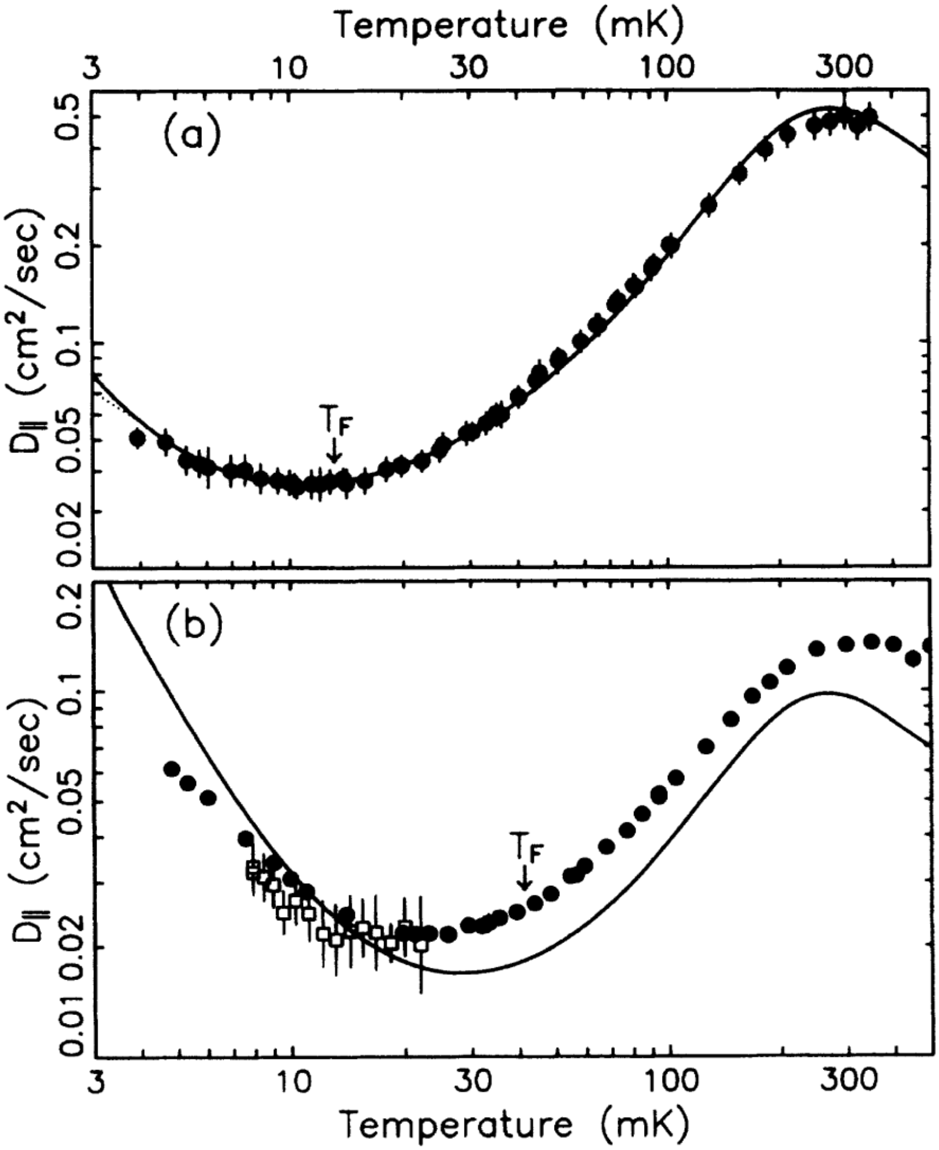

Figure 3.5: Measured values of $D_\parallel$ at 0 bar in a 9.2-T field (solid circles) compared with the calculation of Jeon and Mullin (Ref. 45) (solid lines) using the ^{3}He-^{3}He potential of Ref. 46. The error bars shown are derived from the least- squares fits, and do not reflect the overall 5% uncertainty in the product $D_\parallel \tau_0$. (a) Results for a 350-ppm solution. The dotted line at low temperatures indicates the predicted (Ref. 45) dependence of $D_\perp$ at this concentration and magnetic field. (b) Results for a 1940-ppm solution. Also shown are the results of Candela *et al.* (Ref. 15) for $D_\perp$ (open squares) in an 1840-ppm mixture.

has been pointed out by Bowley.[46] From a detailed comparison of Jeon and Mullin's calculations, which include mean-field effects, for H = 9 T and H = 0 T over the temperature range of our experiments, we find that the polarization dependence of $D_\parallel$ only becomes significant below 10 mK, and even then, the predicted difference between $D_\parallel$ (0 T) and $D_\parallel$(9 T) is much smaller than our uncertainty in $D_\parallel \tau_0$. Any attempt to extend these measurements to lower temperatures, however, may well have to take the polarization dependence of $D_\parallel$ into account.

Since one of the original motivations for this experiment was to look for a discrepancy between $D_\parallel$ and some independent measure of $D_\perp$, it would be nice, at this point, to be able to make a comparison between the two. As we shall discuss in Sec. 4, however, our attempts to measure $D_\perp$ with a spin-echo technique were greatly complicated by the strong molecular field effects in the system. In addition, recent calculations by Jeon and Mullin, shown as the dotted line at very low temperatures in Fig. 3.5(a), indicate that, for our 350-ppm solution, $D_\perp$ should only be observably different from $D_\parallel$ below the temperature range accessible with our current apparatus.

As an alternative approach to the problem of diffusion anisotropy, we decided to take advantage of the recent experiments by Candela *et al.*[15] in which a spin-wave technique was used to measure μM and the quantity $D_\perp/\mu M$ in an 1820-ppm solution. While our attempt to match exactly that concentration missed by about 100 ppm, the difference between the Fermi temperature of our 1940- ppm solution (41.4 mK) and that of the solution studied by Candela et at. (39.7 mK) is negligible, given the resolution of our respective experiments.

Figure 3.5(b) compares our results for $D_\parallel$ (solid circles) in the 1940-ppm solution with $D_\perp$ as extracted from the data of Candela *et al.* (open squares). While at low temperatures their data fall consistently below ours, the uncertainties in both experiments are too large for us to claim that the discrepancy is due to diffusion anisotropy. In particular, while the difference between the data from the two experiments has the correct sign, and is slightly more than the theoretically predicted difference of 34% between $D_\parallel$ and $D_\perp$, it is still less than the combined uncertainty of 7–10% from the two experiments.

Also shown in Fig. 3.5(b) is the same theoretical calculation of $D_\parallel$ (with the same value of V_0) by Jeon and Mullin[44] as was compared with our 350-ppm results, but adjusted for the higher concentration. Although the data and theory have a similar temperature dependence, the quantitative agreement is not nearly as good as for the low-concentration experiment. The reasons for the discrepancy in this case are not understood. It is interesting to note that the two sets of experimental measurements seem to agree with each other better than either one agrees with the theory. It may be that the problem lies with the use of the Ebner potential to describe the ^{3}He-^{3}He interactions; however, that potential was determined from experimental data at an even higher concentration (5%), and it would be very surprising to find that it did a poor job at 1940 ppm but worked again at 350 ppm. Further work, both experimental and theoretical, will be needed to resolve this disagreement.

3.4 Multiple Spin Echoes

3.4.1 Theory

Ordinary spin echoes are a well understood and widely used technique in magnetic resonance in which a pair of rf pulses (θ_1 and θ_2) applied to a system of spins at times $t = 0$ and $t = \tau$ result in a signal at $t = 2\tau$. The decay in the height of this "echo" signal as τ is increased can be used as a probe of spin diffusion in the system. Since the spin echo is built up from transverse magnetization created by the first pulse, the spin-diffusion coefficient determined from such a measurement will, of necessity, be $D_\perp$. It is easy to show (see, for example, Ref. 21) that if T_2 is sufficiently long, i.e., if transverse relaxation may be neglected, the height of the echo will be proportional to

$$e^{-\frac{2}{3}D^*} \equiv e^{-[\frac{2}{3}D_\perp(\gamma G)^2\tau^3]}, \tag{3.13}$$

where $G \equiv \partial H_0/\partial z$ is an applied linear gradient large enough to dominate any unknown contributions from imperfections in the magnet, etc. If the system is linear, then there will be no further echoes unless additional rf pulses are applied.

In systems with a strong molecular field, the simple behavior described by Eq. (3.13) no longer applies, as was first pointed out by Leggett and Rice. In particular, they showed that for the case that $\theta_2 = 180°$, the dependence of the echo heights on the dimensionless parameter $D^* = D_\perp(\gamma G)^2\tau^3$ is no longer exponential. Their predictions were fully verified by Corruccini *et al.*[4] for the case of pure ^{3}He, but a similar experiment on a highly polarized ^{3}He-^{4}He mixture by Gully and Mullin[16] led to the anomalous results for both $D_\perp$ and μM which we discussed in Sec. 1.

If the second pulse in the sequence is not a π pulse, then the nonlinearities introduced by the molecular field can lead to the phenomenon of multiple spin echoes (MSE) in which *additional* echoes at times $t = n\tau, n = 3, 4, \ldots$ appear in response to the original θ_1-τ-θ_2 pulse sequence. Such multiple echoes are a fairly general phenomenon in which the nonlinear spin dynamics lead to a spatially modulated precession frequency. They were first observed in solid ^{3}He,[47] and subsequently in both superfluid[48] and normal[9] liquid ^{3}He, as well as in spin-polarized hydrogen gas.[49] Recently, they have even been observed in water at room temperature.[50]

In the case of solid ^{3}He, the nonlinear mechanism that drives the MSE results from a large internal dipolar demagnetizing field. Such a (considerably weaker) demagnetizing field is also responsible for the MSE observed in water. In their experiments on normal liquid ^{3}He, Einzel *et al.* found two regimes: a high-temperature one in which the multiple echoes were driven by a dipolar field, and a low-temperature regime in which the MSE were driven by an exchange molecular field. In the dilute solutions reported on here, it is this latter mechanism that is of interest; the spin density in these solutions is so low as to rule out any significant dipolar field effects.

The response of our 350-ppm sample to a $90°$-τ-$90°$ pulse sequence is illustrated in Fig. 3.6. In this instance, in which the delay between the pulses was 1 msec, G (applied with the coil illustrated in Fig. 3.1) was 3 G/cm, and the temperature was 10.6 mK, there are 23 echoes visible. Note that although the second echo is large, successive echoes at first decrease in amplitude until, by the fifth echo, there is no signal at all. At later times the echo heights grow again and by the 12^{th} echo are almost as large as the first multiple (i.e. , second) echo.

We may understand the origin of these multiple spin echoes in a very general way by briefly summarizing the analysis made by Einzel *et al.*[9] The first rf pulse (which we will consider to occur at $t = \tau$ creates a transverse component of magnetization which precesses in the applied magnetic field. Because of the large linear gradient included in that field, the magnetization will twist up into a helix along the z (magnetic field) axis in the sample cell. The pitch length of this helix at the time of the second pulse ($t = 0$) will be given by $l_p = 2\pi/\gamma G\tau$. Following this second pulse, the magnetization will have some complicated spatial structure, but will still have an underlying periodicity given by l_p. Since Einzel *et al.* expected the nonlinearities in the system to introduce higher harmonics of this periodicity, they sought a solution for the further time evolution of $M_+ = M_x + iM_y$ in the

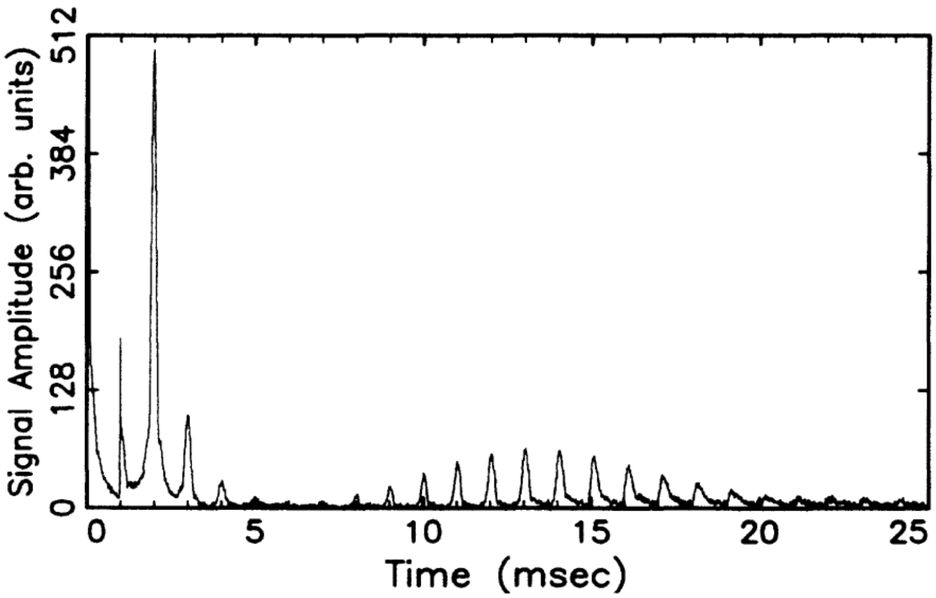

Figure 3.6: Multiple spin echoes at 10.6 mK. The delay between the two 5-μsec 90° pulses was 1 msec, and the magnetic- field gradient in the z direction (parallel to H_0) was 3 G/cm. The signals at $t = 0$ and $t = 1$ msec are the free induction decays from the rf pulses. The remaining peaks are the spin echoes.

form of a power series in $\exp(2\pi z/l_p)$:

$$M_+(z,t) = M_0 e^{-i\gamma G z t} \sum_{n=-\infty}^{\infty} A_n e^{iG\gamma z n\tau}. \tag{3.14}$$

Any signal detected in the experiment will be a spatial average of M_+ over the volume enclosed by the rf cavity. From the two rapidly oscillating factors in Eq. (3.14), we can see that this average will generally be zero, except when t happens to be an integer multiple of τ. Then the precession term will be exactly canceled by the term in the power series with $n\tau = t$, and there will be a net signal (spin echo) whose amplitude is determined by the coefficient $A_n(n\tau)$. It is worth emphasizing that the form of Eq. (3.14) is quite general. All of the model-dependent parameters are manifested in the A_n, which can only be found by solution of the appropriate nonlinear equations for the spin dynamics.

For the case that both longitudinal and transverse relaxation processes can be neglected (i.e., T_1 and T_2 are very long compared to the duration of the echo train), Einzel *et al.*[9] worked out analytic expressions for the in two limiting cases. Of particular interest here is their result for the case in which the MSE arise from molecular-field (exchange) effects. They find that, providing $\mu M \ll 1$, the height of the second echo is given by

$$A_2(2\tau) = \mu M_0 \sin^2\theta_1 \sin\theta_2 (1 - \cos\theta_2) \times D^* e^{-7D^*/3} \sum_{n=0}^{\infty} \frac{(-D^*)^n}{n!(2n+1)(2n+3)}. \tag{3.15}$$

Quite recently, Bedford *et al.*[51] have rederived these results and have shown how the system may be treated numerically to obtain the echo heights when μM is not necessarily small, as well as when both dipolar and exchange mechanisms are important (as is the case in pure ^{3}He around 10 mK). They have also applied their results to experimental data on dilute ^{3}He-^{4}He solutions[52] and find that, in the limit that $\mu M \lesssim 1.5$, the agreement between theory and experiment is very good.

Before turning to a discussion of our MSE data, we wish to emphasize that both the analytic result Eq. (3.15) and the numerical results of Bedford *et al.* predict the echo heights to be a universal function of the parameter D^*. That is to say, if we compare spin-echo data taken at different magnetic-field gradients, all of the (properly normalized) heights obtained for the first (ordinary) spin echo should collapse onto a single curve if plotted against $G^2\tau^3$, which is proportional to D^*. Similarly, the second (first multiple) echo heights should lie on a single curve, and so on. In addition, the second echo height, as given by Eq. (3.15), should have a single maximum as a function of D^*.

3.4.2 Experiment

We obtained multiple spin-echo data using $90°$-τ-$90°$ pulse sequences over a range of τ and a range of applied magnetic field gradients at several different temperatures. While we observed MSE in both the 350-ppm and 1940-ppm solutions, all of the results reported here were obtained from the lower concentration sample. We extracted the individual echo heights (which we denote E_1 for the first echo, E_2 for the second, etc.) from each digitized echo train, and normalized them to $E_1(0)$: the value of E_1 at $t = 0$ for that train. We obtained $E_1(0)$ by a backwards extrapolation of $\ln(E_i)$ against τ^3.[51] Although we could observe a second (i.e., first multiple) echo at temperatures as high as 60 mK, the MSE weakened relatively quickly with increasing temperature.

Figure 3.7(a) shows the results of our measurements of the first echo amplitude at 5.1 mK for gradients of 1, 2, 3, and 4 G/cm. The parameter D^* was calculated according to Eq. (3.13) from the gradient, the delay, and our measured value of $D_{\|}$ at that temperature. The dashed lines are intended only as guides to the eye. It is obvious that, contrary to the expectations discussed in Sec. 4.1, the echo height data taken at different gradients do not fall onto a single curve. We also find that the data taken at the individual gradients do not fall onto straight lines, which indicates that the decay of the echo heights with increasing D^* is not exponential.

As we mentioned earlier, the latter is an expected result, and is due to the Leggett-Rice effect.[2,3] An additional aspect of the Leggett-Rice effect is the "slowing down" of spin diffusion for the transverse components of the polarization. This slowing down is a direct consequence of the spin rotation (or molecular field) effects in the system. It has the effect of stretching out the time scale of the echo train since, roughly speaking, $D_\perp$ in Eq. (3.13) is replaced by an "effective" diffusion coefficient

$$\widetilde{D}_\perp = \frac{D_\perp}{1 + \mu^2 M^2}. \tag{3.16}$$

The importance of this effective diffusion coefficient can be seen in Fig. 3.7(b), which shows the behavior of the second echo at the same applied field gradients as in Fig. 3.7(a). The data taken at each gradient has only a single maximum as function of D^*, as predicted by theory. The positions of these four maxima (indicated by arrows) do not coincide, and they all occur at a much larger value of D^* than is predicted by Eq. (3.15), which has a maximum at $\mathrm{D}^* \approx 0.4$. Since this equation is only applicable for small μM (i.e., for $\widetilde{D}_\perp \simeq D_\perp$), it is apparent that the diffusion has indeed been slowed by the molecular field so that $\widetilde{D}_\perp \ll D_\perp$. Since we have calculated D^* without taking into account this smaller effective diffusion coefficient, our data are "stretched" along the horizontal axis.

It seems, however, from the way in which the positions of the echo height maxima depend on G [see the inset to Fig. 3.7(b)], that this effective diffusion coefficient is a function of the applied gradient. There appears to be a similar effect in the way in which the expected universal dependence on D^* fails for the first echo [see Fig. 3.7(a)]. In both cases, the data taken at larger gradients appear

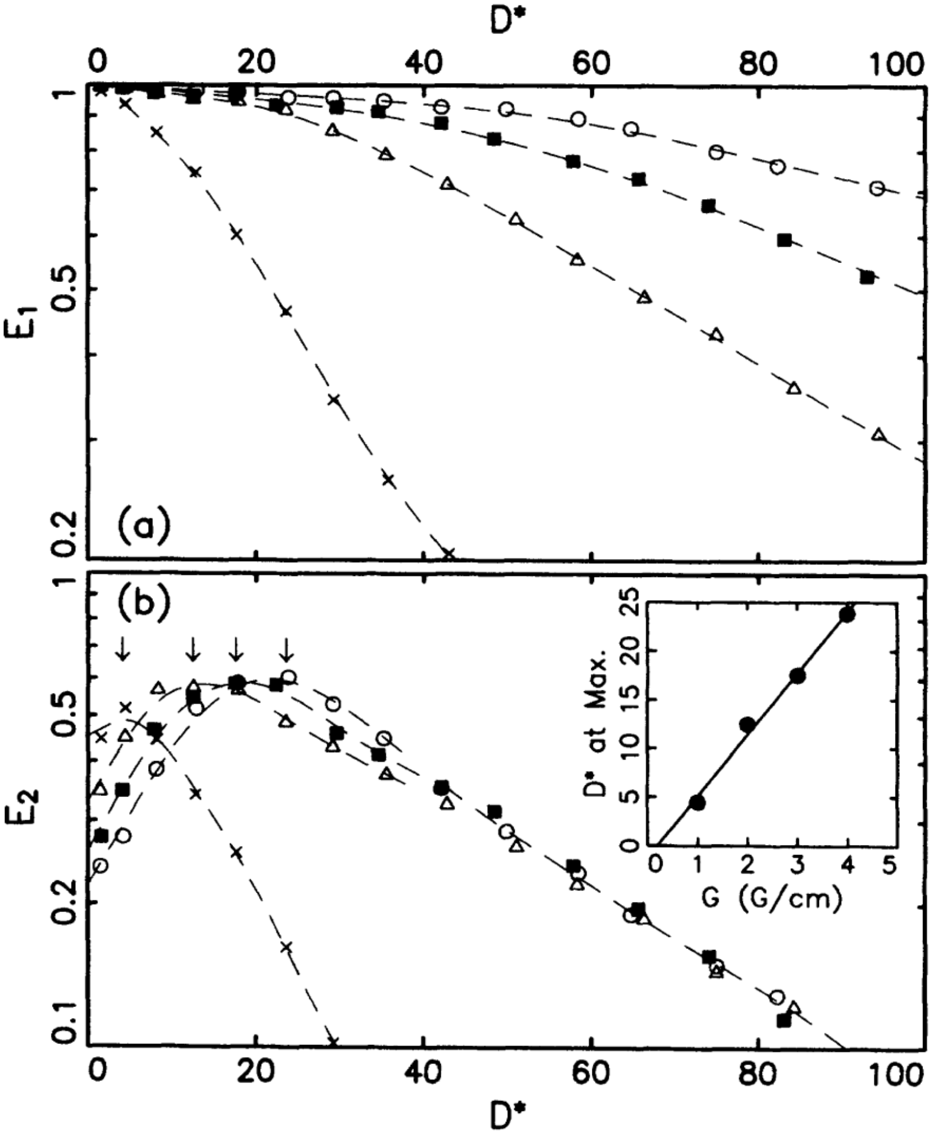

Figure 3.7: Normalized (a) first echo and (b) second echo amplitudes as a function of the dimensionless parameter $D^* = D_{perp}(\gamma G)^2\tau^3$ at 5.1 mK. The data shown were taken at the following magnetic-field gradients: × = 1 G/cm, △ = 2 G/cm, ■ = 3 G/cm, and ◯ = 4 G/cm. The dashed lines are intended only as guides to the eye. Inset: The positions of the second echo maxima (indicated by arrows) as a function of field gradient.

to have a much smaller effective diffusion coefficient, which we see from Eq. (3.16) is equivalent to a much larger molecular field.

The amplitudes of the third and later echoes also exhibit somewhat unexpected behavior. Figure 3.8 shows the results of a high-resolution scan in which successive delay values were very closely spaced. The data were taken at 5.1 mK in an applied gradient of 4 G/cm, and show the normalized amplitude of the second, third, and fourth echoes, as a function of D^*. Note that while the second echo has a single broad maximum, the third echo has a sharp minimum, and the fourth echo has two. While these minima are not predicted by the analytic theory for small μM, the numerical treatment of Bedford *et al.* does in fact exhibit qualitatively similar behavior for large molecular fields ($\mu M \gtrsim 5$).[53]

While we would like to fit the results of Bedford *et al.* to our echo heights to obtain both $D_\perp$ and μ, such an approach is bound to prove unfruitful, given the way in which our present data fail to scale with gradient and delay. Since the parameters of interest enter D^* approximately as the ratio $D_\perp/\mu^2$, a fit to the data at any one gradient would return values for $D_\perp$ and μ, which would be inconsistent with the data taken at other gradients. At this point, we have no way of determining which data set (if any) represents the "true" dependence on D^*.

A likely explanation for the nonuniversal behavior of the multiple spin echoes in our experiment can be found in the experiments of Owers-Bradley *et al.*[52] who studied both MSE and the Leggett-Rice effect in ^{3}He-^{3}He solutions where $\mu M \lesssim 2$. They found that they were unable to fit their results to the theory unless they took particular care to ensure that the magnetic-field gradient across the cell was extremely uniform, and that the cell diameter d was very small so that $Gd/H_1 \ll 1$. (H_1 is the rf magnetic field in the resonator during a pulse.) Even then, they found that they had to limit the magnetic field applied to the system so as to keep the

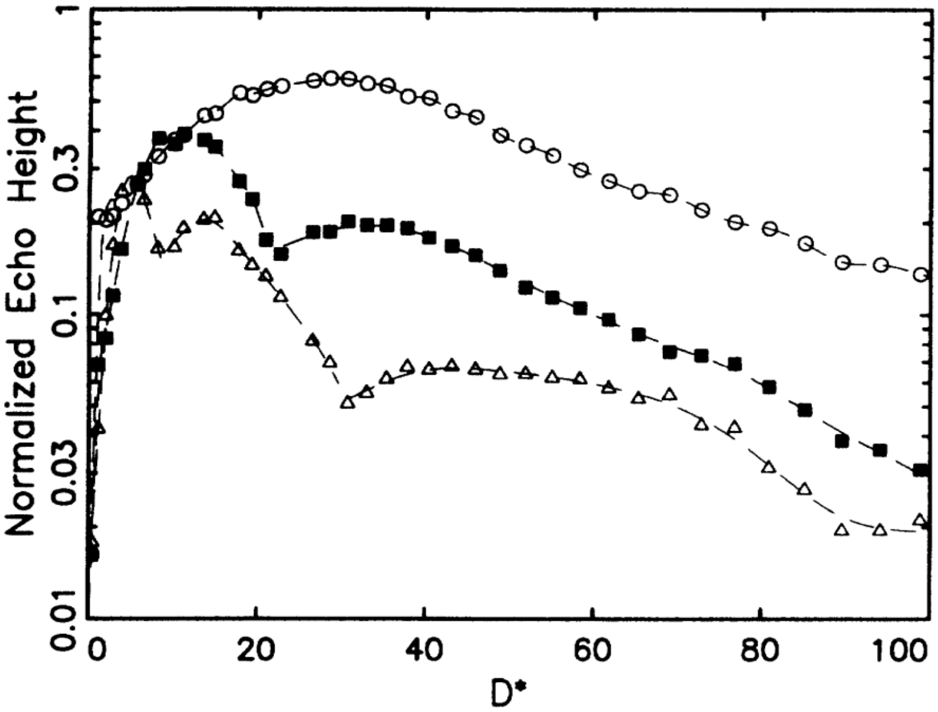

Figure 3.8: High-resolution scan of the echo height as a function of D^* at 5.1 mK in a field gradient of 4 G/cm. The normalized heights of the second, third, and fourth echoes are shown as follows: ◯ = E2, ■ = E3, and △ = E4. The dashed lines are intended only as guides to the eye.

polarization, and therefore μM, small. Otherwise, they found that, because of the spread in actual tip angle across the cell, M_z, following a 90° pulse was not uniformly zero throughout the sample. As a result, there were longitudinal spin currents, which caused the magnitude of the polarization $|\mathbf{M}|$ to no longer have the same value everywhere in the cell.

Unfortunately, the analytic treatment by Einzel et al. requires a uniform $|\mathbf{M}|$ so that the quantity $\mu^2(\mathbf{M} \cdot \overrightarrow{\nabla}\mathbf{M})\mathbf{M}$ in the Leggett equation [Eq. (3.18)] may be neglected. Without this simplification, the analysis of the echo heights becomes considerably more difficult. In their treatment, Bedford *et al.* developed a perturbative expansion for nonuniform $|\mathbf{M}|$, but it is limited to the case that the nonuniformities are small. In our own experiment, the sample cell is very large, and the H_1 field in the resonator during a typical rf pulse is 15.5 G, so that in a 4-G/cm gradient, $Gd/H_1 \simeq 0.2$. During a nominally 90° rf pulse, the spread in actual tip angle across the cell diameter is 2°. The spin currents driven by the resulting gradients in $\mathbf{M}$, may not only explain the gradient dependence of our data, but may also explain the relatively slow decay of the echo heights (as compared to the theory) for longer τ.

For the moment, however, we remain unable to extract the physical quantity of interest, $D_\perp$, from MSE data taken in a cell designed for a measurement of $D_\parallel$. Future experiments to search for the predicted diffusion anisotropy will have to be done in an apparatus where particular attention has been paid to the uniformity of the gradient and tip angle. Even such a careful approach may encounter difficulties when the molecular field is large, as has been pointed out by Candela.[54] If the cell is made small so as to keep Gd/H_1 small, then, following a large angle tipping pulse, the spin currents driven by the $\mu\mathbf{M} \times \overrightarrow{\nabla}\mathbf{M}$ term in the spin dynamics [obtained when Eq. (3.18) is substituted into Eq. (3.19)] will lead to the accumulation of M_z, against one wall of the cell, and cause additional nonuniformities. While small-amplitude probes such as the spin-wave experiments of Candela *et al.* is do not suffer from this difficulty, they are only sensitive to a linearized form of the spin dynamics. A well controlled and correctly analyzed multiple spin-echo experiment would not only reflect the full form of the spin dynamics, but would also be sensitive to the presence of any diffusion anisotropy in the system.

3.5 Long Time-scale Oscillations

3.5.1 Phenomenology

In our measurements of $D_{\|}$ we probed the purely longitudinal spin dynamics of the spin-polarized ^{3}He-^{4}He system. The behavior in this limit remains linear, and appears to be well described by theory. Our spin-echo experiments, on the other hand, primarily explored the nonlinear transverse spin dynamics. In this section we discuss our observation of a completely new, extremely long-lived excitation in this system. This excitation has a characteristic lifetime of about 10 sec - at least 2 orders of magnitude longer than that of weakly damped spin waves[15] - and appears to result from a situation in which a large-amplitude, but purely *longitudinal*, gradient in the magnetization becomes unstable against transverse perturbations. While the nature of these long-time scale oscillations are still not completely understood, we have developed a simple computer model that reproduces several key features of the observed behavior. Other aspects remain unexplained, however, and await further experimental and theoretical insight.

Figure 3.9 shows the digitized signal following a *single* π pulse applied to our 350-ppm sample at a temperature of 10.0 mK. The signal has been mixed down from 300 MHz to about 80 Hz. The pulse was applied at $t = 0$, and because

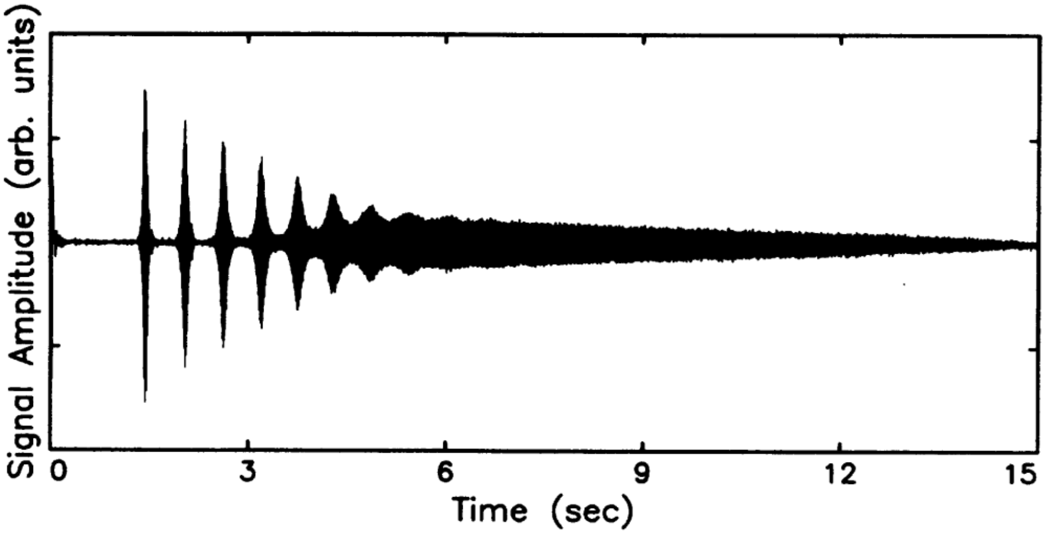

Figure 3.9: Digitized free induction decay (FID) following a single π pulse at a temperature of 10.0 mK.

the population inversion was not perfect (due to small inhomogeneities in the rf and static fields), there is a short free induction decay (FID) as the net transverse magnetization dies away. After a very long delay of about 1.4 sec, during which the digitizer records only noise from the spectrometer electronics, the first of a series of sharp "bursts" suddenly appears. These bursts are at first separated by intervals in which there is again no signal, but gradually shrink in amplitude, broaden, and finally merge into a very long "tail" which can persist for as long as 16 sec after the initial π pulse.

Since this signal was mixed down to about 80 Hz and digitized at 500 Hz, the individual cycles of the signal are indistinguishable on this time scale, but are visible in the expanded view shown in Fig. 3.10. The well-defined oscillations confirm that these signals really do arise from a coherently precessing transverse magnetization. It bears repeating that this bursting behavior is the response of the system to a *single* rf pulse, not some multiple pulse sequence, so that the signal

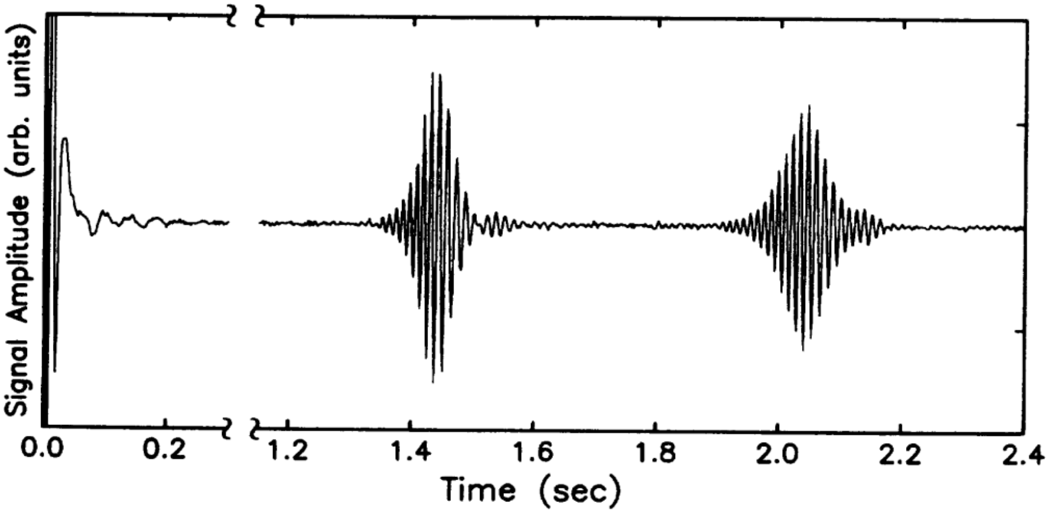

Figure 3.10: Expanded view of the initial FID and first two "bursts" in the long-time-scale signal shown in 3.9. Note that these sharp features are part of the response to a *single* rf pulse, and are therefore unrelated to the spin echoes we would observe following a sequence of two or more rf pulses.

cannot be associated with any kind of spin-echo response.

We took great pains to ascertain that these signals were not an artifact, and in particular, not the result of rf "feedthrough" from the large-amplitude π pulse into the receiver portion of our spectrometer electronics. Because of the long-time scales involved, we could connect our power amplifier directly to the cryostat co-ax, apply the π pulse with the receiver section completely disconnected from the apparatus, and still have time to switch the cables and observe the latter part of the signal - a procedure which rules out recovery effects in both the amplifiers and the ferrite components of the spectrometer. As an additional check, we replaced the entire receiver system with a crystal diode detector and audio amplifier, and fed the output directly to an analog chart recorder. We again observed the long-time-scale signal, which gave us further confidence that this behavior was not an electronic artifact.

3.5.1.1 Tip angle, gradient, and temperature dependence

Of course, much more convincing support for the reality of these signals is provided by their sensitivity to experimental parameters that have little or nothing to do with the spectrometer. We found that the behavior appeared only if the pulse used to invert the spins was within about 20° of π. The results of a scan over a range of tip angles is illustrated in Fig. 3.11. Significantly, if the NMR pulse length was extended until the spins were swept through 2π, we did not get a signal, but if we rotated the spins by 3π, the signal reappeared. From these results we conclude that the driving mechanism for these signals depends on a complete, or near-complete, population inversion in the lower chamber of the sample cell.

All of the data shown in Figs. 3.9 and 3.11 were obtained with our magnet's shim coils adjusted to give as narrow a NMR linewidth as possible. Under these conditions the line shape was not particularly Lorentzian, but rather had a very sharp central peak on top of a much broader background. If we added to this "minimum gradient" an additional, linear gradient, the change in the signal behavior was dramatic. Figure 3.12 shows the result of adding a gradient parallel to the 9.2-T static field, and perpendicular to the long axis of the lower chamber. An increased gradient delays the arrival of the first burst, increases the interval between successive bursts, and suppresses the long tail. If the gradient is increased much beyond what is shown in the figure, the entire behavior disappears. If the gradient is instead applied perpendicular to H_0 and parallel to the long axis of the lower chamber, the behavior remains qualitatively the same. In both cases, if the field gradient across the cell is more than about 0.25 G/cm ($\Delta H \approx 3 \times 10^{-6}$ of H_0), the long-time-scale oscillations are completely suppressed, a fact which we used in our measurements of $D_{\parallel}$.

The signal traces in Fig. 3.12 also illustrate an additional, larger-amplitude

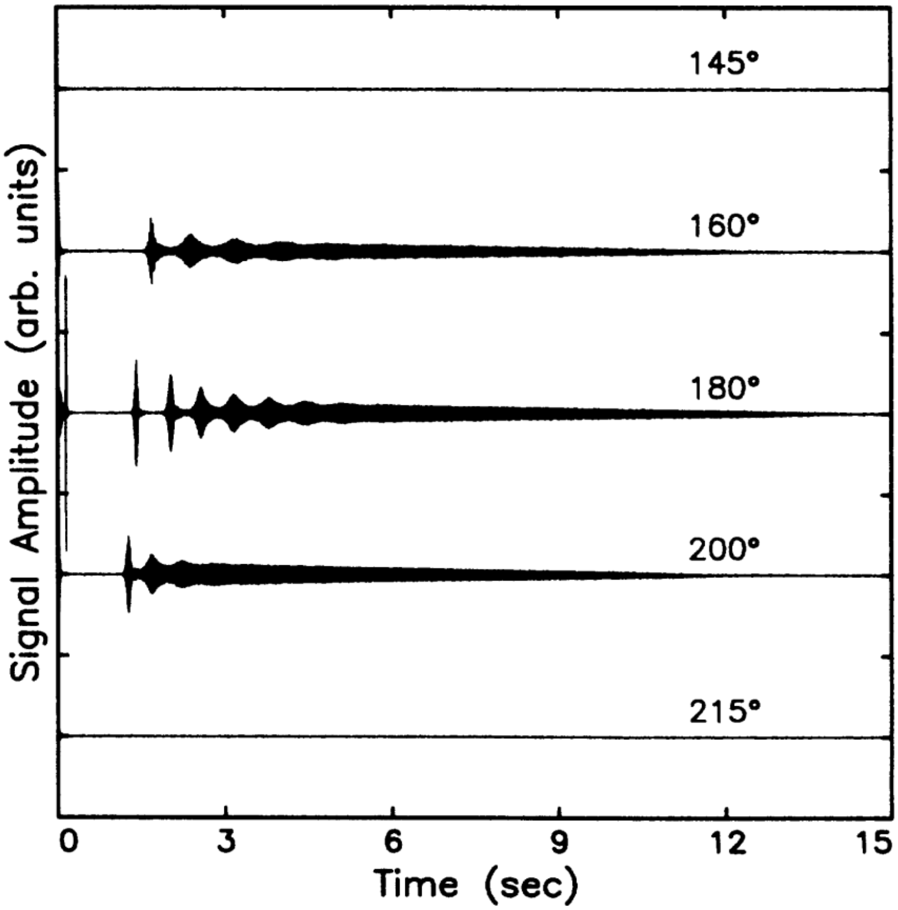

Figure 3.11: Tip angle dependence of the long-time-scale oscillations at 10 mK. All of the data are drawn on the same scale. The data were taken with the magnet shim coils adjusted to give a “minimum gradient” (see text). Note the early burst (see text) that appears only for a tip angle of 180°.

burst at approximately 150 msec after the π pulse. We only observed this early burst at certain temperatures, and for particular configurations of the shim coils. In the case shown, this signal does not seem particularly sensitive to the additional linear gradient, although it is eventually suppressed at gradients $\gtrsim 0.4$ G/cm. Note that one of these early bursts appears in Fig. 3.11, but only for a 180° tip angle. When we applied the gradient perpendicular to H_0, we did not observe this early burst at all. It is not yet clear how this early burst is related to the long-time-scale part of the signal. For the moment, it remains among the least understood aspects of the experiment.

The temperature dependence of these signals is quite dramatic, as is illustrated in Fig. 3.13. As the temperature is raised, the bursts become less pronounced and the overall time scale is reduced. For temperatures $\gtrsim 35$ mK, we do not observe these signals at all. The fact that they persist well above the Fermi temperature of this 350-ppm solution ($T_F \simeq 13$ mK) suggests that the behavior is not driven by degeneracy effects. Note also that the strongest signals do not occur at the lowest temperature, but occur instead in the vicinity of 10 mK, where $D_\parallel$ is at a minimum.

3.5.1.2 Size of the effect

Although these novel signals last for an extremely long time, their instantaneous amplitude is not very large. Comparison with the initial amplitude of the free induction decay following a 90° pulse shows that these signals are on the order of $\frac{1}{300}$ times as large. Because the signal from the NMR resonator represents a spatial average of the transverse magnetization over the whole lower chamber of the sample cell, we cannot tell from this comparison whether we are seeing a very small-amplitude disturbance across the whole cell, or one that has a large amplitude but is highly localized.

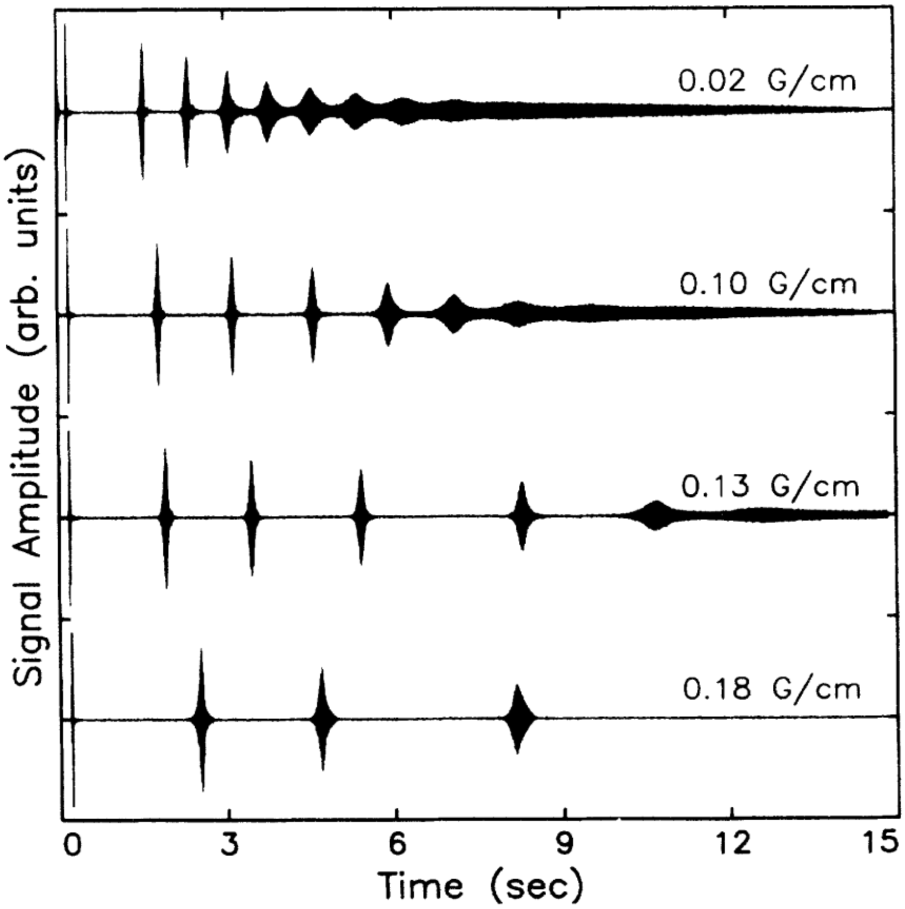

Figure 3.12: Dependence of the long-time-scale oscillations on a magnetic-field gradient applied parallel to H_0, and perpendicular to the long axis of the sample cell. The temperature is 9.9 mK. Note that the spacing between successive bursts is not even. The early bursts (see text) are clearly visible at $t \simeq 150$ msec, and appear to have a uniform amplitude because they have all been clipped by the digitizer.

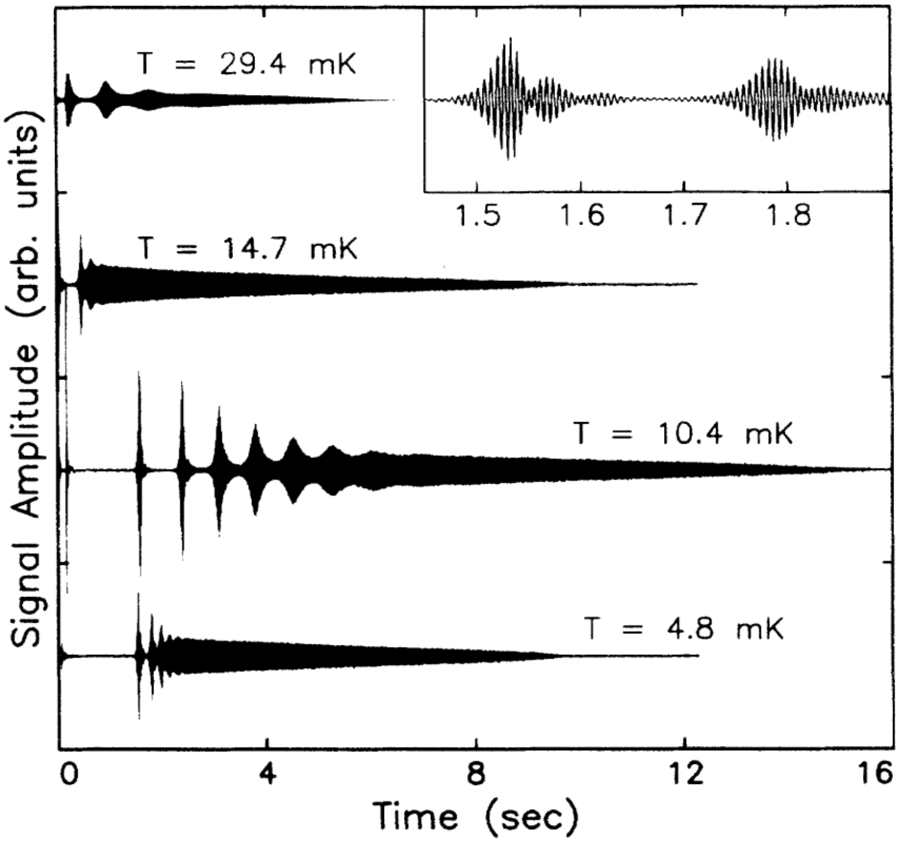

Figure 3.13: Temperature dependence of the long-time-scale oscillations. All the data are drawn on the same vertical scale, and were taken using the “minimum gradient” configuration of the magnet shim coils (see text). The inset shows the part of the 4.8-mK trace between 1.5 and 1.9 sec on an expanded time scale.

In either case, and in spite of the small instantaneous amplitude of the signals, the driving mechanism behind these oscillations eventually involves a substantial fraction of the spins in the lower chamber of the sample cell. We ascertained that this was the case by using a series of small-angle probe pulses - exactly as in our diffusion measurements - to determine M_z in the lower chamber immediately after the oscillation had died out. We compared these results with similar measurements in which an applied magnetic field gradient $\partial H_0/\partial z$ was used to partially or completely suppress the long-time-scale signal. We found that after the oscillation had died out, the polarization in the lower cell was still largely inverted, but that the inversion was *smaller*, by as much as 25%, than it would have been in the absence of one of these signals. As can be seen from Fig. 3.14, the amount of z magnetization lost depends approximately linearly on the duration of the oscillation (or, to an equally good approximation, on the total rf power radiated during the signal). The important implication of this result is that these long-time-scale oscillations proceed by converting z component of magnetization into transverse components at a fairly steady rate, rather than by somehow preserving some initial transverse component created at the start of the oscillation. The fact that the amplitude of the signals remains small (instead of building as the oscillation progresses) implies that these transverse magnetization components are dissipated or otherwise destroyed as fast as they are created.

3.5.1.3 Additional features

While the sensitivity of these long-time-scale oscillations to such external parameters as field gradient and temperature is quite dramatic, there are some more subtle features of the data that are also worthy of note. One such feature can be seen in Fig. 3.10. There is a plainly visible frequency shift (100 Hz) between the FID at early times, and the nonlinear oscillation at later times. This shift may

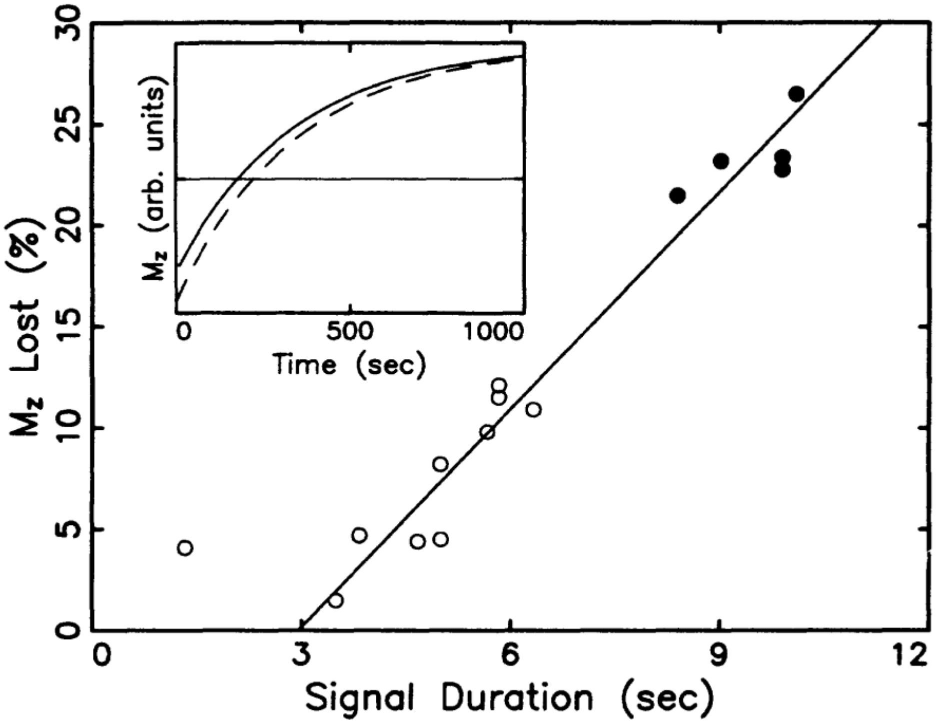

Figure 3.14: Fraction of z component magnetization lost during a long-time-scale oscillation as a function of the duration of the signal. The data were obtained at 21 mK (●) and 29 mK (○). The amount of lost magnetization is determined by comparing the recovery of M_z, following the oscillation to the recovery observed when there is no long-time-scale signal, and is expressed as a percent of M_z, immediately following the π pulse. Inset: a comparison of the "no signal" behavior (dashed line) with the exponential recovery following a 10-sec oscillation (solid line). Both curves were obtained at 21 mK.

be analogous to the frequency shifts observed in spin-wave experiments where the local molecular field causes the magnetization to precess at a frequency that is slightly different from the Larmor frequency. On the other hand, it could simply indicate that the signal is generated in a relatively small region where the local Larmor frequency is somewhat different from the average over the whole cell. As we shall argue somewhat later, we believe that the second explanation is more likely.

In addition to this frequency shift, we find that the signals are also "chirped." That is to say, the frequency of the oscillations is not constant in time, but shifts slightly over the length of the signal. This chirping is difficult to observe when the mixed down frequency of the signals is on the order of 100 Hz, but is clearly visible in signals which have been mixed to a much lower frequency.

We found that in order for the overall behavior of these signals to be reproducible, we had to wait until the sample had relaxed completely ($t \gtrsim 10\tau_0$) before applying successive z pulses, as is illustrated in Fig. 3.15. If we did not wait long enough, the signals appeared quite similar to those we observed when we applied a field gradient: the long tail of the signals was suppressed, and the time interval between successive bursts was extended. If we did allow sufficient relaxation, the overall behavior was largely reproducible, although there remained some trace-to-trace "jitter" in the exact arrival time of the bursts. This jitter likely indicates that there is some stochastic element to the driving mechanism behind these oscillations.

It is interesting to note that applying a second π pulse immediately after the signal died out did not shorten the time interval required for reproducibility. This second pulse returns M_z, to nearly its equilibrium value, but cannot remove any residual transverse polarization created during the course of the oscillation. It seems, therefore, as if those residual components, although completely "scrambled" by inhomogeneities in the magnetic field, still have an important influence on the system, and that reproducible behavior is obtained only once all "memory" of the transverse magnetization has decayed away. In this liquid system, we expect that to occur on a time scale $T_2 \sim T_1$. If this argument is correct, it may also provide an explanation for the magnetic-field-gradient dependence. In that case, the transverse components of $\mathbf{M}$ would be created by the spread in effective tip angle (due to the gradient), rather than a previous long-time-scale signal.

3.5.2 Radiative mechanisms

One of the first mechanisms we considered in searching for an explanation for these phenomena was some kind of maser oscillation or other stimulated emission effect. The characteristic time constant for such processes, however, is given by[20] $\tau_R = (2\pi\eta Q\gamma\mathcal{M}_0)^{-1}$, where η and Q are the cavity filling and quality factors, respectively, γ is the ^{3}He gyromagnetic ratio, and $\mathcal{M}_0 \simeq n_3\mu_3 M_0$ the equilibrium magnetization of the spin system (n_3 and μ_3 are the ^{3}He density and nuclear magnetic moment, respectively). For our 350-ppm sample at 10 mK, this time constant is about 0.1 msec. If some kind of maser action were responsible for the long-time-scale oscillations, we would not only expect the process to start immediately after the π pulse when the cavity rf field is at its largest, but we would also expect it to exhaust the energy in the inverted spin system on a time scale given by τ_R. This is inconsistent with the long delay before these signals appear, with the overall time scale for the signals, and with our observation that there is still a substantial population inversion after the oscillation has died out.[†]

[†] A masing mechanism has been invoked as an explanation for the msec time-scale bursting behavior previously observed in pure ^{3}He (Ref. 55). That mechanism (Ref. 56) applied to our system, however, predicts an interval between bursts of only a few μsec, and a similar time scale for the overall lifetime of the signals.

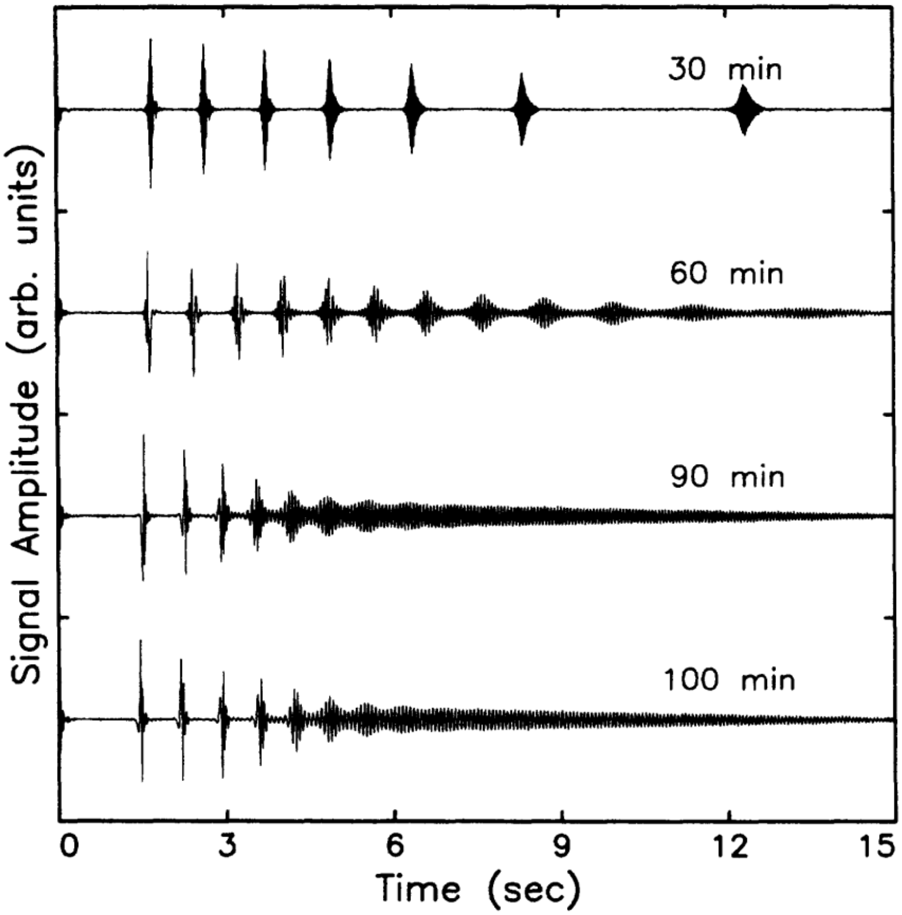

Figure 3.15: Long-time-scale oscillations following π pulses separated by varying time intervals. Each trace is labeled by the approximate elapsed time since the previous pulse. Note that the upper two traces appear quite different from each other and from the lower two traces, but are very similar to the behavior seen when a field gradient is applied, as in Fig. 3.12. The lower two traces are nearly identical, and represent the response of the fully relaxed system. The apparent frequency of the signals varies because the ~75 Hz/h decay of the magnetic field has not been exactly compensated.

A related mechanism we have also considered is not stimulated, but spontaneous emission. In this model, one imagines that any initial maser oscillation is somehow suppressed, but that after some delay, spontaneous emission causes the generation of an initial cavity field, which in turn causes stimulated emission and masing. Purcel[57] has shown that the spontaneous emission rate for a nuclear magnetic moment in a resonant cavity should be enhanced over the free-space rate by a factor that depends on the cavity volume V_C, and quality factor Q. In our cavity ($Q \simeq 1500$, $V_C \simeq 2$ cm^3), however, this enhancement factor is relatively modest, so the excited state lifetime is still on the order of 10^8 sec - much longer then either the initial delay or the subsequent signal observed in our system. As a result we do not consider either spontaneous emission or maser action to be plausible mechanisms for the generation of these Long-time-scale oscillations.

3.5.3 A simple model

An important clue to the model that we have developed, and which does explain several aspects of the observed signals, is provided by an examination of the temperature dependence illustrated in Fig. 3.13. As we pointed out earlier, the oscillations persist to well above T_F, and so are not likely a degeneracy effect. A more plausible mechanism is provided by the nonlinear terms in the spin-dynamical equations, whose strength is given by the parameter μM. An s-wave limit calculation of this parameter, which should be sufficiently accurate in this regime,[44] predicts that μM should remain significant (i.e., ≥ 1) up to temperatures on the order of 40 mK. On the other hand, this same calculation predicts that μM should diverge roughly as $1/T$, so that any nonlinear behavior should become stronger as the temperature is lowered. As can be seen in Fig. 3.13, however, that is not what happens. Instead, the signals with longest time scales and largest amplitudes are observed at intermediate temperatures in the vicinity of 10 mK. If the temperature is either raised or lowered from this point, the signals become shorter and the bursts become less pronounced (although at lower temperatures the initial delay does not shorten up). There is a quantity, however, that does mimic the non-monotonic temperature dependence of these signals: the spin-diffusion coefficient. As can be seen from Fig. 3.5(a), the longest-time-scale oscillations occur near the minimum in $D_{\|}$, and shorter-time-scale signals appear to correspond to faster diffusion. For this reason, we believe that both the diffusion of M_z.through the small channel between the two chambers in our sample cell, and the nonlinearities proportional to μM, play important roles in driving these signals. If the observed behavior does indeed arise from some combination of spin diffusion and the inherently nonlinear spin dynamics in the system, then there must be some additional mechanism at work. After the π pulse, all of the polarization gradients are purely longitudinal, so the spin dynamics should remain entirely linear. In fact, all of our measurements of longitudinal spin diffusion were predicated on the fact that the spin configuration generated by the π pulse would not couple to the transverse nonlinear modes of the system. In order to invoke these nonlinearities as an explanation for the long-time-scale oscillations, we need a mechanism that will, under the right circumstances, generate transverse magnetization from initial conditions in which both $\mathbf{M}$ and gradients in $\mathbf{M}$ are purely longitudinal. A mechanism that will provide precisely this coupling was actually pointed out some time ago by Castaing.[58] In an effort to explain some results from an experiment on rapidly melted spin-polarized ^{3}He, Castaing showed, via a simple linear stability analysis, that the Leggett equation has a regime in which small transverse perturbations will grow exponentially, instead of being damped. To illustrate how this mechanism may apply to our own experiment, we outline the relevant parts of his treatment below. In the absence of a magnetic-field gradient, the spin dynamics of the system are given by Leggett's equation for the spin currents, Eq. (3.17), and the continuity equation, Eq. (3.19), with $\delta\mathbf{H}$ set equal to zero. (Since we believe diffusion anisotropy to be unimportant at currently accessible temperatures, we shall consider the case that $D_{\|} = D_{\perp} = D_S$) We can examine the response of the system to small-amplitude perturbations by inserting into Eqs. (3.17) and (3.19) trial solutions which consist of the steady-state polarization and spin current plus a small oscillatory term:

$$\mathbf{M} = \mathbf{M}_0 + \mathbf{m}e^{i(\omega t - kx_1)}, \tag{3.17}$$

$$\vec{\mathbf{J}} = \vec{\mathbf{J}}_0 + \vec{\mathbf{j}}_1 e^{i(\omega t - kx_1)}. \tag{3.18}$$

Ordinarily, when such a procedure is carried out to obtain the dispersion relation for free (plane-wave) spin oscillations, the quantity $\vec{\mathbf{J}}_\mathbf{0}$ is taken to be zero. That is to say, in the steady state, there are no spin currents. Following Castaing, however, we shall assume that there is, in fact, a large-amplitude steady-state spin current imposed on the system. By "steady state," we mean only that this spin current is slowly varying on the time scales Ω_{int}^{-1} and ω^{-1} given by the molecular field precession and spin-wave frequencies, respectively, and on the length scale k^{-1} given by the spin-wave wavelength. What we have in mind as the origin of this spin current is, of course, the transport of magnetization through the channel that connects the two halves of our sample cell. It is driven by the "steady-state" gradient in the spin configuration following the π pulse, so we take this spin current to be carrying z component of magnetization, and to be defined by the relation

$$J_0^z = -D_s \overrightarrow{\nabla} M_0, \tag{3.19}$$

where M_0 is understood to be parallel to the z axis in spin space.

If we substitute the trial solutions including J_o^z into Eqs. (3.17) and (3.19), and keep only terms up to first order in the small quantities $\mathbf{m}$ and $\vec{\mathbf{j}}_\mathbf{1}$, it is a straightforward matter to find separate dispersion relations for the transverse and longitudinal components of the magnetization. For **m**, we find

$$\omega_z = ik^2 D_s, \tag{3.20}$$

which describes ordinary spin diffusion. In other words, longitudinal perturbations remain purely damped, and their behavior is not affected by the addition of the large spin current. The result for $m_\pm = m_x \pm i m_y$,however, is somewhat different:

$$\omega_\pm = \frac{-k^2 D_s}{(i \pm \mu M_0)} \left\{ 1 \pm \frac{\mu}{k} \overrightarrow{\nabla} M_0 \right\}, \tag{3.21}$$

where we have used Eq. (3.19) to substitute for J_0^z. Aside from the factor in braces, Eq. (3.21) is just the dispersion relation for plane-wave spin oscillations.[59]

The importance of this additional factor, however, can be seen by considering what happens to Eq. (3.21) in the limit that gradients in M_0 are large enough that

$$\left| \frac{\mu}{k} \overrightarrow{\nabla} M_0 \right| > 1. \tag{3.22}$$

In this case, the entire dispersion relation would change sign. In particular, the imaginary part of Eq. (3.21) would change sign, so that the amplitude of small transverse perturbations would grow exponentially instead of being damped.

This analysis forms the basis of our simple model for the long-time-scale oscillations. It shows that even from an initial condition in which $\mathbf{M}$ and $\overrightarrow{\nabla}\mathbf{M}$ are purely longitudinal, it is possible for large gradients in the polarization to bring the spin dynamics into a regime where they are unstable against the growth of transverse components. Of course, in order for this to be a plausible model, the region of instability must correspond to the conditions of our experiment. We can approximate the gradient set up by the π pulse as $\overrightarrow{\nabla}\mathbf{M} \approx 2M/L$, where $L = 0.36$ cm is the length of the channel. If we estimate μM from Ref. 18 to be 10 at 10 mK, and assume that k is determined by the characteristic dimensions of the lower chamber

($\sim$ 1 cm), then at 10 mK we find

$$\frac{2\mu M}{kL} \simeq 9 \gg 1, \tag{3.23}$$

so we are well within the unstable region. Given the same k and L, we find that there is a critical value of μM below which the instability will not occur, so that we should not expect to see the signals above approximately 30 mK, in reasonable agreement with what we observe in the experiment.

3.5.4 Computer simulations

The difficulty with the sort of linear stability analysis we have just carried out, however, is that, while it can show us that there is a region of instability, it can tell us nothing about the behavior inside the unstable region. We derived Eq. (3.21) in the limit of small perturbations, and what we learned is that the perturbations will not stay small. To investigate the behavior above the critical value of μM, we need to keep the full nonlinear equations for the spin dynamics. Because of the complicated form of these equations, we decided that the best approach was to model the system on a computer, and numerically integrate the time evolution of its spin dynamics.

3.5.4.1 Implementation

Because we hoped to recover the essential behavior of the system with as simple a model as possible, we chose to limit our simulation to one spatial dimension, and to work with a relatively small lattice of 128 points. While there are many algorithms for the numerical integration of diffusive equations that are designed to be both stable and fast, we found that adapting them to the more complicated Leggett equation did not seem promising. Instead, we decided to use a simple two-step explicit integration scheme in which we first calculated the spin currents, and then used the continuity equation to advance the system in time. In order to mimic the flow of magnetization into and out of the lower chamber of our cell, we considered one end of the lattice to be connected to an infinite source of $M_z = +1$ and an infinite sink of $M_+ = 0$ At the other, "closed" end of the lattice, the boundary conditions were chosen so that there were no spin currents into or out of the wall. The entire simulation was carried out in the rotating frame, so that our simulated signals were automatically "mixed down" from 300 MHz. For initial conditions, we tried to mimic the effect of an imperfect π pulse for $t \gg T_2^*$ by choosing M_+ to have a small uniform magnitude (typically, $|M_+| = 0.005$), but a random orientation, and by assigning $M_z = 1$ at every lattice site. The simulation was then simply allowed to propagate forward in time, and simulated signals were generated by periodically recording the average of M_x across the cell. Alternatively, the program could be made to record "snapshots" of the whole cell as a function of time.[30]

In any numerical integration scheme, it is important to make sure that the calculation remains stable. In the present case, extra precautions were required because the system has an intrinsic instability, and we needed to ensure that any interesting behavior was associated with the true spin dynamics and not with a spurious numerical effect. In practice, we found it very easy to distinguish the two: in the latter case, the program would quickly start producing values of the polarization greater than 1. As a general rule, we encountered no difficulties if we stayed well within the stability criterion used in integrating ordinary diffusion equations.[60] As an additional check, we verified that the program gave identical results with the time step reduced by half.

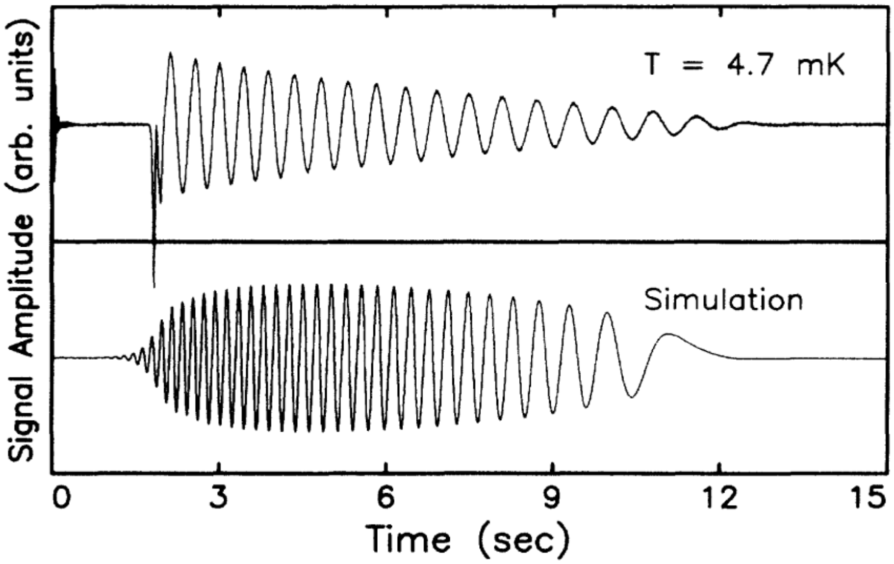

Figure 3.16: Comparison of an experimental signal taken at 4.7 mK and a simulation. Note the monotonic frequency shift in both traces.

3.5.4.2 Results

Figure 3.16 shows a comparison of a simulated signal with an experimental signal taken at 5 mK and mixed to a very low frequency. The parameters used in the simulation correspond approximately to the experimental conditions. The model sample cell was taken to be 1 cm long, and the channel length was chosen to be 0.2 cm, to match the ratio 2 cm to 0.4 cm found in the actual cell. The diffusion coefficient was set equal to 0.05 cm^2/sec, the amplitude of the initial, randomly oriented, transverse polarization was 0.005, and the equilibrium polarization was taken to be +1. There was a linear gradient of 0.05 in units of $10^{-6} \times 9.2$ T/cm (0.045 G/cm) applied across the cell, and the point of zero frequency (in the rotating frame) was placed in the center of the cell. The spin rotation parameter μ was set equal to 7.0 so that μM would *roughly* correspond to the experimental value, at least as predicted by the s-wave limit calculation of Ref. 18.

In spite of the relative simplicity of our model, the simulations reproduce two of the most striking aspects of the experimental data: the initial delay after the π pulse, and the very long-time-scale signal that follows. The numerical signal even has a monotonic frequency shift similar to what is observed in the experiment. On the other hand, it does not exhibit any of the dramatic bursting behavior that is usually characteristic of the experimental signals.

While the comparison made in Fig. 3.16 looks quite reasonable, we cannot argue that our model does in fact describe the experiment unless we first verify that the numerical signals respond to such external parameters as magnetic-field gradient and temperature in a manner at least qualitatively similar to the actual long-time-scale oscillations, and that whatever triggers the oscillations in the simulation does in fact correspond to the Castaing instability on which our model was based. Only if the simulation seems to provide a plausible description of the experimental behavior can we use it to provide some insight into the internal dynamics of the system.

In order to test whether the numerical model does indeed respond in a manner similar to the experiment, we examined the simulated signals given by a broad range of input parameters. We found that as we increased the linear magnetic-field gradient, the simulated signals became smaller and shorter, and were eventually eliminated by a gradient of 0.05 G/cm. This gradient is only a factor of 2 to 4 smaller than the gradient required to eliminate the experimental signals, which we do not find unreasonable. On the other hand, increasing the gradient in the simulation leads to a shorter initial delay, in contrast to the experiment where increasing the gradient lengthened the initial delay.

Changing the "temperature" in the simulation is not quite as straightforward. In the actual experiment, both the strength of the molecular field and the speed with which the spins diffuse change with temperature. We found that since the sensitivity of the simulation to changes in these parameters does not exactly match the experiment, we could reach a better understanding of the behavior by varying D_s, and μM separately. In the experiment, we found that increasing the diffusion coefficient (by moving the temperature away from the minimum in $D_\parallel$ at 10 mK) reduced the overall time scale of the signals, and (for temperatures above 10 mK) reduced the length of the initial delay. In the simulation we find a roughly similar behavior: speeding up the spin diffusion shortens both the initial delay and overall time scale of the signals.

Increasing the temperature in the experiment also results in a reduction in the strength of the molecular field μM, and a corresponding weakening of the long-time-scale oscillations. In our simulations, we find that the signals are very sensitive to the value of μM, and that the correspondence to the experiment is somewhat rough. In the experiment, the signals disappear at a temperature where we estimate μM to be $\lesssim 2$. In the simulation, they disappear when $\mu M \lesssim 5$. If we increase μM, we find that a value of 7 gives a signal that is most like what is observed in the experiment. This value is about a factor of 2 smaller than the $\mu M \simeq 17$ at 5 mK we estimate from Ref. 18.

To verify that the growth of the simulated signals is in fact driven by the Castaing instability, we examined "snapshots" of the magnetization profile in the model cell at successive times. From the form of the critical parameter [Eq. (3.22)], it is apparent that the instability will be driven, at least initially, by long-wavelength (small-k) perturbations. Thus, we see that in order to drive the instability, the gradients in $\mathbf{M}$ must be large (to make the critical parameter large) *and* must extend over long distances (to couple to long-wavelength perturbations).

As a rough measure of this critical parameter, we constructed the quantity

$$\frac{\mu}{2\pi}\Gamma\frac{dM_z}{dx}\bigg|_{x=0} \tag{3.24}$$

from the initial slope of M_z, at the open end of the cell, and the distance Γ over which it fell halfway toward the value $M_z = 1$ far from the open end. We found that, although the initial slope was steadily decreasing with time, our "critical quantity" steadily increased, and had reached a magnitude of about 0.7 at $t = 1$ sec, where the signal first started to rise. Given the somewhat arbitrary definition of this quantity, we find the agreement with Eq. (3.22) to be reasonable.

Finally, if the behavior in the simulation really is governed by an instability in the spin dynamics, then we would expect the results to be only weakly dependent on the perturbation that seeds the initial growth. In our simulation, that perturbation is provided by the randomly oriented transverse component of M which we assigned to each lattice site at $t = 0$. We found that neither using a different random orientation nor reducing the amplitude of the initial M_+ by a factor of 10 had a significant effect on the simulations. In both cases, the amplitude, initial delay, and overall time scale of the signals remained quite close to those illustrated in Fig. 3.16.

3.5.4.3 Analysis

Since the general behavior of our simulation in response to such parameters as the magnetic-field gradient and temperature approximately follows that of the experimental signals, it seems reasonable to believe that a more detailed examination of the internal dynamics of our model system will give us some insight into the actual long-time-scale oscillations themselves.

Figure 3.17 shows a "snapshot" of the magnetization along the length of the cell at $t = 4$ sec for the simulation illustrated in Fig. 3.16. The dotted line shows the profile that M_z, mould have if there were no nonlinearities in the system ($\mu = 0$). The solid line shows the actual profile of M_z which exhibits a region with an extremely steep gradient. Note that the value of M_z at the open (left-hand) end of the cell is *higher* than it would be in the absence of the nonlinear terms, and therefore slows down the rate at which spin-up polarization can enter the cell. Also shown in the figure (dashed line) is the magnitude of the transverse polarization, which is zero everywhere in the cell except in the region of steep gradient in M_z. Both M_z, and $|M_+|$ are plotted on the same scale, so it is evident that the transverse component is large.

Even more intriguing is the vector sum of the two quantities, also illustrated in Fig. 3.17. It shows that the magnetization develops a sharp, coherent 180° twist that forms a domain-wall-like boundary between the spin-up and spin-down regions of the sample cell. The signal in the simulation comes entirely from the transverse component of $\mathbf{M}$ in the region of the twist, which perhaps answers one of our questions about the experimental behavior. In the simulation, at least, the signal arises from a large-amplitude disturbance in a small region of the cell, rather than from some small disturbance over the whole cell.

Further insight into the behavior of the simulation can be gained by considering the time development of the magnetization across the whole cell. Figure 3.18 shows the profile of M_z, at 1-sec intervals (for the same set of parameters as in Fig. 3.17). At early times, before the growth of the instability, the polarization, as a function of distance along the cell, just smoothly decays from its value at the open end. At some point, however, it starts to develop a small kink. The kink then appears to act back on itself (through the transverse components of $\mathbf{M}$) and to continue to steepen until it reaches some limiting slope. As the simulation progresses, however, ordinary spin diffusion continues to drive spin-up polarization into the cell, so that

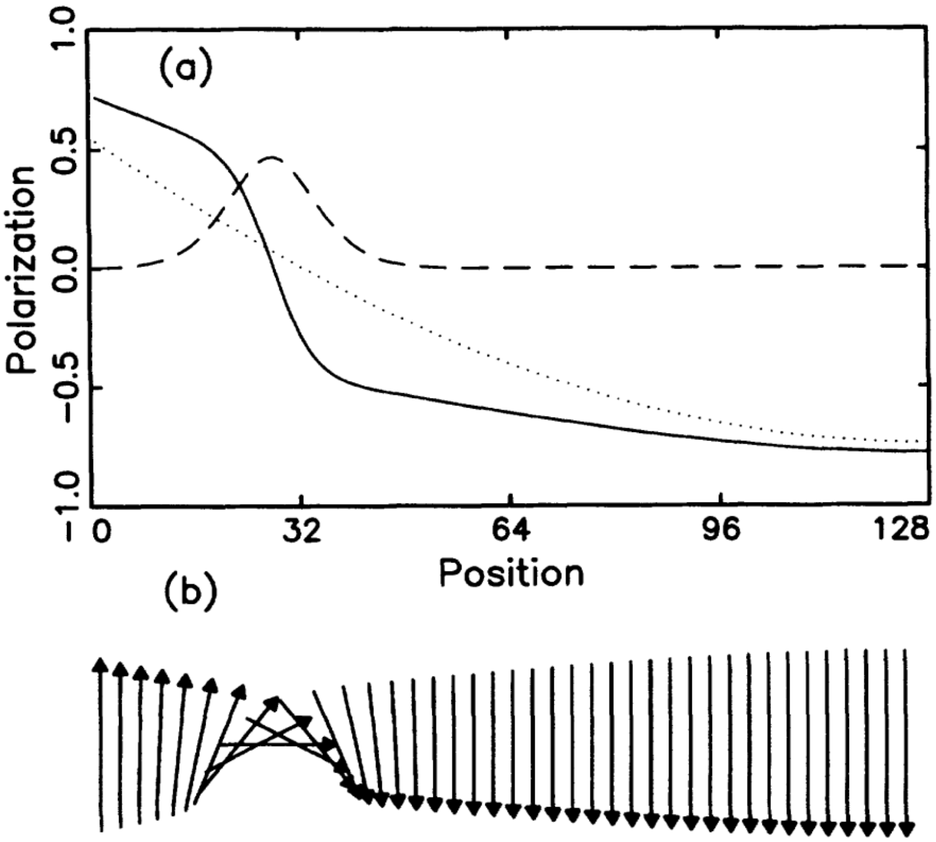

Figure 3.17: (a) A "snapshot" of the polarization inside the $t = 4$ sec for the simulation illustrated in Fig. 3.16. The open end of the 1-cm-long cell is at lattice position 0, and the closed end is at lattice position 128. The dotted line gives M_z, for the case that $\mu = 0$, while the solid line gives M_z for the case that $\mu = 7$. The dashed line shows M_+ (for $\mu = 7$) and is plotted on the same scale as the other curves. (b) A vector plot of the total polarization across the cell showing a coherent "twist" in $\mathbf{M}$.

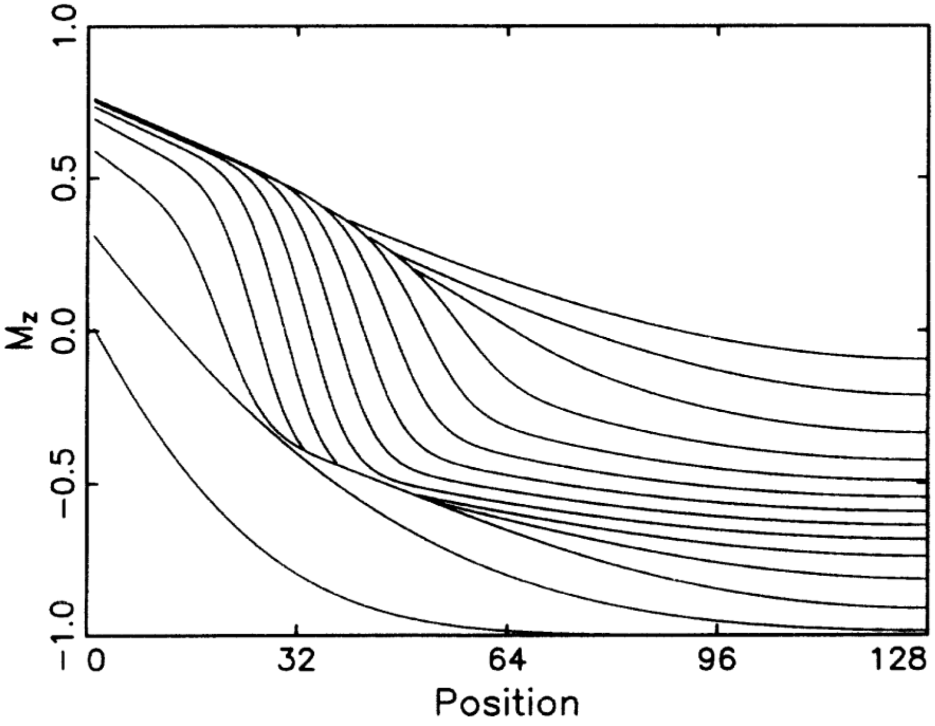

Figure 3.18: A time series showing the profile of M_z across the cell at 1 sec intervals. The data correspond to the simulation shown in Fig. 3.17.

the value of M_z on the "downstream" side of the kink continues to rise. Eventually the polarizations on either side of the steep region become too close in value, the gradient is forced below the critical point, and the kink dies out.

Figure 3.19 shows a matching time series, but at half-second intervals, for the magnitude of M_+. At early times, there is no net transverse magnetization in the cell, but as the kink in M_z (which actually corresponds to a twist in the vector $\mathbf{M}$) develops, M_+ starts to build up. The twist then moves down the sample cell and eventually dissipates, which may provide us with another clue to the behavior observed in the experimental signals. In the simulations, at least, the frequency shift of "chirping" arises from the change in the local Larmor frequency (due to the applied magnetic field gradient) as the "domain wall" structure moves down the cell. The fact that the signal dies out just as it reaches the point of zero frequency (see Fig. 3.16) is coincidental. Moving that point both closer to and farther from the open end of the cell had no effect on the envelope of the signal.

The behavior illustrated so far raise several additional questions, including to what degree the duration of the signals depends on the size of the cell. As can be seen from Fig. 3.18, the signal dies out when there is not enough "headroom" between the values of M_z on the upstream and downstream sides of the domain wall, so that we might expect a bigger cell to result in a longer signal (since there would be more room for the polarization on the downstream side to spread away from the kink). in a (simulated) 5-cm cell, the signal is indeed longer, but not enormously so (15 sec instead of 12 sec). In fact, examination of the magnetization profile in that case revealed that when the signal died out, the domain wall had only traveled about 0.5 cm into the cell. Most of the magnetization in the cell was undisturbed, so that the closed end of the cell had no effect on the duration of the signal. The behavior of M_z in the vicinity of the kink, however, looked almost identical to the behavior illustrated in Fig. 3.18. In other words, even without a wall to confine the polarization, M_z on the downstream side of the kink still rises up and pinches off the signal.

It appears from the long cell results that the duration of the signal is controlled by the relative strength of the reactive term in the spin dynamics, which form the kink and cause it to sharpen up, and the dissipative terms, which work to spread the kink out. By increasing μ, we could increase the importance of the reactive terms, in which case the kink became steeper and persisted for a much longer time. It is also interesting to note that with an increased μ, the kink traveled down the cell much more slowly. The reason for this reduced motion is found in Fig. 3.17 where we pointed out that the appearance of the domain wall *raised* the value of

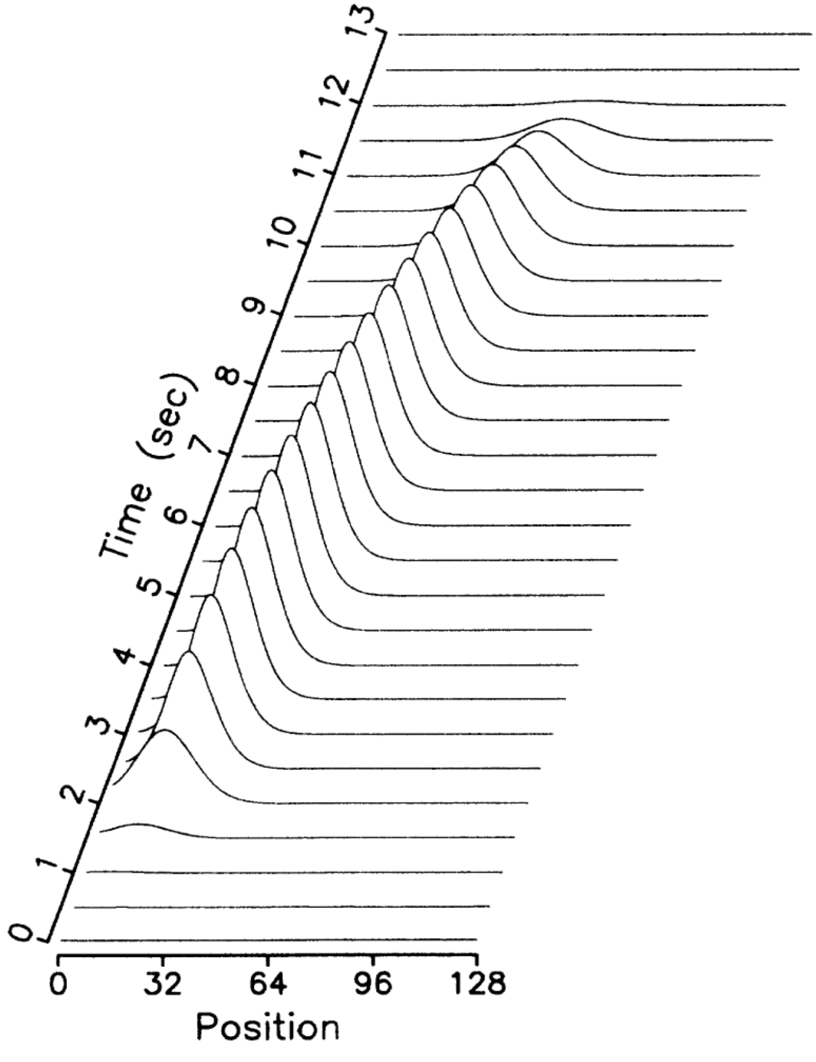

Figure 3.19: A time series showing the profile of $|M_+|$ across the cell at 1 sec intervals. The data correspond to the simulation shown in Fig. 3.17.

M_z at the open end of the cell. Our simulations show that an increased μ is even more effective at this, further slowing the rate at which polarization can enter the cell and push the domain wall downstream.

Given the limitations of our model, the best description of our results so far is that they are suggestive. We find it likely that the actual long-time-scale oscillations observed in the experiment are driven by a nonlinear instability in the Leggett equation, but there remain several issue. The question of what drives the "bursting" behavior is among the most interesting of these.

Also of interest is the relation, if any, between the behavior revealed in our simulation and the previously investigated spin dynamics in this system. In particular, Lévy[61] has shown that in the limit of very low dissipation (i.e., for μM sufficiently large) the Leggett equation can be decoupled into separate equations for the magnitude of the magnetization, M, and its direction, $\hat{\ell}$. The former just obeys the ordinary diffusion equation, but $\hat{\ell}$ obeys the Heisenberg ferromagnet equation, which has known spin-wave, soliton, and soliton wave train solutions.[62] Lévy showed that in the next approximation, the equation for $\hat{\ell}$ includes an additional dissipative term. In this case, he found that the spin dynamics include not only spin waves and solitons but also more complicated three-phase modes termed "pulsons." All of these behaviors, however, were found in a regime where the system had been stabilized against transverse perturbations by the application of a linear magnetic-field gradient. In our experiment, the long-time-scale signals are *suppressed* by a field gradient, and in our model, it is just such a transverse instability that drives the entire behavior. It seems at least plausible that the behavior we observe is precisely the sort of instability that Lévy wished to avoid in his analytic treatment of the spin dynamics.

Finally, we note that although we searched for these long-time-scale signals in our more concentrated (1940 ppm) mixture, we were unable to observe them. It appears that the combination of reduced polarization and (slightly) slower diffusion prevents the system from exceeding the instability criterion. If we put the appropriate parameters into our simulation, we find that there is an instability, but it only sets in after about 10 sec. We find it extremely unlikely that in the real cell, where gradients can spread out in three dimensions, an instability would occur after such a long time.

We have also searched for the nonlinear behavior reported by Owers-Bradley[63] in which a periodic ringing signal was observed for up to 10 msec following a pair of very closely spaced 90° pulses, but could find no evidence for a similar behavior in our experiment.

3.6 Summary and Conclusions

In summary, we have measured the coefficient of longitudinal spin diffusion in dilute ^{3}He-^{4}He solutions with ^{3}He concentrations of 350 and 1940 ppm. In both the high- and low-concentration mixtures, we find that our data smoothly cross over from a high-temperature regime where $D_{\|}$ decreases with decreasing T to a low temperature regime where $D_{\|}$ increases with decreasing T. In neither case did we observe behavior similar to that seen by Gully and Mullin at low temperatures. For the lower concentration, the agreement between our measured values of $D_{\|}$ and theoretical calculations[44] is excellent. The lack of equally good agreement in the higher-concentration case remains something of a puzzle. In addition, we have been able to compare our results for $D_{\|}$ in the 1940-ppm solution with Candela *et al.'s* results[15] for the coefficient of transverse spin diffusion $D_{\perp}$. Within the combined experimental error of the two sets of data, we do not observe a significant difference between $D_{\|}$ and $D_{\perp}$, which is consistent with theoretical predictions for this relatively high-temperature regime.[44]

Our attempts to measure $D_\perp$ with a spin-echo technique were less successful. While the strong multiple spin-echo behavior we observed confirms the presence of large molecular fields in the system, the lack of agreement between our data and theoretical predictions, and, in particular, the failure of the echo amplitudes to scale as expected with field gradient and interpulse delay, prevented us from measuring both $D_\perp$ and the spin rotation parameter μ, directly. For the moment, we consider it likely that rf and static magnetic field inhomogeneities across our relatively large sample cell are the source of the discrepancies. If such experimental difficulties could be surmounted, however, the technique of multiple spin echoes promises to be a powerful tool for the investigation of highly polarized systems. They are a large-amplitude probe that should be sensitive to the existence of the as yet unobserved diffusion anisotropy, and should provide information about the exact form of the spin dynamics in the highly polarized regime. This last point is particularly important, as such information cannot be obtained from spin-wave experiments and other small-amplitude probes that are only sensitive to the linearized spin dynamics of the system.

Finally, we have observed a very long-time-scale excitation in the system which we believe is driven by a non-linear instability in the spin dynamics. While we have developed a simple computer model that reproduces some key aspects of this behavior, our understanding of this phenomenon is still somewhat preliminary. Examination of the spin dynamics in the simulated sample cell indicate that the experimental signals may have their origin in a “half-soliton”-like mode, but it is important to emphasize that we are still uncertain as to what extent the computer model actually describes our experiment. While we are able to generate numerical signals whose overall time scale matches that of the experiment, and which depend on such external parameters as magnetic-field gradient and temperature in roughly the correct fashion, we are unable to reproduce the dramatic “bursting” behavior observed in the experiment.

It is clear that much work, both experimental and theoretical, remains to be done in order to fully understand this behavior. Any future simulations should incorporate more spatial dimensions. If the bursting behavior depends in some fashion on the geometry of the channel, it may appear in a two- or three-dimensional simulation that can more accurately describe the spin dynamics in all three regions of the sample cell. It may also be possible to find a solvable analytical treatment in the unstable region, which would likely offer more insight than a simple numerical integration. From an experimental point of view, since we believe the driving mechanism for these oscillations depends on the flow of spins through the small channel in the cell, it would be extremely interesting to be able to control that flow by changing the cell geometry (e.g. , with a movable partition) from outside the cryostat. Attempting to alter the behavior during the course of the oscillation by, for example, applying a pulsed gradient, may also prove revealing.

3.7 Acknowledgments

We are grateful to W. J. Mullin for providing us with theoretical calculations of $D_{\parallel}$ for our concentration and field, and to D. Candela for providing us with his data on $D_{\perp}$. We thank both of them, as well as J. P. Sethna, A. S. Bedford, R. M. Bowley, J. R. Owers-Bradley, and J. H. Freed, for stimulating and helpful discussions. We are also grateful to R. W. Nelson and S. A. Teukolsky for help with our simulations of the long-time-scale oscillations, and to E. N. Smith for help with the apparatus. This work was supported by the NSF under Grant No. DMR-9011562 and through the Cornell Materials Science Center via Grant No.

DMR-8818558-A02. We gratefully acknowledge the support provided to GN. by IBM Research Division, to A.M.P. by NSERC of Canada, and to D.L.H. by AT&T Bell Laboratories.

REFERENCES FOR CHAPTER 3

[1] S. Stringari, ed., in *Spin Polarized Quantum Systems* (World Scientific, Singapore, 1989); A. E. Meyerovich, in *Helium Three*, edited by W. P. Halperin and L. P. Pitaevskii (North-Holland, Amsterdam, 1990).

[2] A. J. Leggett and M. J. Rice, Phys. Rev. Lett., **20**, 586 (1968).

[3] A. J. Leggett, J. Phys. C., **3**, 448 (1970).

[4] L. R. Corruccini, D. D. Osheroff, D. M. Lee, and R. C. Richardson, Phys. Rev. Lett., **27**, 650 (1971); L. R. Corruccini, D. D. Osheroff, D. M. Lee, and R. C. Richardson, J. Low Temp. Phys., **8**, 229 (1972).

[5] E. P. Bashkin, Pis'ma Zh. Eksp. Teor Fiz., **33**, 11 (1981), [JETP Lett. **33**, 8 (1981)].

[6] C. Lhuillier and F. Laloë, J. Phys. (Paris), **43**, 197 (1982); C. Lhuillier, J. Phys. (Paris), **44**, 1 (1983).

[7] L. P. Lévy and A. E. Ruckenstein, Phys. Rev. Lett., **52**, 1512 (1984); A. E. Ruckenstein and L. P. Lévy, Phys. Rev. B, **39**, 183 (1989).

[8] B. R. Johnson, J. S. Denker, N. Bigelow, L. P. Lévy, J. H. Freed, and D. M. Lee, Phys. Rev. Lett., **52**, 1508 (1984).

[9] D. Einzel, G. Eska, Y. Hirayoshi, T. Kopp, and P. Wölfle, Phys. Rev. Lett., **53**, 2312 (1984).

[10] N. Masuhara, D. Candela, D. O. Edwards, R. F. Hoyt, H. N. Scholz, D. S. Sherrill, and R. Combescot, Phys. Rev. Lett., **53**, 1168 (1984); D. Candela, N. Masuhara, D. S. Sherrill, and D. O. Edwards, J. Low Temp. Phys., **63**, 331 (1986).

[11] J. R. Owers-Bradley, H. Chocholacs, R. M. Mueller, C. Buchal, M. Kubota, and F. Pobell, Phys. Rev. Lett., **51**, 2120 (1983); J. R. Owers-Bradley and R. M. Bowley, J. Low Temp Phys., **63**, 331 (1986).

[12] H. Akimoto, T. Kawae, G.-H. Oh, O. Ishikawa, T. Hata, T. Kodama, and T. Shigi, Jpn. J. Appl. Phys., **26-3**, 65 (1987).

[13] H. Ishimoto, H. Fukuyama, N. Nishida, Y. Miura, Y. Takano, T. Fukuda, T. Tazaki, and S. Ogawa, Phys. Rev. Lett., **59**, 904 (1987).

[14] P. J. Nacher, G. Tastevin, M. Leduc, S. B. Crampton, and F. Laloe, J. Phys. Lett. (Paris), **45**, L441 (1984).

[15] D. Candela, D. R. McAllaster, L.-J. Wei, and G. A. Vermulen, Phys. Rev. Lett., **65**, 595 (1990); D. Candela, D. R. McAllaster, and L.-J. Wei, Phys. Rev. B, **44**, 7510 (1991).

[16] W. J. Gully and W. J. Mullin, Phys. Rev. Lett., **52**, 1810 (1984).

[17] A. E. Meyerovich, Phys. Lett., **107A**, 177 (1985).

[18] J. W. Jeon and W. J. Mullin, J. Low Temp. Phys., **67**, 421 (1987).

[19] J. W. Jeon and W. J. Mullin, Phys. Rev. Lett., **49**, 1691 (1988); J. W. Jeon and W. J. Mullin, Phys. Rev. Lett., **62**, 2691 (1989).

[20] A. Abragam, *Principles of Nuclear Magnetism* (Oxford University Press, Oxford, 1961).

[21] C. P. Slichter, *Principles of Magnetic Resonance* (Springer, Berlin, 1980).

[22] G. Nunes, Jr., C. Jin, A. M. Putnam, and D. M. Lee, Phys. Rev. Lett., **65**, 2149 (1990).

[23] W. P. Kirk and M. Twerdochlib, Rev. Sci. Instrum., **49**, 765 (1978).

[24] D. S. Greywall, Phys. Rev. B, **33**, 7520 (1986).

[25] E. D. Adams, J. M. Delrieu, and A. Landesman, J. Phys. (Paris), **39**, L190 (1986).

[26] G. Nunes, Jr., Rev. Sci. Instrum., **61**, 1154 (1990).

[27] W. N. Hardy and L. A. Whitehead, Rev. Sci. Instrum., **52**, 213 (1981).

[28] N. Bloembergen and R. V. Pound, Phys. Rev., **95**, 9 (1954).

[29] S. Bloom, J. Appl. Phys., **28**, 800 (1957).

[30] G. Nunes, Jr., Ph.D. thesis, Cornell University (1991), (unpublished).

[31] A. Ghozlan and E. Varoquaux, Ann. Phys. (Paris), **4**, 239 (1979).

[32] J. R. Owers-Bradley, R. M. Bowley, and P. C. Main, J. Low. Temp. Phys., **60**, 243 (1985).

[33] B. R. Johnson, Ph.D. thesis, Cornell University (1984), (unpublished).

[34] R. C. Richardson and E. N. Smith, eds., *Experimental Techniques in Condensed Matter Physics at Low Temperatures* (Addison-Wesley, New York, 1988).

[35] J. C. Maxwell, *A Treatise on Electricity and Magnetism*, 3rd ed., Vol. 1 (Oxford, London, 1892) p. 434.

[36] G. H. B. Godfrin, H. Frossati and D. Thoulouze, J. Phys. (Paris) Colloq., **41**, C7 (1980).

[37] N. Bloembergen, ed., *Nuclear Magnetic Relaxation* (Benjamin, New York, 1961).

[38] F. Mullin, W. J. Laloë and M. G. Richards, J, Low Temp. Phys., **80**, 1 (1990).

[39] P. C. Hammel and R. C. Richardson, Phys. Rev. Lett., **53**, 1441 (1984).

[40] J. F. Kelly and R. C. Richarson, in *Proceedings of the Thirteenth International Conference on Low Temperature Physics*, Vol. I (Plenum, New York, 1974) p. 167; J. F. Kelly, Ph.D. thesis, Cornell University (1974), (unpublished).

[41] R. C. Samaratunga, K. P. Martin, J. S. Brooks, and G. O. Zimmerman, J. Appl. Phys., **54**, 6421 (1983).

[42] H. Godfrin, G. Frossati, M. Thoulouze, D.and Chapellier, and W. G. Clark, J. Phys. (Paris) Colloq., **39**, C6 (1978).

[43] R. Kumaresan and D. W. Tufts, IEEE Trans. Acoust., Speech, Signal Process., **ASSP-30**, 833 (1982); H. Barkhuijsen, R. de Beer, W. M. M. J. Bovée, and D. van Ormondt, J. Magn. Res., **61**, 465 (1985).

[44] W. J. Mullin and J. W. Jeon, J. Low Temp. Phys., **88**, 433 (1992); W. J. Mullin, (private communication).

[45] C. Ebner, Phys. Rev., **156**, 222 (1967).

[46] R. M. Bowley, (private communication).

[47] G. Deville, M. Bernier, and J. M. Delrieux, Phys. Rev. B, **19**, 5666 (1979).

[48] G. Eska and *et al.*, Physica B (Utrecht), **108**, 1155 (1981).

[49] J. S. Denker, N. P. Bigelow, D. Thompson, J. H. Freed, and D. M. Lee, Physica B (Utrecht), **108**, 549 (1984).

[50] R. Bowtell, R. M. Bowley, and P. Glover, J. Magn. Res., **88**, 643 (1990).

[51] A. S. Bedford, R. M. Bowley, J. R. Owers-Bradley, and D. Wightman, J. Low Temp. Phys., **85**, 389 (1991).

[52] J. R. Owers-Bradley, D. R. Wightman, R. M. Bowley, A. Bedford, and A. Child, (unpublished); J. R. Owers-Bradley, D. R. Wightman, R. M. Bowley, and A. Bedford, Physica B (Utrecht), **165**, 729 (1990).

[53] A. S. Bedford, (private communication).

[54] D. Candela, (private communication).

[55] F. J. Low and H. E. Rorschach, Phys. Rev., **120**, 1111 (1960).

[56] J. C. Kemp, J. Appl. Phys., **30**, 1451 (1959).

[57] E. M. Purcell, Phys. Rev., **69**, 681 (1946).

[58] B. Castaing, Physica B (Utrecht), **126**, 212 (1984).

[59] A. E. Meyerovich, in *Progress in Low Temperature Physics*, Vol. XI, edited by D. F. Brewer (North-Holland, Amsterdam, 1987).

[60] W. H. Press, B. P. Flannery, S. A. Teukolsky, and W. T. Vetterling, *Numerical Recipes* (Cambridge University Press, New York, 1986).

[61] L. P. Lévy, Phys. Rev. B, **31**, 7077 (1985).

[62] H. C. Fogedby, J. Phys. A, **13**, 1467 (1980).

[63] J. R. Owers-Bradley, Physica B (Utrecht), **169**, 190 (1991).

Chapter 4

Effects of domain walls in dilute spin polarized solutions of ^{3}He in superfluid ^{4}He[†]

4.1 Abstract

Simulations are under way to study transient phenomena in spin polarized dilute ^{3}He-^{4}He mixtures following a 180° NMR pulse. The computer models are designed to test the hypothesis that domain walls produced by the 180° pulse induce spin wave resonances as the domain wall moves along the cell in a field gradient.

4.2 Introduction

Very dilute mixtures of nuclear spin polarized ^{3}He in superfluid ^{4}He provide systems which are in many ways analogous to dilute spin polarized gases at low temperatures.[1] Spin waves have been shown to propagate[2] in these dilute mixtures and the Leggett-Rice effect[3] has also been observed.[4,5] Some years ago, Nunes *et al.*[6] observed long-lived transient effects in pulsed nuclear magnetic resonance (NMR) experiments following a single 180 degree pulse. The effects could be seen only for

---

[†] Reprinted with permission from D. L. Hawthorne, V. V. Khmelenko, and D. M. Lee, in *Proceedings of the Twenty-Sixth International Conference on Low Temperature Physics* (To be published).

very low concentrations of ^{3}He (350 ppm), where very low Fermi degeneracy temperatures mitigated the effects of Pauli blocking,[7] thus allowing large polarizations to develop.

The equation governing spin wave phenomena in highly polarized fluids (gases or liquids) was first derived by Leggett and Rice[3] (L-R) for pure liquid ^{3}He. The equation, which is basically non-linear, describes the departure of spin diffusion from the low polarization limit in terms of a molecular field. The precession of spin currents then becomes important when the scattering length and hence the spin diffusion time becomes long as Fermi-Dirac degeneracy sets in. A linearized version of the L-R equation, discussed by Lhuillier and Laloe[8], was used to describe nuclear spin wave phenomena in rarefied spin polarized hydrogen gas, first observed by Johnson *et al.*[1]. Bashkin[9] and Lévy and Ruckenstein[10] used a molecular field approach to discuss these phenomena. Spin waves were also observed in spin polarized ^{3}He gas[11] by a group at École Normale Supérieur in Paris using optical pumping techniques to achieve the nuclear polarization. The spin wave phenomena observed in these highly dilute systems did not require quantum degeneracy (as required for pure liquid ^{3}He).

4.3 Early Experiments

Nunes *et al.*[6] observed interesting transient effects following a single 180° NMR pulse in a 350 ppm mixtures of ^{3}He in superfluid ^{4}He with the polarization being provided by an applied magnetic field of 9 Tesla. The NMR frequency was 300 MHz. Temperatures ranging down to 4mK were obtained via a dilution refrigerator. The apparatus has been described in detail in reference 6 and in Geoffrey Nunes Ph.D. thesis.[12] The experimental arrangement is shown schematically in figure 4.1. It consisted of two separate chambers connected by a short tube (ra-

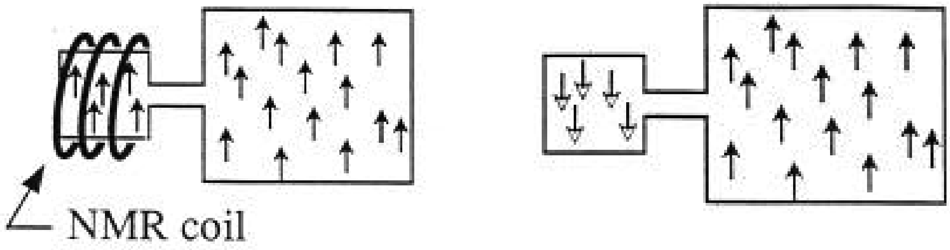

Figure 4.1: A schematic of the sample cell before and after the application of a 180 degree pulse to the NMR coil (which is in practice a loop-gap resonator tuned to 300 MHz.) A domain wall will move from the connecting tube down the cell from right to left in this figure.

dius 0.122 cm, length 0.36 cm). The cell was first used to measure the longitudinal spin diffusion following a 180 degree pulse which was found to reach a minimum at 10 mK for the 350 ppm ^{3}He-^{4}He mixture. During these measurements, for small or zero applied gradients, a long lived train of echo patterns was observed which varied with field gradient and temperature. The temperature dependence of a set of echo trains is shown in figure 2 for temperatures of 10.4 mK and 4.8 mK.[6,12] The patterns are strongly dependent on temperature with spacing of the bursts being very small at the lowest temperatures.[6]

The equation describing the L-R effect and most of the other spin dynamics we shall be discussing was studied in more detail by Leggett.[13] (We will continue to call it the L-R equation to distinguish it from the equations developed by Leggett to describe the spin dynamics of superfluid ^{3}He).[14] The full L-R equation is (with $\mathbf{M}(\vec{r},t)$=the polarization):

$$\frac{\partial \mathbf{M}}{\partial t}(\vec{r},t) - \mathbf{M} \times \gamma\delta\mathbf{H}(\vec{r}) =$$
$$D_S \sum_{i=1}^{3} \frac{\partial}{\partial x_i}\left[\frac{1}{1+\mu^2 M^2}\left\{\overrightarrow{\nabla}\mathbf{M} + \mu(\mathbf{M}\times\overrightarrow{\nabla}\mathbf{M}) + \mu^2(\mathbf{M}\cdot\overrightarrow{\nabla}\mathbf{M})\mathbf{M}\right\}\right], \tag{4.1}$$

This equation can represent the spin dynamics of classical as well as degenerate polarized quantum gases. It can be linearized for the purpose of treating small amplitude oscillations m_+, transverse to the applied steady magnetic filed, H_0. The linearized equation is

$$\frac{\partial m_+}{\partial t} = D_S \frac{i - \mu M_z}{1 + \mu^2 M_0^2} \nabla^2 m_+ + \gamma \delta H m_+. \tag{4.2}$$

This equation is approximately isomorphic to the Schrödinger equation (modified by a small dissipative term) so that solutions in various potentials (linear, harmonic oscillator, square well, etc.) can be carried over from known solutions of the Schrödinger equation. In particular, it can yield spin waves, where the potential gradient term corresponds to the gradient in the applied magnetic field. Thus for example, spin eigenfrequencies correspond to Airy functions[15] for a linear magnetic field gradient. The quantities μ and M are of crucial importance. The term μ is called the spin rotation parameter and it must be of sufficiently large magnitude for spin waves to occur. If Ω_{int} corresponds to the precession frequency in a molecular field, then μM $= \Omega_{int}\tau_D$ where τ_D is the mean diffusion time and μ is the strength of the molecular field. The quantity μM can be thought of as a spin wave figure of merit. It depends strongly on the temperature, increasing rapidly from 30 mK down to 3 mK.[12] (In the Fermi degenerate regime, M changes slowly so μ will be the dominant quantity.) Jeon and Mullin[16] have performed extensive theoretical studies of magnetic phenomena relevant to the present work, including the rapid dependence of μM on temperature. One would expect that the adjacent spin wave lines should become closer together as T decreases. This appears to correlate with the decreased spacing between bursts at the lowest temperatures shown in Figure 4.5. The spin wave spectrum for the linearized L-R equation is very sensitive to the field gradient, with the spin wave spectra behaving as follows for three different gradients: For the one dimensional square well potential the spin wave modes get farther apart with increasing magnetic field; they remain equally spaced for the harmonic oscillator potential; and they become more closely spaced for the linear potential for increasing magnetic fields. The bursting phenomena corresponding to the echo trains turned out to be very sensitive to the applied magnetic field gradients which ranged from .01 - .14 gauss/cm. For studies in fields of 9 tesla this would require knowledge of the actual field gradient to a few parts per million. Unfortunately, residual gradients lead to errors in estimating the actual gradient dependence. For figure 2, the reader should notice the long delay time before the onset of the bursting phenomenon, although prompt echos are sometimes observed. To describe the influence of the 180° pulse on the sample, the non-linear L-R equation is required. Of particular importance is an instability first introduced by Castaing while considering the rapid melting of highly polarized solid ^{3}He.[17] This instability was basically a feature of the (non-linear) L-R equation. A large disturbance of the spins could lead to a region where a large population precessed in the plane perpendicular to the steady applied field H_0. In these experiments the Castaing instability could give rise to a domain wall separating the up spins in the cell (following the 180 degree pulse) from the down spins in the volume to the left of the narrow channel. Simulations performed by Nunes[6] showed that this led to the formation of a domain wall which traversed the cell from right to left. Within the domain wall the spins were in the transverse plane, and consequently were expected to precess at the local Larmor frequency. The Larmor frequency of the signals tended to vary (chirp) as the domain wall moved through the cell due to the field gradient. The domain wall also tended to broaden as it traversed the cell.

In the experiments of Nunes, *et al.*[6] a very curious memory effect was observed. If a 180 degree NMR pulse was applied to the sample 30 minutes after the previous 180 degree pulse, the burst pattern was entirely different. It required a time interval

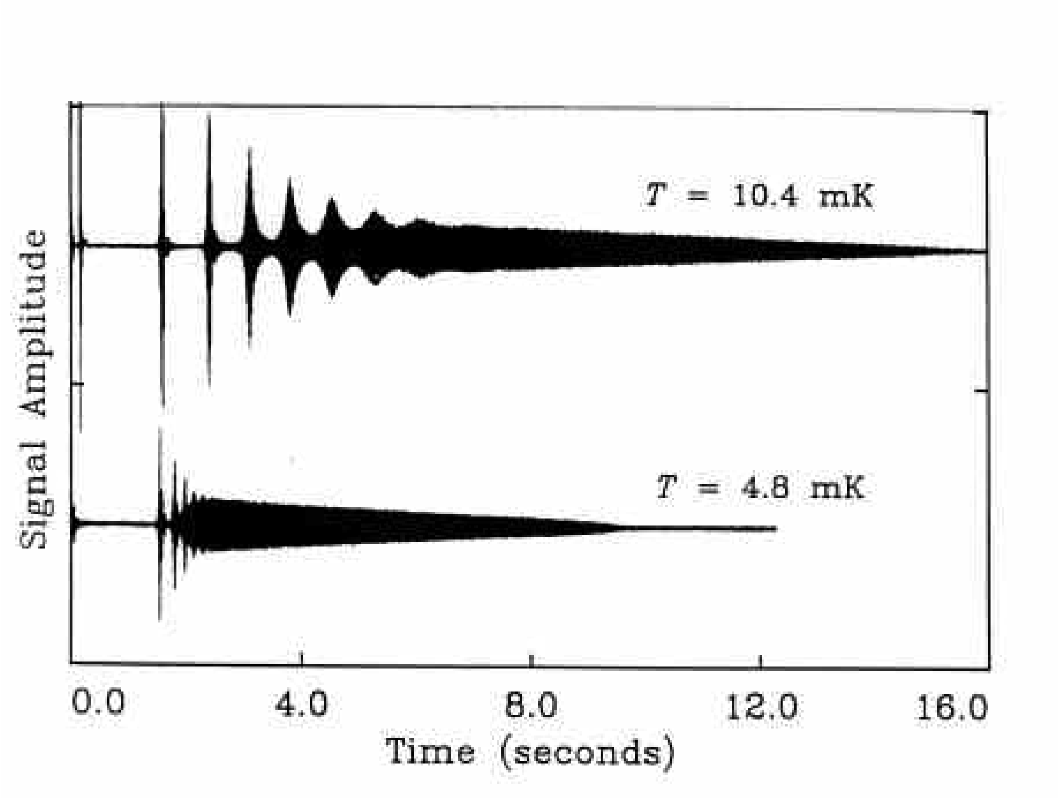

Figure 4.2: Long time scale oscillations. The large reduction in the burst spacing when T is reduced from 10.4 to 4.8 mK results from the increase of μM with decreasing temperature.

of more than one hour between the two successive 180° pulses for the burst pattern to return to its original form.

4.4 Recent Simulations

The striking phenomena discussed in the previous section were not fully understood at the time. In the meanwhile, computer technology has improved to a considerable extent. Therefore the decision was made to perform further computer simulations in an attempt to better understand the observations. One of the goals is to test the hypothesis that the very long lasting coherent precession of the transverse component of the magnetization within a domain wall would generate spin wave resonances when the Larmor frequency varied due to the progression of the domain wall along the cell. Dmitriev[18] has discussed the coherent precession of spins within domain walls in normal ^{3}He and ^{3}He-^{4}He mixtures for very low polarizations and low temperatures. We believe that the domain wall acts as a weak variable frequency source as it moves through the magnetic field gradient. When this frequency matches a spin wave resonance in the cell, the result should be a sharp rf burst which can be detected by the receiver. The simulation is designed to register these resonances. The domain wall itself may also serve as a reflecting boundary condition which could affect the burst patterns. A related phenomena was observed by Owers-Bradley[19] who saw a 10 msec periodic ringing signal after two closely spaced 90° pulses. A second goal of the simulation is to model the domain wall motion in order to determine the cause of the long term memory effects discussed in the previous section. The effects could be explained by the fact that the domains break up into smaller domains which could become pinned by the boundaries and therefore might persist for longer periods of time. Alternatively, the original domain wall itself could be pinned.

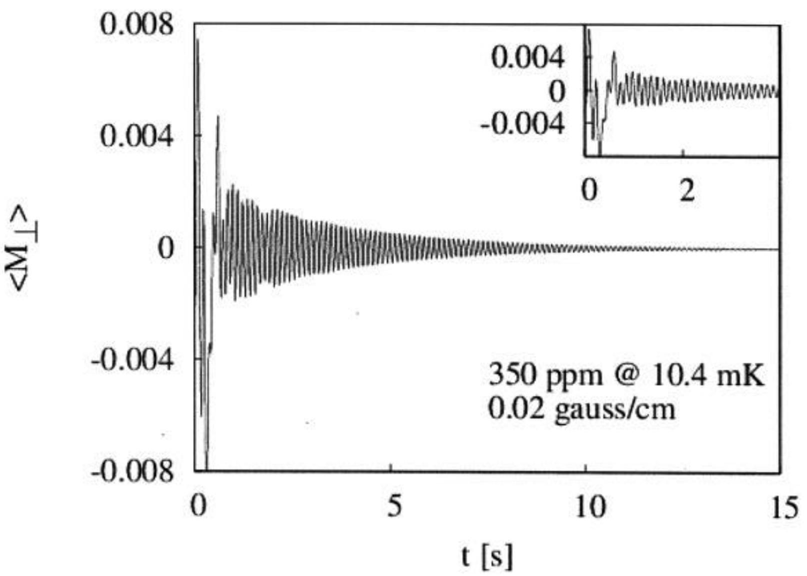

Figure 4.3: Simulation for the NMR signal in an axial gradient of 0.02 Gauss per cm following a 180 pulse at T=10.4 mK. The very sharp bursts at the beginning of the trace are shown more clearly in the inset. They are followed by a weakly modulated decay pattern lasting 9 seconds.

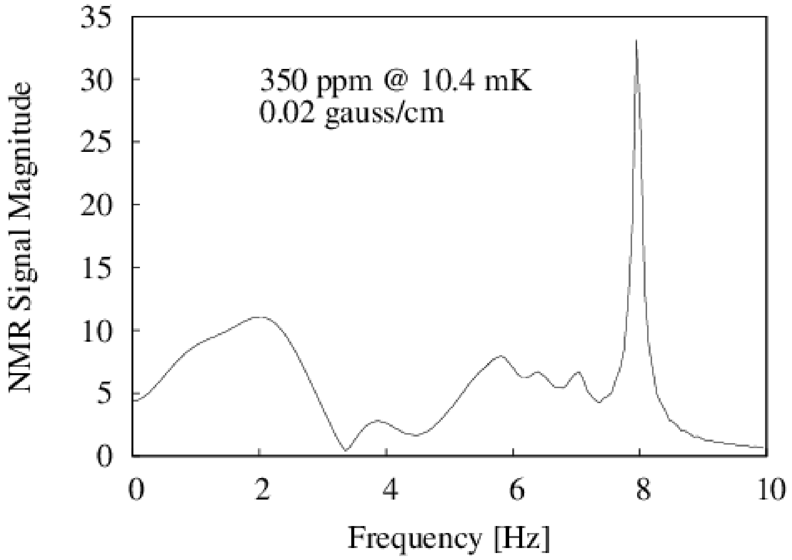

Figure 4.4: A Fourier transform of the data in the rotating frame as shown in figure 3. The region between 4 and 9 Hz appears to be similar to the spin wave spectra seen in polarized hydrogen gas.

So far, simulations have been conducted only for one dimensional geometries. Short term structures are observed in the first few seconds following the 180° pulse which seem to roughly correspond to the burst patterns observed with the signal dying out after about 9 seconds. (see figure 3.) Fourier transforms of the time spectrum of figure 3 show a pattern suggestive of spin wave Airy function modes as observed in spin polarized hydrogen[15] (see figure 4). A domain wall shown in figure 5 moves along the cell, and the structure is still observed after 7 seconds indicating a persistent coherent spin precession within the domain wall for this period of time. More realistic two dimensional simulations are now under way. The addition of side walls could alter the domain wall motion and possibly lead to stabilization of the domain structures. The simulations have not yet accounted for the relatively stable structures observed in the experiments over hour long durations. Finally the phenomena observed in the experiments do not seem to correspond to the purported Bose-Einstein condensation of magnons[20] seen in ^{3}He-B since the coherent precession takes place only within the domain walls.

4.5 Conclusion

So far the results of the simulations seem to indicate that the observed experimental phenomena[6] can be at least roughly described in terms of domain walls. More extensive modeling is now under way which might provide a more accurate description of the experiments. Future experiments will require a much better regulation of the field gradients, to understand the relation between the spin wave spectra and the bursting phenomena. The memory effect can be much better understood if data could be obtained with shorter time intervals between 180° pulses. The reproducibility of these effects must also be further investigated.

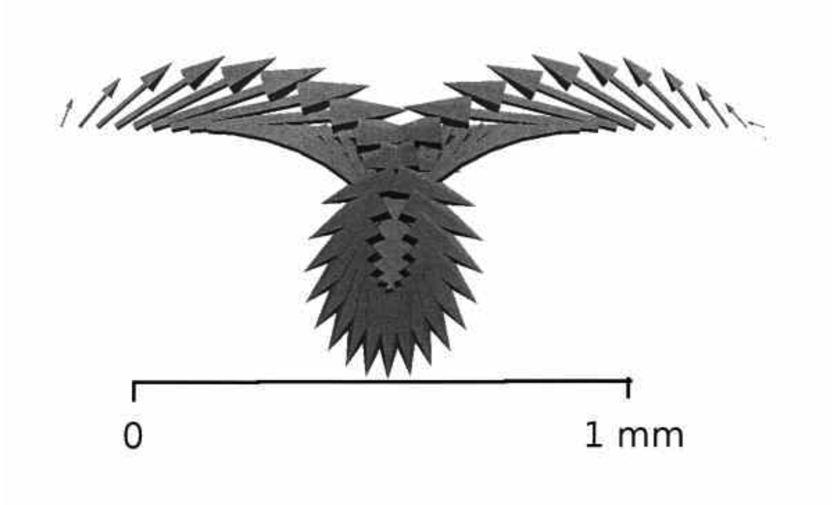

Figure 4.5: This plot is a snapshot of the transverse magnetization as a function of position in the cell. We associate the sharp loop with the formation of a domain wall. Data at later times show that the domain wall progresses along the cell and fades out at the center of the cell after about 7 seconds which is consistent with figure 3. The tails of the arrows correspond to the position in the cell.

4.6 Acknowledgments

The authors thank the Norman Hackerman Advanced Research Program of the State of Texas under grant No. 010366-0137-2009. They are grateful to Dr. Geoffrey Nunes and Prof. Erich Mueller for illuminating advice and discussions. Figures 1 and 2 were adapted from the Ph.D. thesis of Geoffrey Nunes.[6,12]

REFERENCES FOR CHAPTER 4

[1] B.R. Johnson *et al.*, Phys. Rev. Lett., **52**, 1508 (1984).

[2] D. Candela *et al.*, Phys. Rev. Lett., **65**, 595 (1990).

[3] A. Leggett and M. Rice, Phys. Rev. Lett., **20**, 586 (1968).

[4] L.R. Corruccini *et al.*, Phys. Rev. Lett., **27**, 650 (1971).

[5] W. Gully and W. Mullin, Phys. Rev. Lett., **52**, 1810 (1984).

[6] G. Nunes, Jr. *et al.*, Phys. Rev. B, **46**, 9082 (1992).

[7] N. Ashcroft and N. Mermin, *Solid State Physics* (Holt, Rinehart and Winston, Orlando, FL USA, 1961) p. 661.

[8] C. Lhuillier and F. Laloë, J. Phys. C (Paris), **43**, 197 (1983).

[9] E. Bashkin, Pis'ma Zh Eksp Teor Fiz, **33**, 11 (1981).

[10] L. Lévy and A. Ruckenstein, Phys. Rev. Lett., **52**, 1512 (1984).

[11] P.J. Nacher *et al.*, J. Phys. Lett. (Paris), **45**, L441 (1984).

[12] G. Nunes, Jr., Ph.D. thesis, Cornell University (1991), (unpublished).

[13] A. Leggett, J. Phys. C, **3**, 448 (1970).

[14] A. Leggett, Phys. Rev. Lett., **31**, 352 (1973).

[15] N.P. Bigelow *et al.*, Phys. Rev. Lett., **63**, 1609 (1989).

[16] J. Jeon and W. Mullin, J. Low Temp. Phys., **67**, 421 (1987).

[17] B. Castaing, Physica (Utrecht), **126 B**, 212 (1984).

[18] V.V. Dmitriev *et al.*, Physica B, **210**, 366 (1984).

[19] J. Owers-Bradley, Physica B, **169**, 190 (1991).

[20] Y. Bunkov, J. Low Temp. Phys., **158**, 118 (2010).

Chapter 5

Long wavelength dynamics in a 1D planar ferromagnet: Magnetostatic modes and soliton-induced damping in $\mathbf{CsNiF_3}$[†]

5.1 Abstract

Above 2.6 K, $CsNiF_3$ is an excellent example of a soliton-bearing spin-chain system. We have studies the long wavelength excitation in $CsNiF_3$ by spin resonance, using a strip line technique that couples to finite q excitations. In addition to the uniform precessing mode, we have observed a magnetostatic resonance. It lies at a lower energy than the uniform mode, consistent with the spectrum expected in linear response. The uniform mode, however, broadens much more rapidly with temperature. We propose that a dipolar magnon-soliton interaction is the dominant channel for the relaxation of long wavelength excitations in the quasi-1D system.

[†] Reprinted with permission from D. H. Reich, L. P. Lévy, and D. L. Hawthorne, J. Appl. Phys., **69**, 5950 (1991). Copyright ©1991 American Institute of Physics.

5.2 Introduction

The presence of quantum fluctuations at arbitrarily long length scales is responsible for the destruction of long-range order in one-dimensional (1D) systems. The absence of rigidity in the ground state allows a host of nonlinear excitations, even at low temperature. Some 1D magnetic systems can be approximately mapped onto exactly soluble nonlinear models. They have been an excellent testing ground for the novel nonlinear excitations (solitons, breathers, an instantons) present in a number of nonlinear field theories.[1] For example, it is possible to give an approximate description of $\mathrm{CsNiF_3}$, a quasi-1D ferromagnet,[2] with a sine-Gordon Hamiltonian.[3] In $\mathrm{CsNiF_3}$, the $\mathrm{Ni^{2+}}$ ions (S=1) are arranged in well-separated chains with exchange coupling only along the chains. An easy-plane symmetry perpendicular to the chain axis ($\hat{\mathbf{z}}$) is produced by single-ion anisotropy. It can be broken by a dc magnetic field Hx perpendicular to the chain. The associated 1D Hamiltonian is

$$H_{1D} = -J \sum_i \mathbf{S}_i \cdot \mathbf{S}_{i+1} + A \sum_i (S_i^z)^2 - \mu H_x \sum_i S_i^x, \tag{5.1}$$

Where $J = 30$ K, $A = 6$ K, and $\mu = 2.25\mu_B$.[†] In the semi-classical limit (large $\widetilde{S} = [S(S+1)]^{1/2}$), the excitation spectrum is composed of noninteracting magnons and solitons that can be viewed as a 2π twist of the spins about the $\hat{\mathbf{z}}$ axis of size $1/k_0 = (J\widetilde{S}/\mu H)^{1/2}$ and energy $\epsilon_S = 8k_0 J\widetilde{S}^2$. Within this ideal gas picture of noninteracting excitations, the equilibrium and dynamical properties of this model have been compared to specific heat[6] and neutron scattering[4] experiments on $\mathrm{CsNiF_3}$. While these experiments have provided strong qualitative evidence for solitons,[7] the limitations of this classical description for an $S = 1$ spin chain have become apparent. The inclusion of quantum effects as renormalization of

---

[†] These parameters are determined from a fit of neutron scattering data (Refs. 2 and 4), including the effects of quantum fluctuations. See Ref. 5

the magnon and soliton energies has resolved some of the quantitative differences between theory and experiment,[8,9,10] but interaction effects between magnons and solitons are also thought to be relevant. In fact, dipolar interactions not included in the Hamiltonian [5.1] determine the three dimensional antiferromagnetic order which takes place below $T_N = 2.6$ K. It is therefore natural to consider their effects in the 1D phase at $T > T_N$.

The spin-resonance experiments described here are conducted at very long wavelength (approaching the sample size) where dipolar effects are felt most strongly. At these wavelengths, magnons are no longer the normal modes of the system. The correct modes are the magnetostatic, or Walker modes,[11] whose spectrum is determined by the coupling of the magnetization $\mathbf{m}$ to the magnetic field $\mathbf{h}$ through Maxwells equation, $\nabla \cdot (\mathbf{h} + 4\pi\mathbf{m}) = 0$, and by the boundary conditions on $\mathbf{h}$ at the surface of the sample. Our data are consistent with the magnetostatic modes in our geometry; in particular, the uniform precession mode lies at an energy higher than the other magnetostatic modes, which are close to the bottom of the spin-wave band. What cannot be explained by conventional magnon relaxation processes is the qualitatively different broadening of the uniform and magnetostatic modes as the temperature is increased. On the other hand, interactions between magnons and solitons will be shown to provide a highly selective decay process at long wavelength that qualitatively describes the data.

The coupling of a finite wavelength magnetic excitation is achieved through an electromagnetic field that is spatially periodic on a scale small compared with its free-space wavelength. This can be achieved with microstrip transmission lines that are folded in a meander pattern as shown in 5.2.[‡] The sample is placed on the surface of the pattern. The oscillating magnetic field $\mathbf{h}$ at the surface of the

---

[‡] The actual transmission line structure used, known as "coupled microstrip," consists of two parallel metal strips on an insulating substrate with a ground plane on the back. See Ref 12.

sample is perpendicular to the chain axis ($\hat{\mathbf{z}}$), and has components along the $\hat{\mathbf{x}}$ and $\hat{\mathbf{y}}$ axes that are parameterized as

$$\mathbf{h} = [\hat{\mathbf{x}} h_x \cos(kx) + \hat{\mathbf{y}} h_y \sin(kx)] f(y) \cos(\omega t). \tag{5.2}$$

The function f describes how the field penetrates the sample. $k = 0$ and $k = 2\pi/\lambda$ ($\lambda = 100\mu$m is the strip line wavelength) are the dominant wave vectors excited. The magnetic excitations can be detected as an absorption of the electromagnetic radiation, either in a reflection geometry using one microstrip structure, or in transmission with another similar structure placed on the other side of the sample. The data were taken using a heterodyne spectrometer operating at 20.286 GHz, with an intermediate frequency (IF) of 30 MHz. Through phase-sensitive detection of the IF signal we were able to resolve both components of the susceptibility $\chi(k,\omega) = \chi'(k,\omega) + i\chi''(k,\omega)$. A small amount of DPPH was placed next to the sample as a frequence marker. By looking at its simple, free-spin line shape, and rotating the phase until χ' and χ'' were well separated, we could set the zero of the phase to an accuracy of $\pm 10^\circ$. The dc field was applied with a high homogeneity superconducting magnet. The sample, a single crystal of $\mathrm{CsNiF_3}$ of dimensions $0.2 \times 0.2 \times 1.5$ cm^3, is sufficiently close to a long cylinder that we can approximate the demagnetizing factors as $N_x \approx N_y \approx 2\pi$ and $N_z \approx 0$.

Figure 5.2 shows the dependence of χ'' as a function of magnetic field, measured in transmission at six different temperatures between $T = 2.6$ and 6.0 K. The microwave field strength was nominally 10 Oe at the strip lines. At this level, the observed signals are linear. χ'' is in arbitrary units and traces have been offset for the purpose of display. Except for the strong feature which appears below 1 kOe with the onset of 3D antiferromagnetic ordering at $T = 2.6$ K, the response is characterized by two separate resonances at $H = 2.0$ and 3.5 kOe. The two resonances are well resolved at low temperatures, but merge together at high T

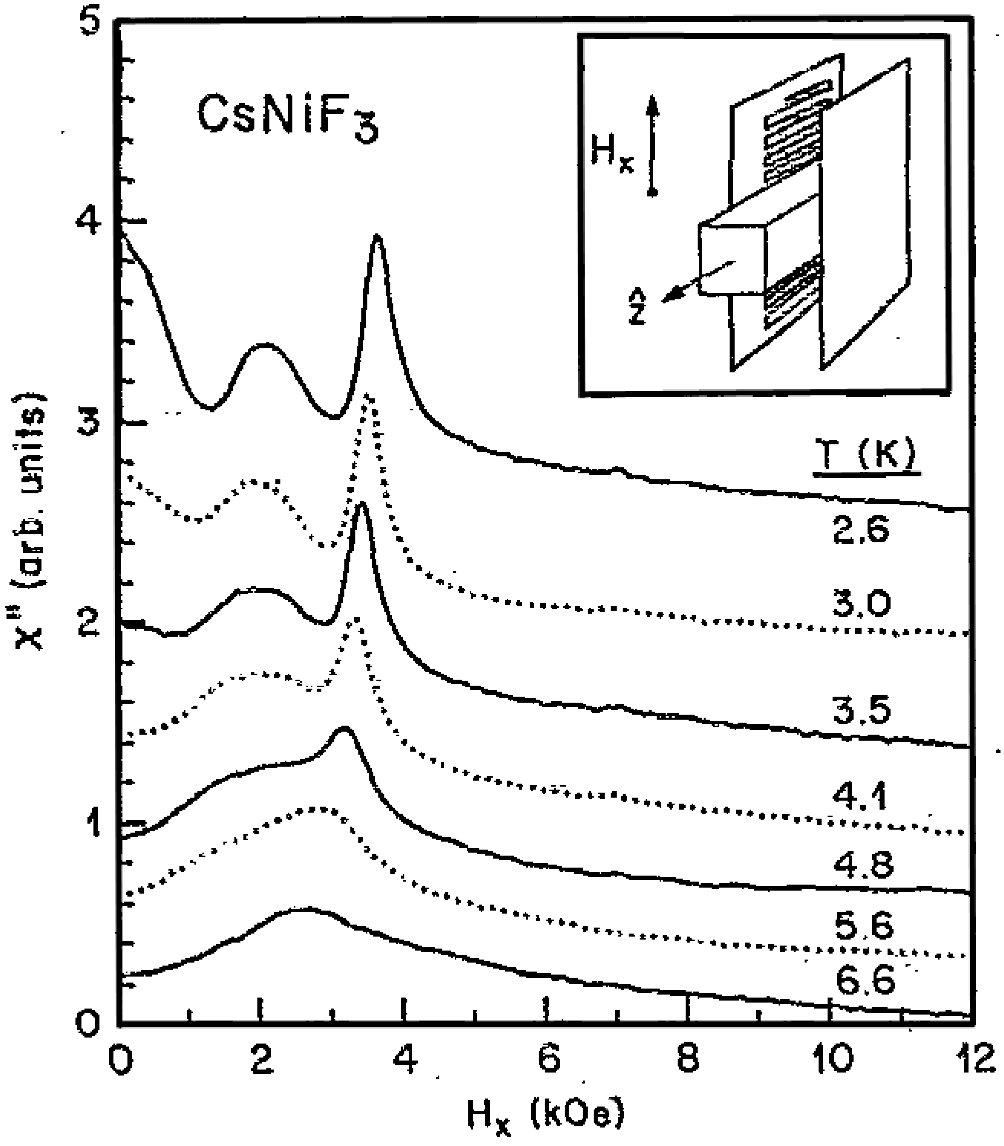

Figure 5.1: χ'' vs magnetic field for 2.6K $\leqslant T \leqslant$ 6K. The traces are offset for clarity. The peaks at $H_x = 2$ and 3.5 kOe are the uniform and Walker modes, respectively. Inset: experimental geometry showing sample sandwiched between two meander strip lines for transmission measurement. The dc field is perpendicular to the chain ($\hat{\mathbf{z}}$) axis.

due to frequency shifts and broadening of the lower mode. We note that the field splitting (1.5 kOe) between the two modes at $T = 2.6$ K is close to the demagnetizing field $H_D = N_x M_0$ at the saturated magnetization ($M_0 \approx 240$ Oe). The splitting decreases with temperature the same way as the magnetization. We show below how this allows us to identify the lower mode with the uniform precession mode and the upper mode with a magnetostatic mode with spatial periodicity λ.

5.3 Harmonic magnons and magnetostatic modes

In spite of the absence of long-range oder, there is a well-defined harmonic approximation[13] to $H_{1D} + H_{dip}$ in the semiclassical limit (large $\widetilde{S}$). Using this $1/\widetilde{S}$ expansion,[5,14,15] the magnon spectrum can be written as $\omega_q = \sqrt{R_1(\mathbf{q})R_2(\mathbf{q})}$, where

$$\begin{aligned} R_1(\mathbf{q}) &= 2J\widetilde{S}(1-\cos(q_z)) + \mu\{H - M[A_{xx}(0) - A_{yy}(\mathbf{q})]\} && (5.3) \\ R_2(\mathbf{q}) &= 2J\widetilde{S}(1-\cos(q_z)) + \mu\{H - M[A_{xx}(0) - A_{zz}(\mathbf{q})]\} + 2A\widetilde{S} && (5.4) \end{aligned}$$

The $A_{jj}(\mathbf{q}) = v_a \sum_r (1 - 3r_j^2/r^2)\exp(i\mathbf{q}\cdot\mathbf{r})/r^3$ are dipolar sums,[§] and give rise to a momentum dependent effective field. At $\mathbf{q} = 0$, $R_1 = \mu[H - M(N_x - N_y)]$ and $R_2 = 2A\widetilde{S} + \mu[H - M(N_x - N_z + 3A^S_{xx})]$. The additional term $A^S_{xx} = 9.781$ appears because the CsNiF$_3$ lattice is non-cubic. Using linear response, we can express the susceptibility in terms of the magnon normal modes:

$$\chi'' = \frac{\Lambda_{jk}\Lambda_{kj}}{\omega^2 - (\omega_q + i\gamma_q)^2}, \tag{5.5}$$

where γ_q is the magnon damping. The Λ_{jk} are constant frequencies such that $\chi_{yy} \gg \chi_{zz} \gg \chi_{xx}$ for fields small compared to the anisotropy. The Walker modes are electromagnetic modes inside the sample determine by

$$\nabla \cdot (\mathbf{h} + 4\pi\mathbf{m}) = [1 + 4\pi\chi_{yy}(\omega)]\frac{\partial h_y}{\partial y} + \frac{\partial h_x}{\partial x} = 0. \tag{5.6}$$

[§] v_a is the volume per spin. See Ref. 16.

This equation is most easily solved for an infinite slab of thickness L (0.2 cm) sandwiched between two strip lines: Upon substituting 5.2 and the small q limit of 5.5 into 5.6, we find well-defined solutions, $f(y) = \cos(\pi n y/L)$, for the discrete frequencies

$$\omega_W^2 = 2A\widetilde{S}\left[H - M\left(N_x - \frac{4\pi}{1 + 4(L/\lambda n)^2}\right)\right] \tag{5.7}$$

where $n(> 0)$ is the the number of nodes of the electromagnetic field between the two strip lines. Since the strip line periodicity is much shorter than the sample dimensions ($L/\lambda \approx 20$), we find that the Walker modes are close in energy even if the finite width of the slab is taken into account, and they lie close to the bottom of the spin-wave band. On the other hand, the uniform mode is well separated and always lies above the Walker modes. Alternatively, the required resonant field H_{res} for the uniform mode is approximately $N_y M$ below the other resonances. This is summarized in Fig. **??**, where we show the relative energy of all the linear modes with respect to the soliton energy.

The observed spectrum is qualitatively consistent with Fig. **??**. The relative splitting between the high-field resonance, which we interpret as unresolved Walker modes, and the low field, or uniform mode, has the right magnitude and correctly follows the magnetization. On the other hand, the two resonant fields are 1 kG higher than expected from Eqs. 5.3, 5.4 and 5.7. This may be attributed to quantum fluctuation as will be discussed elsewhere.[17]

5.4 Soliton-magnon scattering

While the observed spectrum can be explained with linear response theory, it is difficult to understand why the uniform mode broadens more rapidly than the magnetostatic modes: in the 1D phase the average energy of the thermal magnons is between three and eight times the magnon gap. With such a large population, magnon processes should dominate the linewidth. Following Villain,[13] we estimated the four-magnon linewidths of the uniform and magnetostatic modes and found them to be similar at all temperatures. Thus, additional broadening mechanism have to be considered to explain the data.

In ordered ferromagnets, the relaxation of long wavelength modes takes place through momentum nonconserving but energy-conserving processes such as dipolar scattering from rough surfaces.[18] Scattering can thus only take place into magnons degenerate in energy with the long wavelength mode. From Fig. **??**, we note that while the uniform mode has degenerate magnon states available, the Walker modes at the bottom of the spin-band do not.

Solitons are massive classical objects with weak momentum dispersion (**??**) that can absorb momentum with very little change in energy (no recoil). They can be viewed as magnetic defects of size $1/k_0$. In particular, dipolar interaction can scatter the uniform mode off a soliton into degenerate magnons in analogy with surface defect. This scattering will be most effective when the degenerate magnon wavelength becomes comparable to the soliton size. The momentum of the degenerate magnons $q \approx [\mu N_x M/(J\widetilde{S})]^{1/2} \approx 0.1$ is very close to $k_0 = [\mu H/J\widetilde{S}]^{1/2} \approx 0.13$ at the field (2 kOe) used in the experiment. Ignoring the momentum dependence of the dipolar interaction leads to a soliton-induced linewidth of

$$\Gamma \approx 4\pi M n_s \frac{\pi q}{k_0^2} \operatorname{csch}\left(\frac{\pi q}{2k_0}\right) \tag{5.8}$$

for the uniform mode, In Eq. 5.8 n_s is the soliton density. Since $n_s \propto exp(-\epsilon_S/kT)$ increases exponentially with temperature, this process leads to a rapid broadening of the uniform mode with temperature. On the other hand, the Walker modes which have no available final states remain unaffected.

We find that this dipolar scattering between magnons and solitons qualitatively reproduces the temperature dependence of the linewidths observed in our exper-

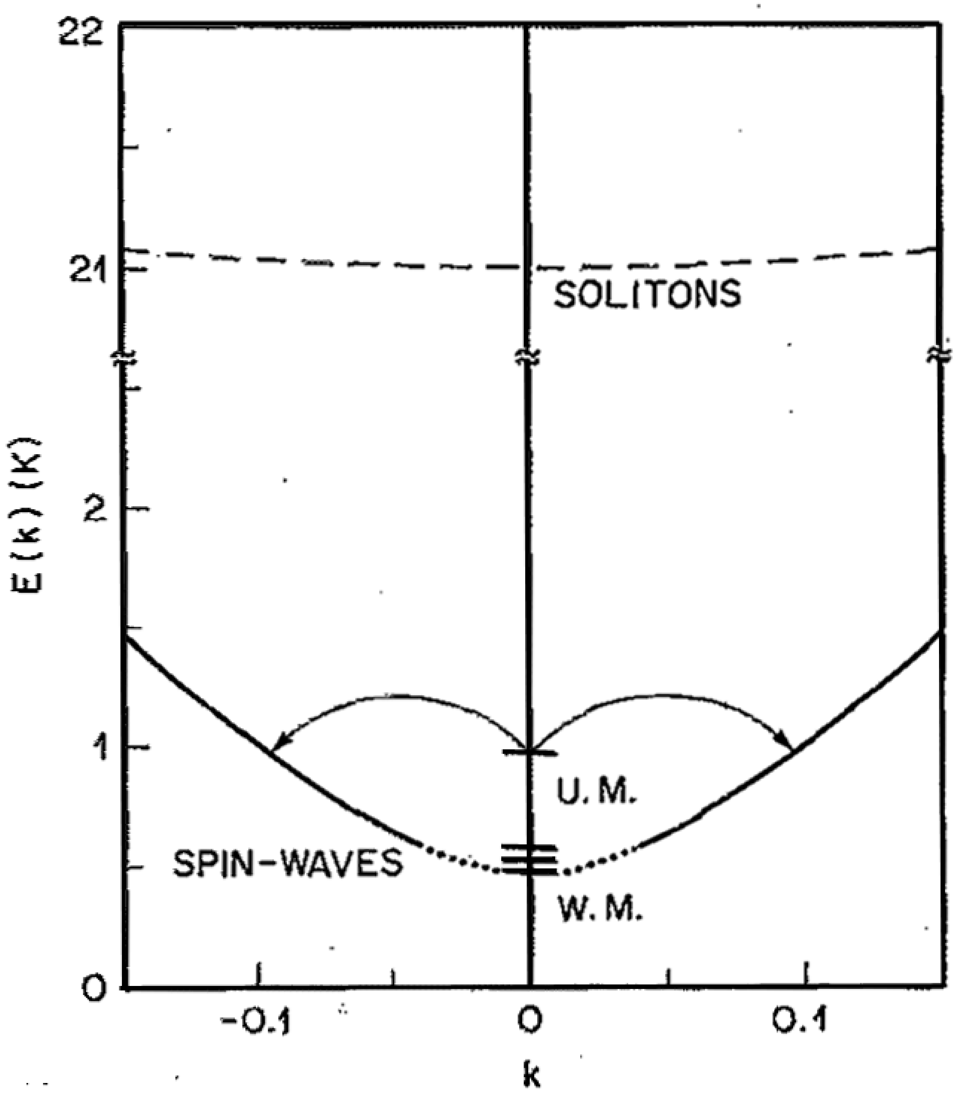

Figure 5.2: Long wavelength excitations in $CsNiF_3$, showing locations of uniform (UM) and Walker (WM) modes relative to the spin-wave (solid line) and soliton (dashed line) bands. The arrows indicate the soliton-mediated decay channel of the uniform mode.

iments. In addition, the magnitude of the observed uniform mode linewidth ≈ 1 kG is consistent with a dipolar interaction [Eq. 5.8]. This gives us confidence that we have correctly identified the dominant broadening process as the dipolar magnon-soliton interaction.

REFERENCES FOR CHAPTER 5

[1] K. Maki, in *Magnetic Properties of Inogranic Quasi-One-Dimensional Materials*, edited by P. Monceau (Riedel, Dordrecht, 1985).

[2] M. Steiner, J. Villain, and C. G. Windsor, Adv. Phys., **25**, 87 (1975).

[3] H. Mikeska, J. Phys. C, **11**, L29 (1978).

[4] M. Steiner, K. Kakurai, and J. K. Kjems, Z. Phys. B, **53**, 117 (1983).

[5] P. S. Riseborough, Solid State Commun., **48**, 902 (1983).

[6] A. P. Ramirez and W. P. Wolf, Phys. Rev. Lett., **29**, 227 (1982); A. P. Ramirez and W. P. Wolf, Phys. Rev. B, **32**, 1639 (1982).

[7] Y. A. Izumov, Usp. Fiz. Nauk, **155**, 553 (1988).

[8] H. C. Fogedby, K. Osano, and H. J. Jensen, Phys. Rv. B, **34**, 3462 (1986).

[9] G. M. Wysin and A. R. Bishop, Phys Rev. B, **34**, 3377 (1986).

[10] H. J. Mikeska, Phys. Rev. B, **26**, 5213 (1982).

[11] L. R. Walker, Phys. Rev., **105**, 390 (1957).

[12] K. C. Gupta, G. Garg, and I. J. Bahl, *Microstrip Lines and Slotlines* (Artech House, 1979).

[13] J. Villain, J. Phys. (Paris), **35**, 27 (1974).

[14] H. J. Mikeska, B. Vaz da Costa, and H. C. Fogedby, Z. Phys. B, **77**, 119 (1989).

[15] P. S. Riseborough, J. Appl. Phys., **61**, 3393 (1987).

[16] L. M. Holmes, J. Als-Nielsen, and H. J. Guggenheim, Phys. Rev. B, **8**, 3323 (1973).

[17] D. H. Reich, L. P. Lévy, and T. Giamarchi, .

[18] M. Sparks, *Ferromagnetic Relaxation Theory* (McGraw-Hill, New York, 1964).

CHAPTER 6

RECENT SIMULATIONS OF SPIN DYNAMICS IN DILUTE ^{3}HE-^{4}HE SOLUTIONS

6.1 Introduction

Attempts to explain the experimental data presented in chapters 3 and 4 left several questions unanswered. Early simulations of the spin dynamics seemed to provide plausible explanations for many aspects of the NMR resonator output, yet failed to explain other features.[1,2] The delayed response could be understood in terms of the time necessary for a longitudinal polarization gradient to develop to the critical point at which the Castaing instability[3] was encountered and longitudinal polarization was converted to transverse polarization through the nonlinearity of the Leggett equation.[4] Also, the frequency modulation or "chirping" of the received signals could be understood as a result of the localized transverse polarization disturbance moving slowly in a magnetic field gradient where the Larmor precession frequency varied with position. However, the early simulation work failed to illuminate the "bursting" phenomena. More recent work presented in chapter 4 showed signs of the bursting behavior.[5] On the other hand, a clear interpretation was not forthcoming. In addition, the recent simulation work generated a new enigma when it failed to reproduce the delayed signal behavior, which was thought to be well understood. In this chapter, we shall address these questions, the bursting behavior and the lack of delay in the more recent simulations of chapter 4.

6.2 Attempt to adapt a computational fluid dynamics package for computational spin dynamics

Researchers in computational fluid dynamics (CFD) have been solving nonlinear partial differential equations numerically for quite some time.[6] It stands to reason that we could adapt the technology developed by CFD researchers for our study of spin dynamics. Indeed, in presenting his linear stability analysis of the Leggett equation, Castaing referred to the instability as *spin turbulence*,[3] turbulence being a topic of considerable interest in the fluid dynamics community. While Castaing predicted the existence of such turbulence, he could say little about the behavior of the spin system inside the unstable region. Proper application of CFD techniques seemed to be a promising way to study such behavior. Given the conclusion that the Castaing instability was responsible in large part for the nonlinear spin dynamics we observed in the laboratory,[1,2] a detailed study of the spin turbulence was most intriguing.

When solving a partial differential equation (or set of equations) numerically, the equation must be converted from its formulation in terms of continuous variables, e.g. space and time, to a discrete form. Here there are several options available, most notably the methods of finite differences, finite elements and finite volumes. Many individuals are familiar with the finite difference method. However, the finite element and finite volume methods tend to be used more often for higher order problems. Of particular importance is the relationship between the finite volume method and problems which include flow variables and conservation laws.[7] Recalling the Leggett equation and the spin density continuity equation, we have

$$\vec{\mathbf{J}}(\vec{r},t) = -\frac{D_s}{1+\mu^2 M^2}[\overrightarrow{\nabla}\mathbf{M} + \mu(\mathbf{M}\times\overrightarrow{\nabla}\mathbf{M}) + \mu^2(\mathbf{M}\cdot\overrightarrow{\nabla}\mathbf{M})\mathbf{M}], \tag{6.1}$$

and

$$\frac{\partial \mathbf{M}}{\partial t}(\vec{r},t) + \overrightarrow{\nabla} \cdot \vec{\mathbf{J}}(\vec{r},t) - \mathbf{M} \times \gamma \delta \mathbf{H}(\vec{r}) = 0. \tag{6.2}$$

Equation 6.1 defines a flow variable $\vec{\mathbf{J}}(\vec{r},t)$, the spin current, while equation 6.2 defines the conservation law for spin density. Such a system of equations is a likely candidate for solution by the finite volume method.

As an implementation of the finite volume method algorithm, the OpenFOAM computational fluid dynamics software package was selected.[8] Unfortunately, after a considerable amount of effort, the concept of adapting a CFD package to study spin dynamics was abandoned due to a rather steep learning curve and poor documentation for the software. The major impedances encountered were somewhat weak support for tensor objects such as $\vec{\mathbf{J}}$, as well as poor support for complex arithmetic. We believe that such problems are surmountable, therefore OpenFOAM should be given a second look in the future.

6.3 1-D simulations revisited

With the decision to abandon the 3-D finite volume solution, it was decided to revisit the 1-D simulations as performed by Nunes *et al.*.[1,2] The one dimensional problem as outlined in chapters 3 and 4 is a second order initial value problem with two boundary conditions specified, solved by the method of finite differences. The FORTRAN code used in the simulations of chapter 3 can be found in Appendix B of Dr. Nunes' Ph.D. dissertation.[1] As a benchmark, this code was scanned into a computer file and minimally altered to make it FORTRAN 90 compliant. An improved version was coded in C++ to ease scalability to higher dimensions. Code was written using the Eclipse integrated development environment running on the OpenSUSE 11.4 Linux operating system. The GNU compiler collection was used for both FORTRAN and C++ compilation, typically with optimization option *-O0* while debugging and *-O3* while running a complete simulation. The performance difference between the unoptimized *-O0* and optimized *-O3* code was breathtaking.

6.3.1 Major differences and improvements

All of the simulation code implemented was adapted for use with the Paraview 3-D data visualization tool.[9] Paraview was capable of producing 3-D shaded vector plots of the polarization in the simulated cell, as well as animations of the polarization's time evolution. Both classes of programs, FORTRAN and C++, also output the spatial average of the axial component of the transverse polarization in the rotating frame within the NMR resonator versus time, i.e. the simulated output of spectrometer's real part. The imaginary part of the resonator output was also computed but was generally not of interest.

It was noted that the original FORTRAN implementation used a discretization of the Leggett and continuity equations, equations 6.1 and 6.2, which were first order accurate in space:

$$\frac{\partial m}{\partial x} \approx \frac{m_{k+1}^{n} - m_{k}^{n}}{\Delta x}, \tag{6.3}$$

where the superscript refers to the time variable and the subscript refers to the position variable. The C++ code was written to be second order accurate in space:

$$\frac{\partial m}{\partial x} \approx \frac{m_{k+1}^{n} - m_{k-1}^{n}}{2\Delta x}, \tag{6.4}$$

The original FORTRAN code assumed harmonic time dependence of the transverse polarization with a precession frequency given by the local Larmor frequency in the rotating frame, i.e.

$$\omega_L(\vec{r}) = \gamma \delta H(\vec{r}), \tag{6.5}$$

where γ is the gyromagnetic ratio of ^{3}He, 20.3789 kRadian/sec/Gauss, and $\delta H(\vec{r})$ is the residual applied static magnetic field

$$\delta H(\vec{r}) = H(\vec{r}) - H_0. \tag{6.6}$$

The C++ code did not make the assumption of harmonic time dependence, although there is no reason to believe the assumption is not valid.

Another important difference lay in the formulation of the initial values of the polarization. The FORTRAN implementation allowed the user to specify a fraction of the total polarization which would be projected into the transverse plane, with a random phase at each location in space. The motivation was to provide the transverse perturbations required to excite the Castaing instability without creating a net spatial average of the transverse polarization. While in practice this initial condition seemed to reproduce certain aspects of the behavior observed in the laboratory, it is hard to justify a purely random transverse polarization field. To make the simulation more realistic, the C++ implementation computed a spatially varying NMR rotation operator based on the local larmor frequency ω_L as given by equation 6.5. At each position in space, the code computed the matrix elements of the off-resonance rotation operator[10]

$$\hat{R}_{off} = \hat{R}_z(\phi)\hat{R}_y(\theta)\hat{R}_z(\omega_{eff}\tau)\hat{R}_y(-\theta)\hat{R}_z(-\phi) \tag{6.7}$$

where $\hat{R}_y$ and $\hat{R}_z$ are the rotation operators about the y and z axes in the Larmor frame, respectively, ϕ is the electrical phase of the rotation pulse, θ is the tilt away from the z axis, ideally $\frac{\pi}{2}$, given by

$$\theta = \arctan\left(\frac{\omega_{nut}}{\Omega_0}\right), \tag{6.8}$$

where ω_{eff} is the magnitude of the effective rotation frequency

$$\omega_{eff} = (\omega_{nut}^2 + \Omega_0^2)^{\frac{1}{2}}, \tag{6.9}$$

ω_{nut} is the nutation frequency

$$\omega_{nut} = \frac{1}{2} \left| \gamma h_1 \right|, \tag{6.10}$$

τ is the duration of the RF pulse, h_1 is the magnitude of the RF magnetic field, and $\Omega_0 = \gamma \left(H(\vec{r}) - H_0 \right)$ is the shift in the local precession frequency away from the average Larmor frequency. The matrix representation of the y and z rotation operators for a spin $\frac{1}{2}$ particle are

$$\hat{R}_y(\theta) = \begin{pmatrix} \cos\frac{1}{2}\theta & -\sin\frac{1}{2}\theta \\ \sin\frac{1}{2}\theta & \cos\frac{1}{2}\theta \end{pmatrix} \tag{6.11}$$

and

$$\hat{R}_z(\theta) = \begin{pmatrix} \mathrm{e}^{-\frac{1}{2}i\theta} & 0 \\ 0 & \mathrm{e}^{+\frac{1}{2}i\theta} \end{pmatrix}. \tag{6.12}$$

Next we formulate the appropriate equilibrium density matrix $\hat{\rho}$ for a given polarization M

$$\hat{\rho} = \begin{pmatrix} \frac{1+M}{2} & 0 \\ 0 & \frac{1-M}{2} \end{pmatrix}, \tag{6.13}$$

and apply the rotation operator $\hat{R}_{off}$ to obtain the local polarization after the pulse:

$$\hat{\rho}' = \hat{R}_{off} \hat{\rho} \hat{R}_{off}^{-1}. \tag{6.14}$$

We then solve for the polarization vector after the RF pulse, $\mathbf{M} = (M_x, M_y, M_z)$, which is the projection of the density matrix $\hat{\rho}'$ onto the Pauli matrices $(\sigma_{\mathbf{x}}, \sigma_{\mathbf{y}}, \sigma_{\mathbf{z}})$.

The initial conditions clearly depend on knowledge of the spatial distribution of the magnetic field $H(\vec{r})$. Spatial inhomogeneity of $H(\vec{r})$ has two components, the applied magnetic field gradient and the intrinsic inhomogeneity of the NMR magnetic field. While it is likely impossible to precisely compute the latter field, the C++ code made some approximations based on a simple zonal harmonic expansion due to Garrett[11] which was matched to the NMR magnet homogeneity as quoted by the manufacturer, American Magnetics. This allowed us to compute the local field gradients due to magnet inhomogeneity inside and, to within reason, outside the quoted high-homogeneity region.

Both the original FORTRAN and the C++ code solved the set of coupled partial differential equations, equations 6.1 and 6.2, using an explicit method with very small time steps ($\sim 1\mu$sec).[1] A typical spatial grid size was 256 points for the FORTRAN code and 1024 points for the C++ code. In either case, the Courant stability condition for discretization of ordinary diffusion problems is well satisfied.[12] As a testimony to improvements in computer technology, it is interesting to note that the original simulations took on the order of one day to complete, while the recent simulations took about three minutes even though the grid size is four times larger.

6.3.2 Modeling the spin dynamics in the connecting tube

By far the most important difference between our original FORTRAN code and the recent C++ implementation was the treatment of the spin dynamics in the tube connecting the upper chamber (or reservoir) to the lower chamber (or NMR cell). The original FORTRAN code assumed that the polarization in the tube varied linearly with position inside the tube and that the dynamics of the tube could be replaced with an easily computed spin current:

$$J_z(\vec{r}=0) = -\frac{D_0}{L_{chan}}(M_z(0) - M_0), \tag{6.15}$$

$$J_+(\vec{r}=0) = -\frac{D_0}{L_{chan}}M_+(0), \tag{6.16}$$

where D_0 is the bare spin diffusion constant, L_{chan} is the length of the channel, $M_z(0)$ and $M_+(0)$ are the longitudinal and co-rotating polarizations at the interface between the NMR cell and the tube, respectively, and M_0 is the constant polarization in the upper chamber toward which the system is relaxing. Treatment of the boundary condition in the C++ code assumed that the polarization at the interface between the connecting tube and the reservoir was fixed at $M_z = M_0$, $M_+ = 0$; the spatial distribution of the polarization in the connecting tube was treated as an unknown to be computed as part of the solution.

Figure 6.1 illustrates the unphysical nature of the original treatment of the spin dynamics inside the connecting tube. When the spin populations are inverted by an NMR π pulse, the polarization inside the resonator is inverted, while the polarization inside the connecting tube remains, to lowest order, unaffected. This is demonstrated by the upper snapshot in figure 6.1. If we model the spin dynamics according to equations 6.15 and 6.16 and the linear spatial variation assumption which led to them, at an infinitesimally small time later, the polarization looks like the lower snapshot in figure 6.1. Clearly, the system cannot respond so quickly and our model is incorrect. We must model the time evolution of the polarization in the connecting tube similarly to that inside the NMR resonator. As with many discoveries, this fact was uncovered more by accident than by reason: the simulations of chapter 4 showed a glimpse of bursting behavior while the simulations of chapter 3 did not. The most substantial difference between the two scenarios was the treatment of the time evolution of the polarization in the connecting tube. We then expanded our sample cell snapshots to include the polarization in the tube and it was clearly observed that the time evolution was much more complex than that predicted by equations 6.15 and 6.16.

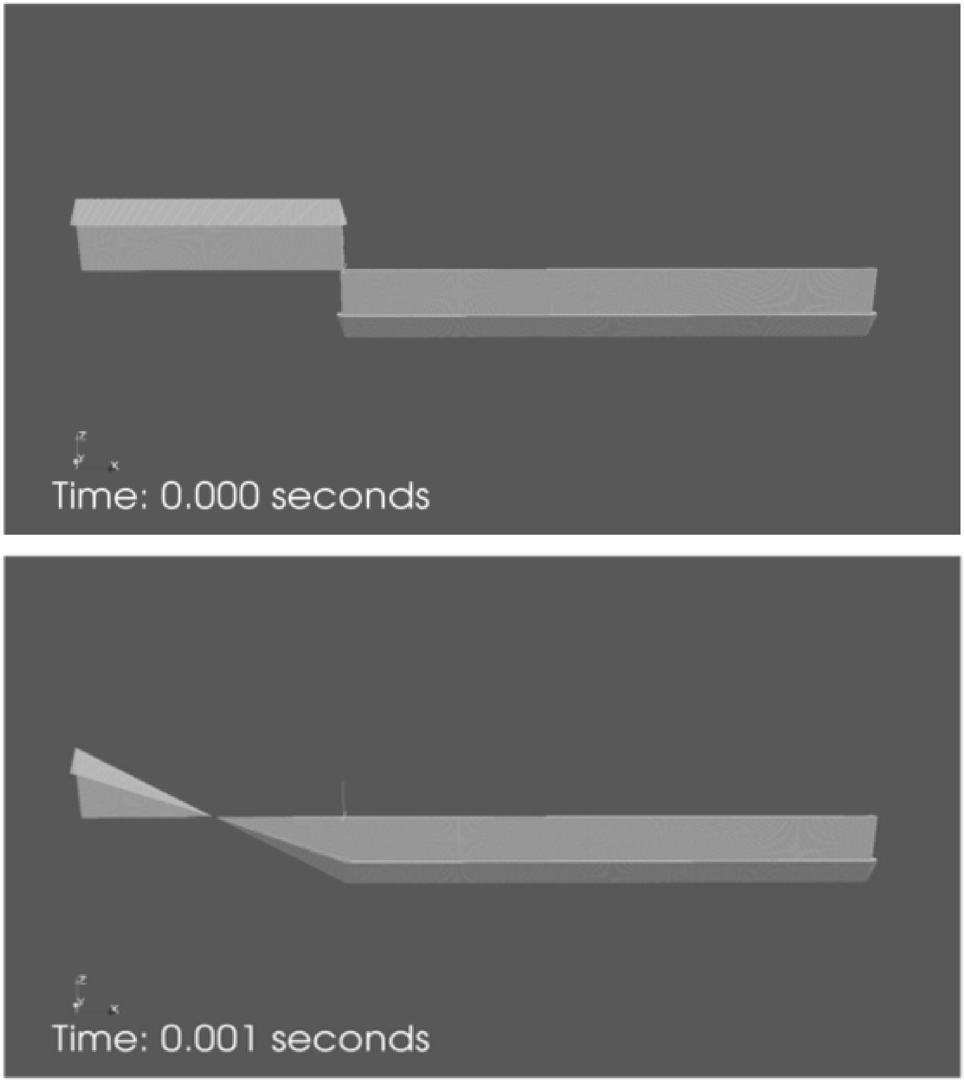

Figure 6.1: Distribution of polarization before and immediately after start of simulation using the original FORTRAN code. The polarization in the tube is on the left of each plot; the polarization in the NMR resonator is on the right. It is not physically possible for the system to respond so quickly, hence the FORTRAN code missed the bursting behavior.

6.3.3 Importance of the sign of the magnetic field gradient

The simulations presented in chapter 4 were somewhat puzzling. While they showed evidence of the bursting phenomena, the characteristic delay was missing completely. At that point in time, the C++ code was nearly algorithmically identical to the FORTRAN code, so indeed we were puzzled until, again by pure chance rather than reason, we changed the sign of the magnetic field gradient. A careful reading of reference 2 reveals that in fact a negative gradient was used in the laboratory and in the original simulations. Here a positive gradient implies that the static magnetic field is lower at the open end of the cell (where the NMR cell meets the connecting tube) and higher at the closed wall end. A negative gradient implies that the static magnetic field is higher at the open end and lower at the closed end. With the correction of the sign of the applied linear field gradient, the C++ implementation produced delayed output as expected, although the delay is approximately $\frac{1}{4}$ of the delay observed in the laboratory. We shall have more to say about this in section 6.3.4.1.

Although not strictly rigorous, it is instructive to examine the qualitative differences between the positive and negative applied gradients using the linearized Leggett equation,

$$\frac{\partial m_+}{\partial t} = D_S \frac{i - \mu M_z}{1 + \mu^2 M_0^2} \nabla^2 m_+ + \gamma \delta H m_+. \tag{6.17}$$

The solution to this equation with a linear applied gradient δH and reflecting boundaries is illustrated by Bigelow[13] in the context of nuclear spin waves in doubly spin polarized hydrogen. The spin wave eigenfunctions are described by the Airy function Ai; the eigen frequencies are determined by the roots of the derivative of Ai. Figure 6.2 depicts the lowest energy spin wavefunctions $m_+(\vec{r})$ in a positive field gradient. The wavefunctions are spatially confined to the lower field region at the end of the cell, i.e. the open end for positive gradients and the closed

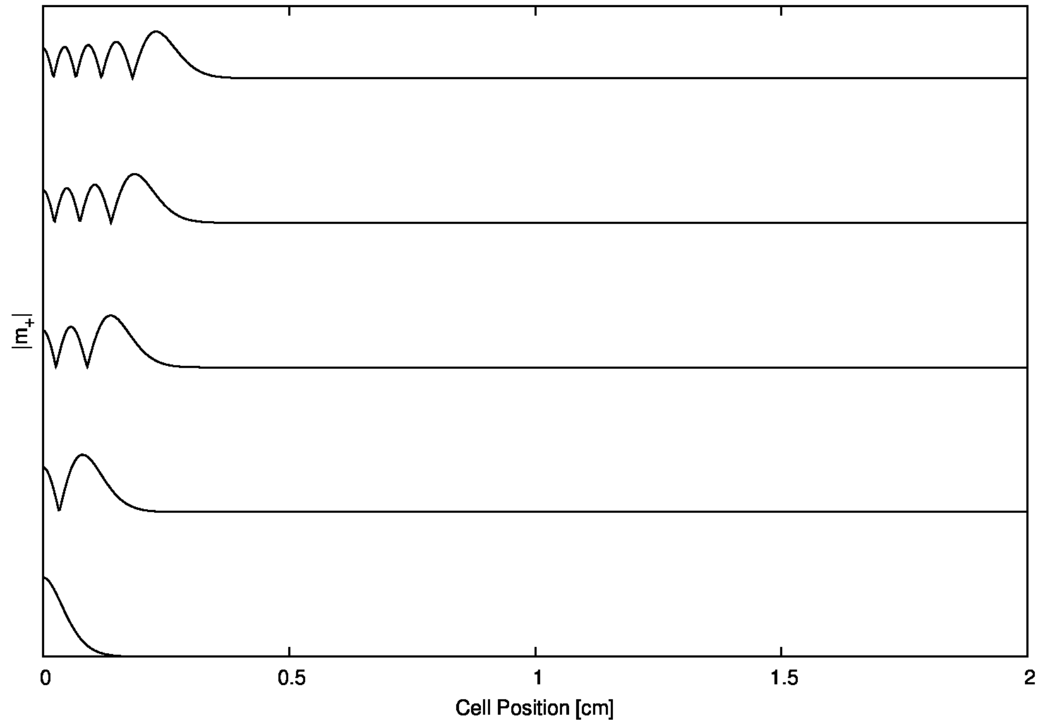

Figure 6.2: Magnitude of the five lowest energy Airy modes for a 350 ppm solution at 10.4 mK in a +0.02 G/cm linear magnetic field gradient. Plots have been offset for clarity and arranged in order of ascending energy, the lowest energy being at the bottom of the figure. The wave functions have not been normalized. As the x position approaches 2 cm, the length of the cell, all five wave functions decay to zero.

end for negative gradients. Noting this, we begin to understand qualitatively why the sign of the gradient is important.

Let us assume for a moment that the presence of the connecting tube at one end of the cell is a minor perturbation which does not greatly impact the eigenfunctions which are derived using reflecting boundary conditions. This is certainly not true in the 1-D simulations, but it provides a place to start. Since there exists, in general, a gradient in the polarization m_+ at the open end of the cell, there will in general be a spin current $\overrightarrow{\mathbf{J}}$ flowing at that point in space. If the field gradient is positive, then the low energy eigenfunctions are confined to the open end region and may couple easily to the spin current $\overrightarrow{\mathbf{J}}$. However, if we reverse the gradient, giving it a negative value, the lower energy eigenfunctions are confined to the closed wall end of the cell and the spin current cannot couple to these modes. While it is not easy to say quantitatively what the difference in the excitation spectra will be, it is clear that the two conditions may yield different behavior. Indeed, the simulated spectrum shown in figure 4.4, produced with a positive gradient and hence able to more easily excite the low energy Airy modes, clearly shows modes which appear similar to those seen in spin polarized hydrogen. However, spectra produced from simulations with a negative gradient show a broad line with no clearly resolved modes. Similar spectra were observed in the laboratory as well. This brings to mind a bitter pill to swallow: had we reversed the gradient in the laboratory, we might have seen the characteristic Airy spectra and been able to extract μM and $D_{\perp}$, two highly sought after pieces of information.

6.3.4 Effect of RF field inhomogeneity

It was always assumed that the RF field h_1 inside the NMR resonator was extremely homogeneous due to the electromagnetic skin effect at low temperatures and high frequency. The high conductivity of the OFHC copper resonator at $T \approx 60$ milli-Kelvin and the high frequency of the RF field, $f \approx 300$ MHz, combined to create a cylindrical cavity which no flux lines could cut. This is certainly true. However the flux lines still splayed away from the cylindrical axis of the resonator at either end, causing h_1 inhomogeneity. While this inhomogeneity is amenable to calculation, we chose to treat the problem phenomenologically and add various amounts of RF field inhomogeneity and observe the effect on the simulated spin system.

6.3.4.1 Perfectly homogeneous RF field: no bursting

The initial conditions for the case of perfectly homogeneous RF field h_1 are shown in figure 6.3. Given these initial conditions, the simulated resonator output for a 350 ppm solution at 10.4 mK in a -0.02 Gauss/cm linear static field gradient is shown in figure 6.4. Noticeably absent from the simulated resonator output are the initial bursts. The signal has a slight characteristic delay, but it is only approximately 0.25 seconds, at least a factor of four smaller than that observed in the laboratory.[1,2] This discrepancy is not inexplicable. It is clear from the associated animation that the system relaxes through a mechanism much more complex than the ordinary diffusion, which predicts approximately the correct delay time. The animation snapshot shown in figure 6.5 displays a complex twisting pattern of the polarization vector at the connecting tube/resonator interface. This mode of relaxation appears to be faster than ordinary diffusion, shortening the time it takes for spin turbulence to develop and the domain wall to form, and hence yielding a shorter delay time. Figure 6.6 shows a snapshot of the system just before the formation of the domain wall when the motion of the polarization is turbulent. This provides more evidence that we have correctly identified the steady state spin dynamics as a domain wall nucleated via the Castaing instability.[1,2]

6.3.4.2 Small RF inhomogeneity: observation of a single burst

Figure 6.7 shows the initial conditions with a small amount of h_1 inhomogeneity added. Specifically, the tipping angle at the open end of the cell was varied exponentially from 170° at the interface to the connecting tube to 180° at the center of the cell with a decay constant of $dx = 0.02$ cm. A similar taper was given to the tipping angle at the closed end of the NMR cell, which is still inside the resonator. A non-zero tipping angle inside the connecting tube was also included to simulate

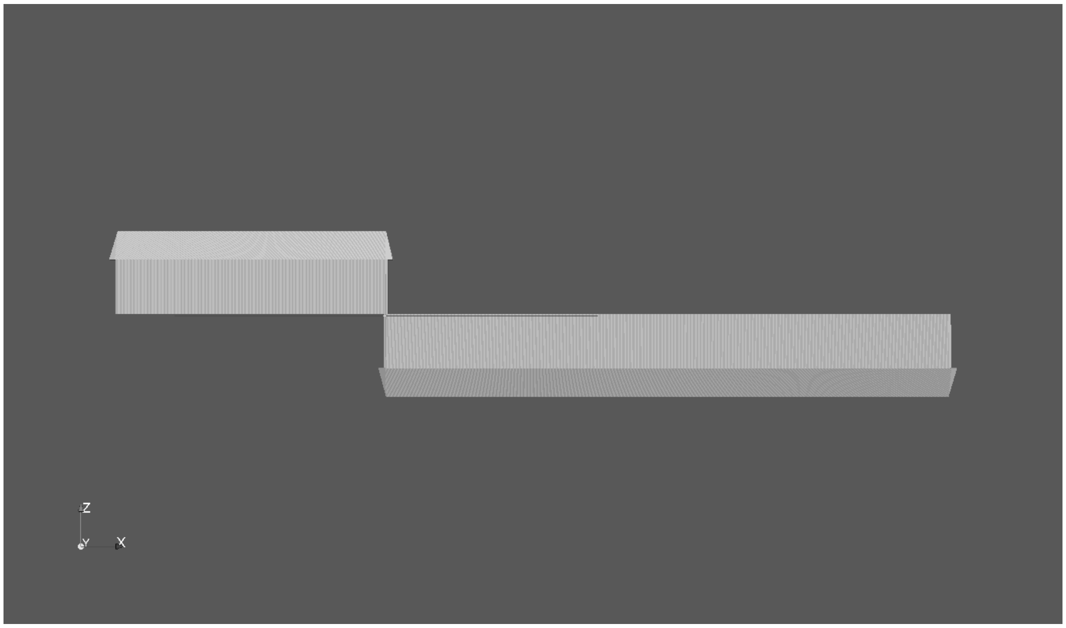

Figure 6.3: Initial conditions with a no RF field inhomogeneity. The tipping angle is 180° inside the resonator and zero in the connecting tube.

the effect of the NMR resonator's return flux on the spins in the tube. The tipping angle inside the tube was exponentially varied from 10° at the interface with the NMR cell to 0° far away from the interface with a decay constant of $dx = 0.02$ cm.

Figure 6.8 shows the simulated NMR resonator output for a 350 ppm solution at 10.4 mK with a -0.02 G/cm gradient perpendicular to H_0, with the initial conditions as described above. One burst at $t \approx 0.2$ seconds is clearly visible. Also visible in a snapshot of the cell/tube animation, figure 6.9, is the formation of multiple traveling wave packets. These wave packets provide an effective mode of spin transport across the polarization gradient.

There are two possible scenarios for the generation of the wave packets. In the first scenario, the wave packet nucleates as a transverse perturbation to the downward-pointing polarization *inside* the resonator. Such a disturbance rapidly

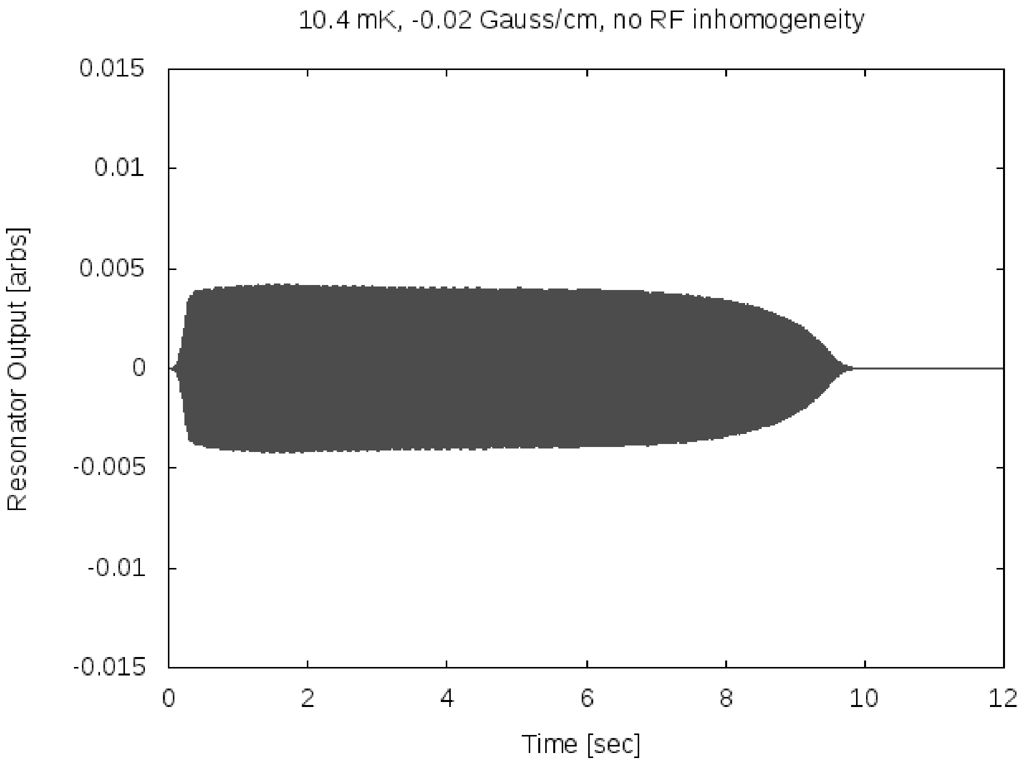

Figure 6.4: Simulated resonator output for 350 ppm solution at 10.4 mK in a -0.02 Gauss/cm gradient perpendicular to H_0 with initial conditions after the π pulse as shown in figure 6.3 (perfectly homogeneous RF field).

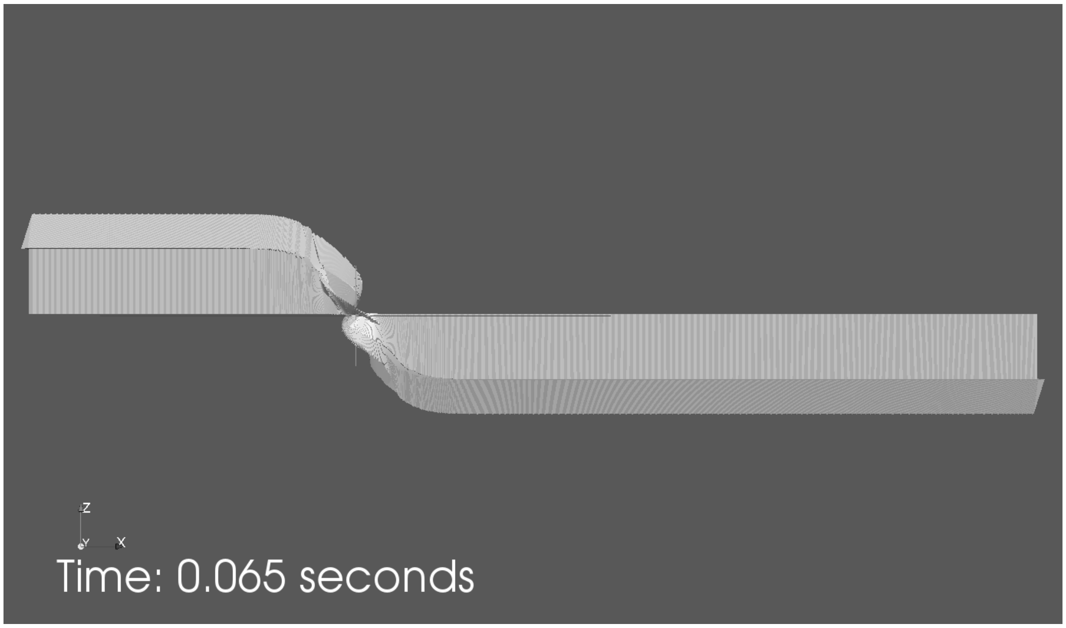

Figure 6.5: Sample cell and connecting tube snapshot corresponding to the perfectly homogeneous RF field initial conditions as shown in figure 6.3 at time $t = 65$ mSec. The tube is on the left; the NMR cell is on the right. The polarization twists in time and space like an auger bit, rapidly equilibrating the two regions of polarization.

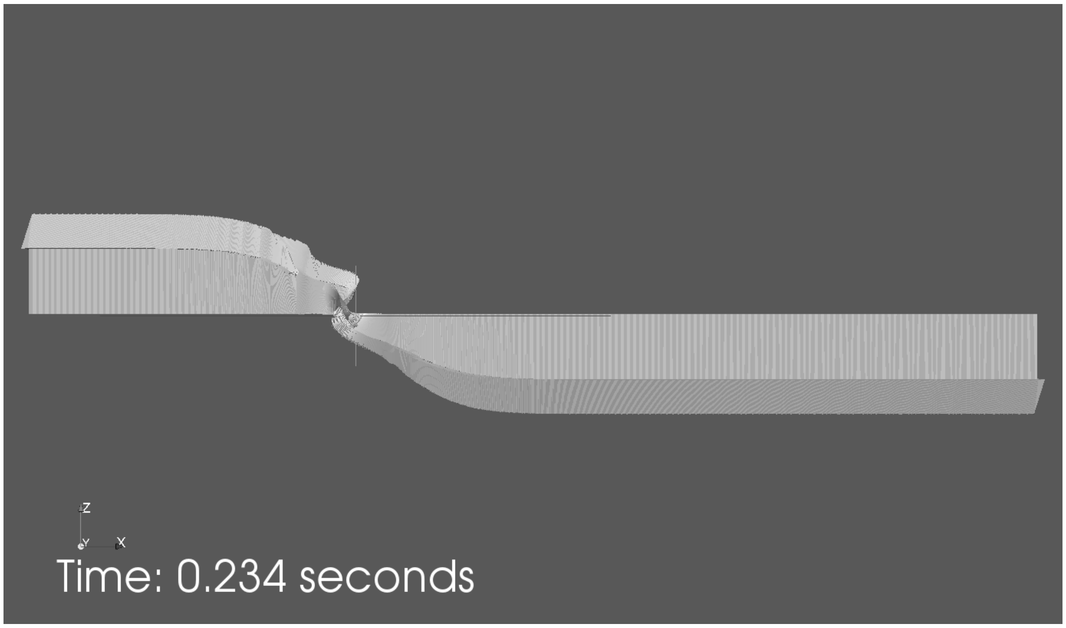

Figure 6.6: Sample cell and connecting tube snapshot corresponding to the initial conditions as shown in figure 6.3 (perfectly homogeneous RF field) at time $t = 234$ mSec. At this time, the polarization at the interface between the NMR cell and the connecting tube develops turbulent behavior.

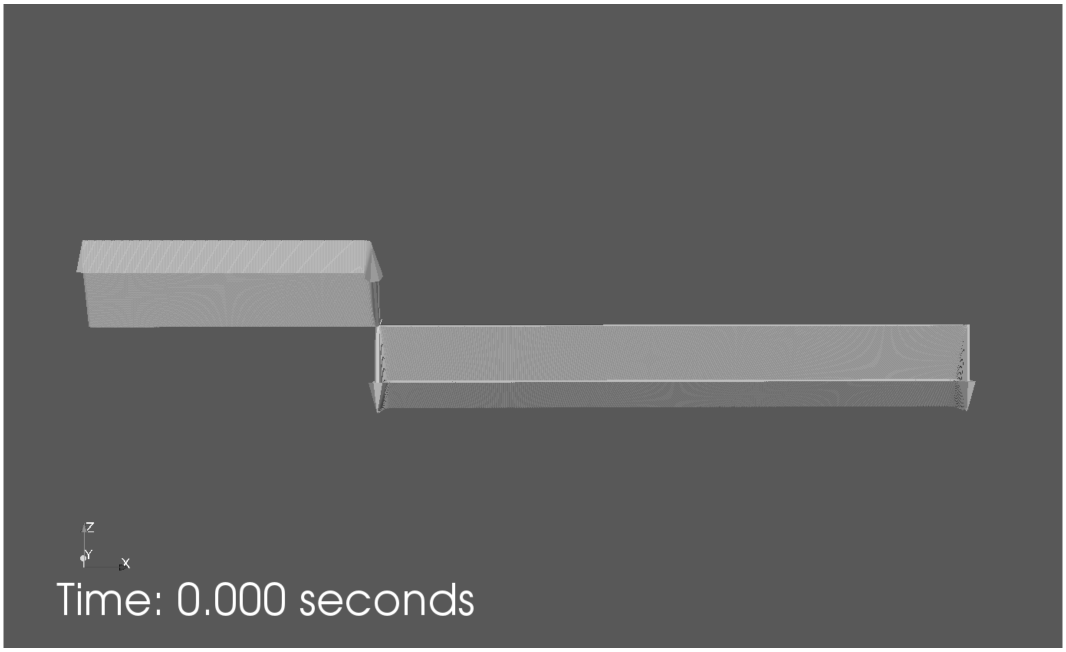

Figure 6.7: Initial conditions with a small amount of RF field inhomogeneity. The tipping angle is varied by 10° at each end of the NMR cell and at the end of the connecting tube.

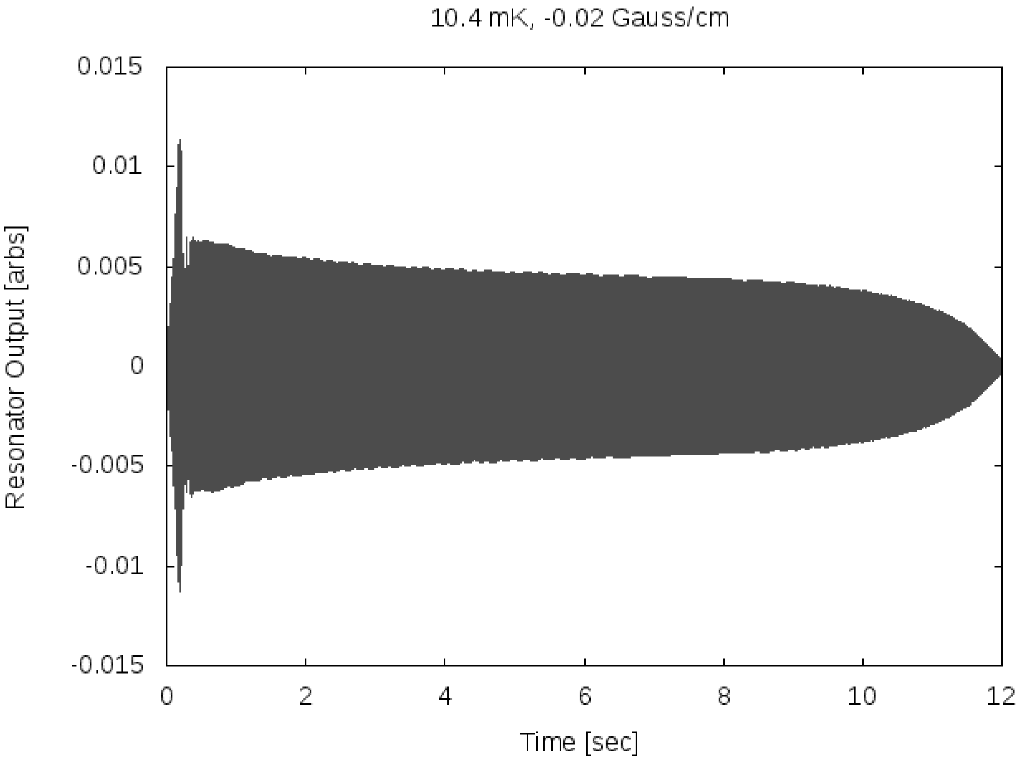

Figure 6.8: Simulated resonator output for 350 ppm solution at 10.4 mK in a -0.02 G/cm gradient perpendicular to H_0 with initial conditions after the π pulse as shown in figure 6.7 (modest RF field inhomogeneity).

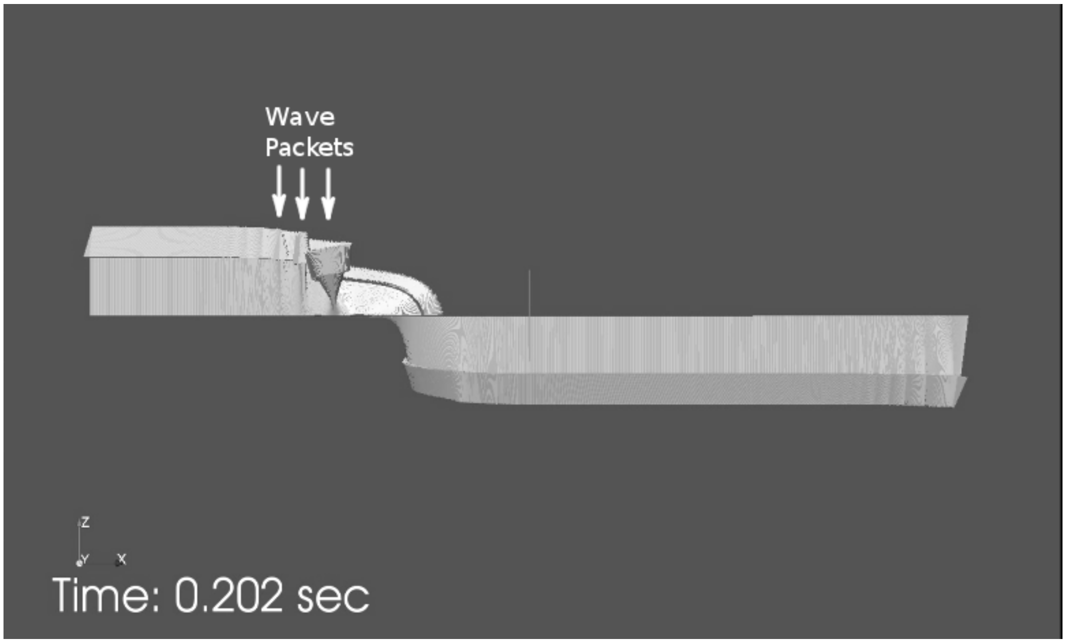

Figure 6.9: Sample cell and connecting tube snapshot corresponding to the time of the burst event seen in figure 6.8. The tube is on the left; the NMR cell is on the right. Three or more wave packets are visible in the tube at the left. In the animation, wave packets can clearly be seen nucleating inside the resonator at the right of the precessing domain wall, nutating into an upward orientation and traveling down the tube. Physical parameters are appropriate for a 350 ppm solution at 10.4 mK in a -0.02 G/cm gradient perpendicular to H_0.

nutates into a position where the longitudinal component points up, i.e. the packet flips over. As the packet nutates, it is ejected from the cell. This process can be clearly seen in the animation. Since the nutation process occurs while the wave packet is inside the resonator, we can observe a corresponding signal in the simulated resonator output. This is the source of the high amplitude oscillations which compose the single burst shown in figure 6.8. Figure 6.10 shows an expanded view of the burst seen in figure 6.8 with the oscillation period highlighted. This period, 15 mSec, is precisely the period between creation of the wave packets as determined from the animation. This corresponds to a modulation of the resonator RF output at 66.7 Hz. It also corresponds to one precession of the domain wall. In summary, one precession of the domain wall creates one wave packet which creates one period of output in the resonator!

At longer times, the wave packets are no longer generated inside the resonator on the "downstream" side of the domain wall, but rather are generated on the "upstream" side, essentially outside the resonator. We cannot observe such wave packet formation in the simulated resonator output: the resonator output falls and the burst ends.

Actually, these wave packets are not unfamiliar; we reported them in the work presented in chapter 4.[5] However, in that work we referred to the structures depicted in in figure 4.5 as domain walls. Labeling the structures as traveling wave packets would have been more accurate. They happen to be an effective mechanism by which the system may shed polarization which is out of equilibrium.

6.3.4.3 Large RF inhomogeneity: multiple bursts

Figure 6.11 shows the addition of RF inhomogeneity taken to an extreme. The tipping angle is made to smoothly vary from 0° at the leftmost end of the connecting tube to 180° inside the NMR cell. A Fermi function was used to provide the smooth

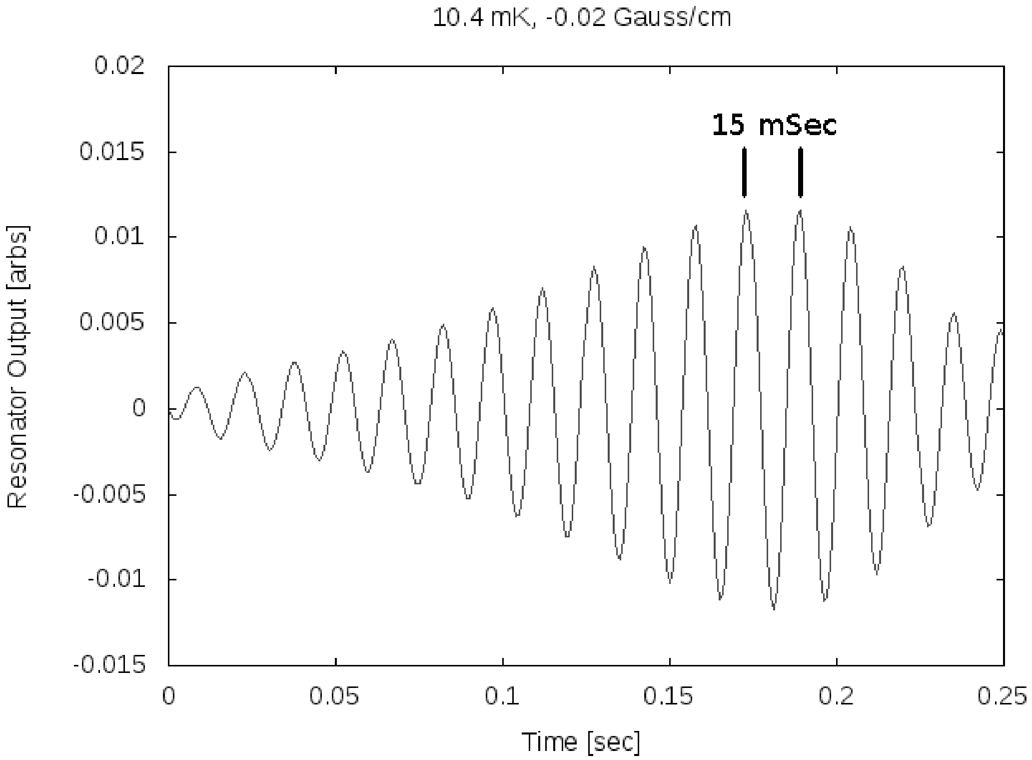

Figure 6.10: Expanded view of a burst in the simulated resonator output for 350 ppm solution at 10.4 mK in a -0.02 G/cm gradient perpendicular to H_0 with initial conditions after the π pulse as shown in figure 6.7 (modest RF field inhomogeneity). Oscillation period is approximately 15 mSec.

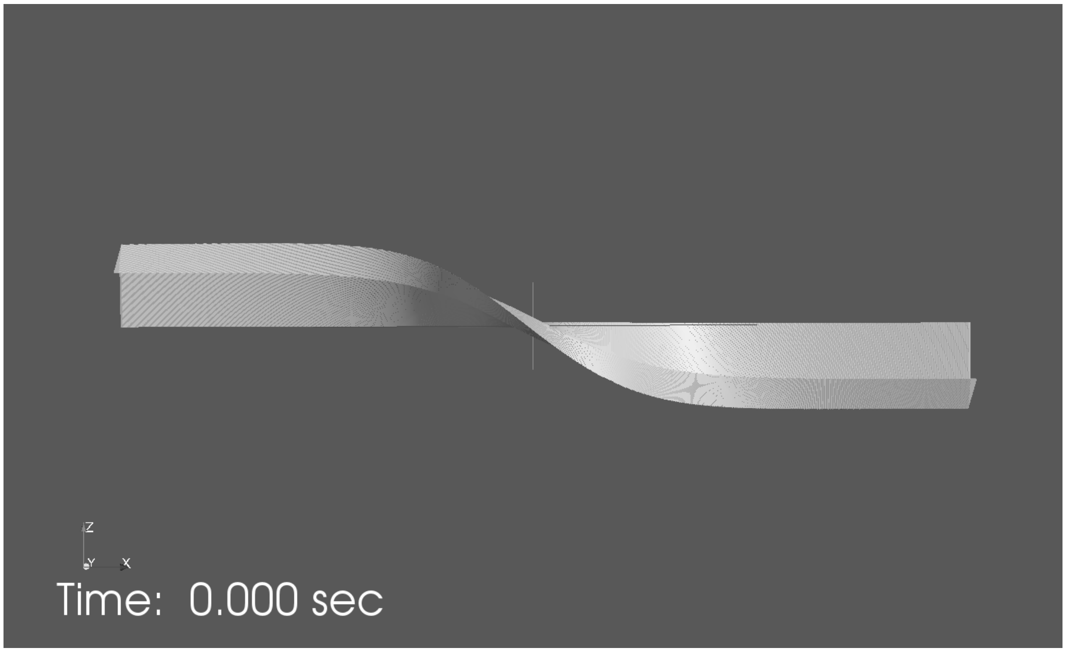

Figure 6.11: Initial conditions with a large amount of RF field inhomogeneity. The tube is also elongated to prevent standing waves from forming.

variation. The function passes through 90° at the interface between the tube and the cell. The length of the tube was increased to model the presence of the vast reservoir and prevent standing waves from forming.

The simulated resonator output corresponding to a 350 ppm solution at 10.4 mK with a -0.02 G/cm gradient perpendicular to H_0 is shown in figure 6.12. Multiple bursts are clearly visible. It is also clear that the height of the bursts is monotonically decreasing and the duration or width of the burst is monotonically increasing. This behavior is *suggestive* of a single wave packet train propagating in a dispersive medium, perhaps undergoing partial transmission/reflection events at some boundaries. The solution to the linearized Leggett equation tells us that the transverse polarization propagation is indeed dispersive.[13] The dispersion relations

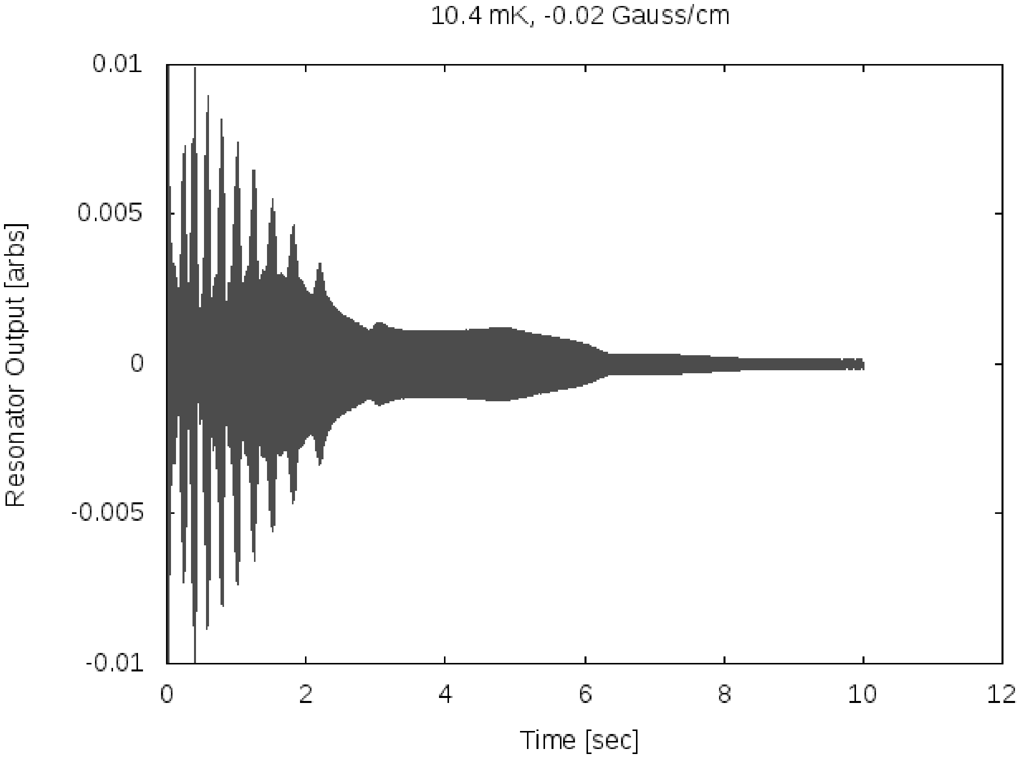

Figure 6.12: Simulated resonator output for 350 ppm solution at 10.4 mK in a -0.02 G/cm gradient perpendicular to H_0 with initial conditions after the π pulse as shown in figure 6.11 (large RF field inhomogeneity).

for longitudinal and transverse spin waves are[1]

$$\omega_z = ik^2 D_s \tag{6.18}$$

and

$$\omega_\pm = \frac{k^2 D_s (1 \mp \mu \mathrm{M}_0)}{1 + \mu^2 \mathrm{M}_0^2}. \tag{6.19}$$

The boundaries to be considered are the perfectly reflecting walls, the interface between the connecting tube and the reservoir, and the nonlinear excitation that is the domain wall. As reported in chapter 5, scattering of magnetic excitations by more massive non-linear modes is possible.

An attempt to follow the procedure used in the previous section to study a single burst, i.e. matching of features in the resonator output *with features in the animation*, proved to be unfruitful in the case of multiple bursts. The animation is too complex for a simple visual analysis to yield meaningful results.

6.4 Conclusions

We have performed numerical simulations of the spin dynamics in ^{3}He-^{4}He solutions and confirmed a slowly moving magnetic domain wall to be the quasi-steady-state solution as presented in chapters 3 and 4. Furthermore, we have evidence that the bursting phenomena observed in the laboratory is due to the relaxation of non-equilibrium polarization by rapid nutation. There is some suggestive evidence that these nutation events propagate as waves with group velocities much higher than that of the domain wall and may reflect off boundaries in the system; however there is no unequivocal proof of this hypothesis.

6.5 Future directions

It is clear that to completely understand the spin dynamics of the system, more theoretical work is needed, and perhaps more experimentation. There is a glaring need to explain the multiple burst phenomena. The resonator output looks so suggestive of a propagating disturbance, but what is propagating where? Furthermore, the need to prime the system with large amounts of h_1 inhomogeneity is unpalatable. Any future work must accurately describe h_1 based on the known resonator geometry. The simulations certainly need to be performed in higher dimensions where the connecting tube can be somewhat decoupled from the NMR cell. Another attempt at using a computational fluid dynamics package is warranted.

REFERENCES FOR CHAPTER 6

[1] G. Nunes, Jr., Ph.D. thesis, Cornell University (1991), (unpublished).

[2] G. Nunes, Jr., C. Jin, D. L. Hawthorne, A. M. Putnam, and D. M. Lee, Phys. Rev. B., **46**, 9082 (1992).

[3] B. Castaing, Physica B (Utrecht), **126**, 212 (1984).

[4] A. J. Leggett, J. Phys. C., **3**, 448 (1970).

[5] D. L. Hawthorne, V. V. Khmelenko, and D. M. Lee, in *Proceedings of the Twenty-Sixth International Conference on Low Temperature Physics* (To be published).

[6] J. D. Anderson, Jr., in *Computational Fluid Dynamics: An Introduction*, edited by J. F. Wendt (Springer-Verlag, Berlin, 2009) 3rd ed.

[7] E. Dick, in *Computational Fluid Dynamics: An Introduction*, edited by J. F. Wendt (Springer-Verlag, Berlin, 2009) 3rd ed.

[8] Http://www.openfoam.com/ (Accessed 12/20/2010).

[9] Http://www.paraview.org/ (Accessed 12/28/2010).

[10] M. H. Levitt, *Spin Dynamics: Basics of Nuclear Magnetic Resonance* (John Wiley and Sons, New York, 2001).

[11] M. W. Garrett, J. Appl. Phys., **38**, 2563 (1967).

[12] W. H. Press, B. P. Flannery, S. A. Teukolsky, and W. T. Vetterling, *Numerical Recipes in C*, 2nd ed. (Cambridge University Press, New York, 1994).

[13] N. P. Bigelow, Ph.D. thesis, Cornell University (1990), (unpublished).

APPENDIX A

SIMULATION PARAMETERS

A.1 Parameters used in ^{3}He-^{4}He solution simulations

The following is a reproduction of the configuration file passed to the C++ code when simulating a 350 ppm solution at 10.4 mK in a -0.02 Gauss/cm linear magnetic field gradient. Some of the parameters such as the random number seed are historical and are not used.

```
!!!!!!!!!!!!!!!!!!!!!!!!!!!!!!!!!!!!!!!!!!!!!!
!
! parameters.txt
! ~~~~~~~~~~~~~~
!
!!!!!!!!!!!!!!!!!!!!!!!!!!!!!!!!!!!!!!!!!!!!!!
!
! Log level (0=OFF, 1=ERROR, 2=INFO, 3=DEBUG)
3
!
! Temperature in mK
10.4
!
! 3He Concentration in ppm
350.0
!
! Number of cell points along x axis
64
!
! Number of cell points along y axis
4096
!
! Number of cell points along z axis
64
!
! Solution method (0=Explicit, 1=Implicit)
0
!
! Time step in seconds
1.0e-6
!
```

```
! Duration of computation
12.0
!
! Number of time steps between plots
1000
!
! Seed for random number generator
647
!
! Cell length in centimeters
2.096
!
! Cell radius in centimeters
0.437
!
! Length of the diffusion channel in centimeters
! 0.396
1.0
!
! Radius of diffusion channel in centimeters
0.122
!
! Spin diffusion constant D0 [cm^2/sec]
0.0375
!
! Spin rotation parameter mu
19.6
!
! Equilibrium magnetization to relax toward
0.45
!
! Constant magnetic field along z axis, Hz0, in gauss
9.2e4
!
! The magnet inhomogeneity in ppm
! Set to 0.0 to ignore inhomogeneity
0.0
!
! The volume over which the homogeneity is quoted, in cm**3
1.0
!
! Magnetic field gradient dHzdy, in gauss/centimeter
-0.020
!
! Magnetic field gradient dHzdz, in gauss/centimeter
!
0.0
```

```
! Offset of cell center from NMR magnet center along x, in cm
0.0
! Offset of cell center from NMR magnet center along y, in cm
0.0
! Offset of cell center from NMR magnet center along z, in cm
! TODO: fill in the real value here
0.0
!
! Model spin dynamics during NMR pulse?
!     0 => false; tipping is spatially uniform and instantaneous
!     1 => true; tipping is non-uniform based on local Larmor
!          frequency, plus the RF field strength and frequency
1
!!!!!!!!!!!!!!!!!!!!!!!!!!!!!!!!!!!!!!!!!!!!!!!!!!!!!!!!!!!!
!
! NMR pulse sequence
!
!!!!!!!!!!!!!!!!!!!!!!!!!!!!!!!!!!!!!!!!!!!!!!!!!!!!!!!!!!!!
!
! Number of pulses
1
!
! Note: when modeling the spin dynamics during a pulse,
! the duration is computed from the data below, otherwise
! the tipping is instantaneous.
!
! Pulse #1
! The initial 180 degree inverting pulse
! on 9.2 Tesla resonance
! (start time)(tip angle)(RF frequency)(RF Phase)(duration)
!  (seconds)   (degrees)    (Hertz)    (degrees)  (seconds)
      0.0        180.0     298.393e6      0.0      10.0e-6
```